Damage in Railway Crossings - Numerical Models

Dissertation

zur Erlangung des akademischen Grades

Doktor der montanistischen Wissenschaften

an der Montanuniversität Leoben

eingereicht von

Martin Pletz

Institut für Mechanik

Montanuniversität Leoben

Leoben, 20. Juli 2012

Acknowledgements

Danksagung

Für die Begutachtung dieser Arbeit und für die offizielle Betreuung möchte ich mich herzlich bei Univ.-Prof. Thomas Antretter vom Institut für Mechanik bedanken.
Auch danke ich Dr. Werner Daves, dem Leiter der Rad/Schiene/Weichen Projekte, für die Betreuung vor und während dieser Dissertation. Und die zahlreichen Diskussionen, aus denen diese Arbeit hervorgegangen ist.
Die vorgestellte Arbeit wurde in einem Forschungsprojekt mit der VAE GmbH in Zeltweg durchgeführt. Sollte der eine oder andere Teil dieser Arbeit gut geworden sein, so hat das ganz entscheidend mit der Unterstützung und den Diskussionen mit der VAE, allem voran DI Heinz Ossberger, zu tun. Dafür herzlichen Dank.
Außerdem danke ich Univ.-Prof. Robert Danzer vom Institut für Struktur- und Funktionskeramik (ISFK) dafür dass ich während meiner Dissertation am ISFK sitzen durfte und er mir einiges übers Präsentieren und Schreiben beigebracht hat. Herzlich danke ich meinen Kollegen am ISFK, besonders Dr. Raul Bermejo und Dr. Marco Deluca.
Zum Schluss möchte ich mich bei meinen Eltern Bernhard und Christa und meinen Brüdern Jakob, Lukas und Tobias bedanken. Für ihre Unterstützung bei dieser Dissertation und auch sonst.

Der österreichischen Bundesregierung (insbesondere dem Bundesministerium für Verkehr, Innovation und Technologie und dem Bundesministerium für Wirtschaft, Familie und Jugend) sowie dem Land Steiermark, vertreten durch die Österreichische Forschungsförderungsgesellschaft mbH und die Steirische Wirtschaftsförderungsgesellschaft mbH, wird für die finanzielle Unterstützung der Forschungsarbeiten im Rahmen des von der Materials Center Leoben Forschung GmbH abgewickelten K2 Zentrums für „Materials, Processing und Product Engineering“ im Rahmen des Österreichischen COMET Kompetenzzentren Programms herzlich gedankt.

Abstract

Damage in rails and turnouts is an important issue as it is one of the main causes for maintenance such as reprofiling (grinding) and replacing of rails. In the contact areas between rail and wheel, very high loads are produced that cause this damage in the form of wear and development of surface cracks. In the crossing panel of turnouts, the wheel has to change from one rail to another, causing a vertical impact. As the wheel has to roll on different rolling radii during this change, slip is produced. The impact thus leads to high contact pressures and high slip. Important parameters of the impact are the train speed, the wheel profile, the axle load and the crossing's support. In this thesis, dynamic and quasi-static finite element models for the passing over the crossing have been developed. Three models are used for describing the damage arising in crossings: A global dynamic model that calculates the run of a wheel through a three- metre crossing, a dynamic model that calculates the repeated impact of the wheel on the crossing nose and a quasi-static two-dimensional crack model. Loads have been transferred between those models, which shows that there are three important mechanisms for damage in crossings: a) The dynamics of the impact, determined mainly by crossing and wheel geometry, train speed and crossing support, b) the plastic adaption of the crossing to the wheel profile and c) the build-up of residual stresses near the crossing's surface. The plastic adaption and the residual stresses both reduce the loading of a crack and strongly depend on the plastic behaviour of the crossing material. Understanding these mechanisms that cause the loading of crossings allow for the optimization of crossings in terms of their material, support and geometry.

Zusammenfassung

Schädigung in Schienen und Weichen ist einer der Hauptverursacher für Wartungsarbeiten wie Schienenschleifen und Austausch von Schienen im Gleis. In den Kontaktflächen zwischen Rad und Schiene wirken hohe Lasten, die zu einer Schädigung in Form von Verschleiß und Rissbildung führen. Im Bereich der Herzstücke von Weichen wechselt das Rad seinen Lauf von einer Schiene auf eine andere. Dabei muss es sich aus geometrischen Gründen und abhängig von der Bauart der Weiche nach unten und oben bewegen, was in einem vertikalen Stoß resultiert. Da das Rad eine konische Lauffläche besitzt und sich die Kontaktpositionen am Rad während diesem Überlauf ändern, kommt es dabei auch zu Schlupf. Dieser Stoß führt somit zu hohen Kontaktdrücken und hohem Schlupf, die durch Parameter wie die Zuggeschwindigkeit, das Radprofil, die Achslast und die Lagerung der Weiche bestimmt werden. In dieser Arbeit wurden dynamische und quasistatische finite Elemente Modelle für den Herzstücküberlauf entwickelt. Drei Modelle berechnen die Schädigung in Herzstücken: Ein globales dynamisches Modell mit einem Radlauf über drei Meter des Herzstücks, ein dynamisches Modell für den wiederholten Stoß des Rads auf der Herzspitze und ein quaststatisches zweidimensionales Modell mit einem Oberflächenriss. Die Belastungen werden zwischen den einzelnen Modellen übertragen. Es zeigt sich, dass es drei wichtige Mechanismen gibt, die für Schädigung in Herzstücken verantwortlich sind: a) Der dynamische Stoß des Rads beim Aufsetzen, bei dem die Geometrie von Rad und Herzstück, Zuggeschwindigkeit und Lagerung des Herzstücks eine wichtige Rolle spielen, b) die geometrische Anpassung der Herzspitze (durch plastische Verformung) an das Radprofil und c) der Aufbau von Eigenspannungen nahe der Herzstückoberfläche. Die plastische Anpassung des Herzstücks und die Eigenspannungen reduzieren im Allgemeinen die Belastung eines Risses im Kontaktbereich, wobei das plastische Materialverhalten des Herzstücks dabei eine entscheidende Rolle spielt. Das Verständnis dieser Belastungsmechanismen erlaubt Vorhersagen über den Einfluss des Materials, der Lagerung und der Geometrie von Herzstücken. Damit können in weiterer Folge Herzstücke optimiert werden.

Compilation of thesis

This thesis consists of an extended summary and the following appended papers

Paper A Pletz, M., Daves, W., and Ossberger, H., A Wheel Set / Crossing Model Regarding Impact, Sliding and Deformation- Explicit Finite Element Approach. Under Revision- Wear.

Paper B Pletz, M., Daves, W., and Ossberger, H., A Wheel Passing a Crossing Nose- Dynamic Analysis under High Axle Loads using Finite Element Modelling. Accepted for publication in Proceedings of the Institution of Mechanical Engineers, Part F: Journal of Rail and Rapid Transit, 2012.

Paper C Pletz, M., Daves, W., Eck, S., and Ossberger, H., The Plastic Adaption of Railway Crossings due to Dynamic Contact Loading - Explicit Finite Element Study. To be submitted.

Paper D Pletz, M., Daves, W., Yau, W., and Ossberger, H., Prediction of Rolling Contact Fatigue in Crossings- Multiscale FE Model, in Proceeding at the 8th International Conference on Contact Mechanics and Wear of Rail/Wheel Systems, Chengdu, China, 2012.

Related papers by the author

Paper E Pletz, M., Daves, W., Fischer, F.D. and Ossberger, H., A Dynamical Wheel Set: Crossing Model Regarding Impact, Sliding and Deformation, in Proceeding at the 8th International Conference on Contact Mechanics and Wear of Rail/Wheel Systems, Florence, Italy, pp 801-809, 2009.

Paper F Pletz, M., Daves, W., and Ossberger, H., Dynamic Finite Element Model of a Wheel Passing a Crossing Nose. Proceedings of the tenth international conference on computational structures technology, Valencia, Spain, 2010.

Paper G Pletz, M., Daves, W., and Ossberger, H., A Wheel Passing a Frog Nose- Dynamic Finite Element Investigation of High Axle Loads, Proceedings of the International Heavy Haul Association Conference, Calgary, Canada, 2011, on-line.

Paper H Pletz, M., Daves, W., Yau, W., and Ossberger, H., Multi-Scale finite element model to describe wear and rolling contact fatigue in the wheel – rail test rig, in Proceeding at the 8th International Conference on Contact Mechanics and Wear of Rail/Wheel Systems, Chengdu, China, 2012.

Paper I Pletz, M., Daves, W., and Ossberger, H., Understanding the Loading of Railway Crossings, Railway Gazette, August Issue, 2012.

Contribution to papers

Paper A (Extended version of paper E and F), paper B (extended version of paper G) and paper C

Responsible for the development of the method.
Carried out the numerical simulations.
Wrote most parts of the paper.

Paper D

Responsible for the development of the crossing model, the impact model and the methodology for combining the models on different length scales.
Carried out the numerical simulations for the crossing and the impact model (the crack model simulations were carried out by Weiping Yao).
Wrote most parts of the paper.

Paper H

Responsible for the development of the three-dimensional test-rig model and the methodology for combining the models on different length scales.
Carried out the numerical simulations for 3D test-rig model (the crack model simulations were carried out by W. Yao and the roughness model calculations by W.K. Kubin).
Wrote most parts of the paper.

Paper I

Responsible for the development of the method.
Carried out the numerical simulations.
Wrote most parts of the paper.

The extended summary of this thesis is nearly identical to Paper I. The support of Railway Gazette is gratefully acknowledged.

Affidavit

I declare in lieu of oath, that I wrote this thesis and performed the associated research myself, using only literature cited in this volume.

Leoben, July 2012

Martin Pletz

Contents

Extended Summary

1 Introduction

Turnouts are an important part of the track structure as they allow trains to switch from one track to the other. They are also a weak spot in the track structure as they cause an impact of the wheel in the horizontal (at the switch panel) or in the vertical direction (at the crossing nose). Issues such as wear and rolling contact fatigue (RCF) are thus very important for turnouts. In Figure 1, a typical rigid crossing is shown. It consists of two wing rails and a crossing nose. Moving from the front to the back in Figure 1 (facing move), the wheel runs initially on one wing rail and then impacts onto the crossing nose. In the opposite direction, the wheel impacts onto the wing rail. In the track, more damage is observed on the crossing nose than on the wing rail and thus the facing move is the more critical case for the evolution of damage. The model in this work thus only simulates the facing move.

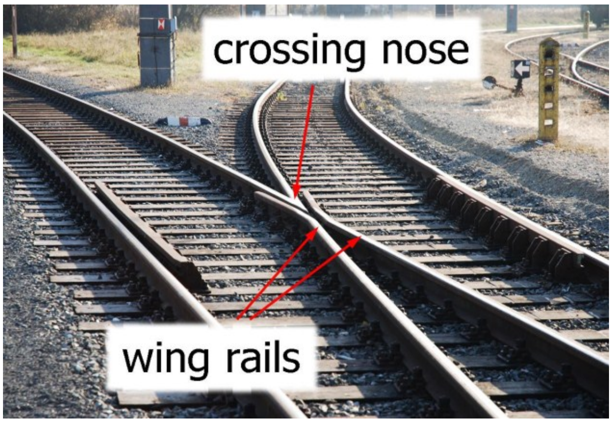

Figure 1: A picture of a rigid crossing. The wing rails and the crossing nose are highlighted.

One aim of the turnout producers is to minimize or, in the ideal case, totally avoid these increased loads to extend the lifetime and the maintenance intervals of turnouts. Crossings with movable crossing noses (in contrast to the rigid crossings) can nearly totally avoid the vertical impact of the wheel, but are due to their high costs only used in special applications such as high speed tracks or heavy haul lines. Understanding the factors that influence the loading of these crossings and as a consequence their damage provides a basis for the optimization of the crossing geometry, crossing material and properties of the elastic support. In this work, a finite element (FE) model is presented which simulates a wheel running over a crossing.

Parameters such as the train velocity, the wheel profile, the crossing's support and the axle load are varied to see the influences on the arising loads. With simplified analytical models, the origin of contact pressures and slip is explained.

Most commonly calculations for turnouts are done with multi body system (MBS) simulation tools, which model the whole train and track structure using point masses, springs and dashpots. The whole train and long parts of the track can be modelled. Simplified contact models provide the interaction of the wheels and crossing parts. Inelastic material behaviour cannot be used directly. Such calculations can e.g. be found in [1].

Focusing on the influences of load parameters on the material response, a simplified FE crossing model was developed by the authors. It is a fully dynamic model based on the method of finite elements, which calculates just one wheel running over the crossing. Therefore reasonable but simplified assumptions have to be made about the lateral wheel position and influence of the wheel set during the crossing process.

Within the group of involved engineers and scientists it has been shown that the understanding and prediction of the development of surface damage in rails such as wear, crack initiation and growth (commonly referred to as rolling contact fatigue-RCF) is a very complex topic. In Figure 2, a crossing nose with surface cracks and even breakouts is shown. There are various models that describe wear and crack formation [2, 3]. All models for surface damage somehow use the contact pressure (or force) and the slip velocity (relative velocity of contacting surface points). As there is no universal model available from which the kind and extent of surface damage can be predicted, the article deals with explaining the reasons that cause high or low contact pressure and slip on the crossing surface.

Figure 2: A damaged crossing nose with surface cracks and breakouts.

2 The FE Model

A dynamic finite element model has been developed to describe the process of the wheel transition from the wing rail to the crossing nose. The chosen geometry represents a rigid crossing with a curve radius of 760 m and without superelevation of the wing rail. These geometrical specifications need a FE model where the wheel has to roll over a distance of three metres. This distance has been shown as sufficient to model this transition, see **Paper A**. One wheel of the wheel set is modelled with finite elements; the second wheel was accounted for by its influence on the rolling velocity of the wheel set to obtain reliable results for the slip on the crossing nose. Using the FE geometry shown in Figure 3, simplifications of the boundary conditions are necessary. Most important, the steering of the bogie is neglected during this three-metre run of the wheel set. Furthermore, the lateral position of the wheel is fixed assuming a run along the check rail. The wheel has a constant longitudinal velocity but is free to change its rotational velocity. The elastic deformations of wheel and crossing are captured by the model. The mesh in the model is refined towards the contacting regions, which is shown in Figure 3b. Details about the model's setup are given in **Paper A, Paper B and Paper F**. In those papers, the influence of the train speed, crossing support and axle load on the dynamic response and the arising stresses are investigated with elastic-plastic material behaviour of the crossing. In the paper at hand, the model uses only elastic material behaviour for the representation of wheel and crossing.

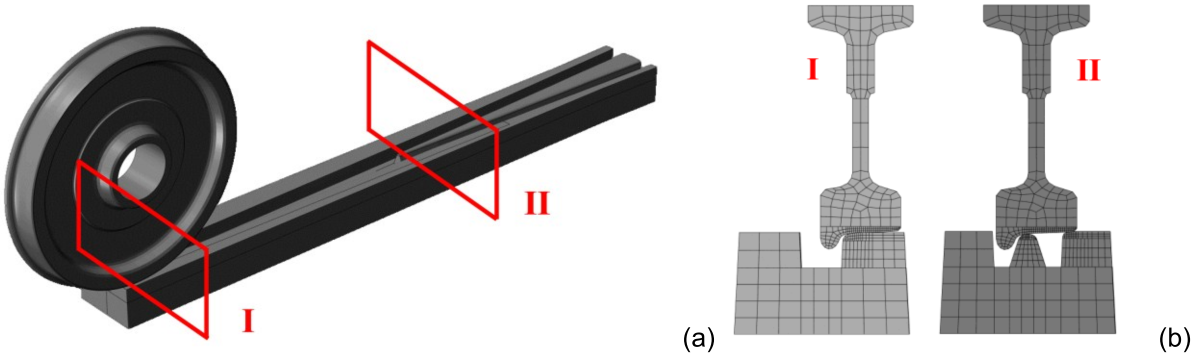

Figure 3: The three-dimensional crossing model with a) the whole geometry and b) cross-sections of the mesh at two positions.

In the current work, seven load cases are selected to illustrate the influences of the following parameters on the crossing's loading:

- Wheel profile
- Train speed
- Crossing support
- Axle load

All load cases are given in Table 1. Load case 1, the standard load case, represents a train speed of 160 km/h, an axle load of 14,200 kg, a crossing support in which the bottom of the crossing is connected with a parallel combination of a spring (c= 90 kN/mm) and a dashpot (k= 0.25 kNs/mm) to the ground, a new wheel profile and a wheel mass of 1025 kg.

Table 1: The seven load cases of the finite element model, with load case 1 being the standard case.

Load case	**Train speed**	**Wheel profile**	**Crossing support**	**Axle load**	**Wheel mass**
1- standard	160 km/h	new wheel	elastic support	14.2 tons	1025 kg
2	160 km/h	worn wheel	elastic support	14.2 tons	1025 kg
3	160 km/h	hollow wheel	elastic support	14.2 tons	1025 kg
4	75 km/h	new wheel	elastic support	14.2 tons	1025 kg
5	250 km/h	new wheel	elastic support	14.2 tons	1025 kg
6	160 km/h	new wheel	elastic support	32.4 tons	1500 kg
7	160 km/h	new wheel	rigid support	14.2 tons	1025 kg

The wheel profiles used in the model are shown in Figure 4. The grey – shaded shape represents the unworn wheel of the type UIC-ORE 1002. The hollow-worn wheel profile was taken from the literature [4] and its outline is drawn as a red curve (hollow wheel). A wheel that is worn at the flange and on the outside of the wheel tread (worn wheel) is drawn in blue. Note that the conicity of the wheel is defined as the average inclination of the wheel tread. For the three shown wheel profiles, the conicity is highest for the worn wheel and lowest for the hollow worn wheel. Load case 2 uses the worn wheel profile and load case 3 the hollow wheel, respectively. To investigate the influence of the train speed, two additional velocities of 75 km/h (load case 4) and 250 km/h (load case 5) are used. Load case 6 represents a heavy haul case using a higher axle load of 32,400 kg and a higher wheel mass of 1500 kg. Load case 7 uses a crossing with completely fixed bottom.

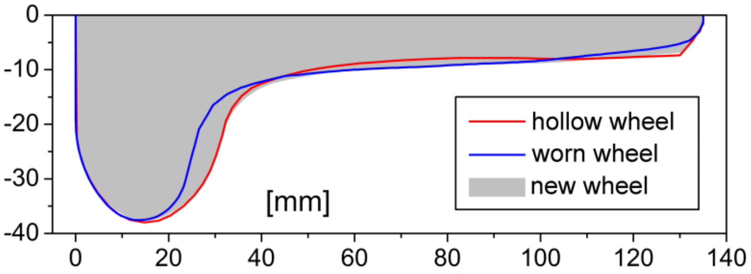

Figure 4: The three used wheel profiles. The new wheel is shown in grey, the hollow-worn wheel in red (case: *hollow wheel*) and the wheel with wear on the flange and on the outside of the tread is shown in blue (case: *worn wheel)*.

3 Mechanisms of Loading

During the rolling of a wheel over a crossing, the wheel changes its run from the wing rail to the crossing nose. To enable a smooth transition of the wheel, the crossings need to have a certain geometry where the wing rail deviates from the general track direction, henceforth denoted as “deviating wing rail”. Because of that geometry, the contact point of the wheel continuously changes its lateral position on the wheel tread. As some of the mechanisms of the crossing's loading can be explained by these changes and the corresponding running wheel radius, this is described in more detail. In Figure 5, the crossing is cut at three selected longitudinal positions and the contact geometries in these cross-sections is shown. It can be seen that initially (before reaching the deviating part of the wing rail) the wheel contacts the wing rail in the middle of its tread. As the wheel approaches the crossing, this contact position moves away from the flange. The first contact of the wheel with the crossing nose is close to the wheel’s flange. After the impact on the crossing, the lateral contact point on the wheel moves back to the middle of the wheel tread.

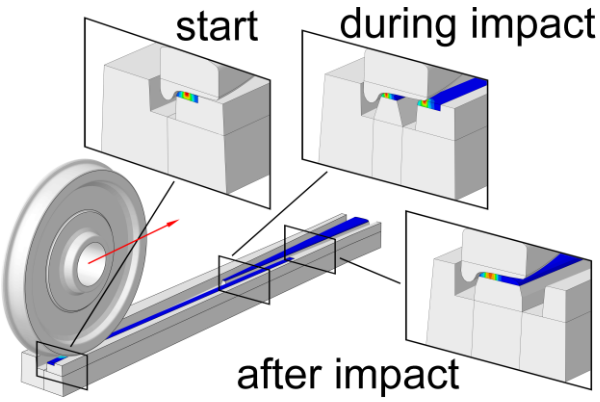

Figure 5: Three cross-sections of the wheel-crossing contact before, during and after the impact of the wheel onto the crossing nose. Note the different contact positions on the wheel tread.

This is also illustrated in Figure 6, where the initial and final contact point on the wheel are shown with a green point labelled “0”. On the wing rail, that contact point moves to the right to the position labelled “wr”. As the wheel impacts onto the crossing nose, the contact point on the wheel is close to the flange and in Figure 6 labelled “cn”. A certain lateral contact position on the wheel tread corresponds with a certain running radius of the wheel. In Figure 6, these radii are called R_0 (initial and final radius), R_{wr} (radius of the outermost contact point on the wing rail) and R_{cn} (radius of the first contact of the wheel with the crossing nose). This change of the rolling radius leads to two kinematic effects as the wheel runs over a crossing:

a) the wheel moves vertically (causing the impact)

b) the angular velocity of the wheel changes (causing the slip)

The vertical movement is associated with the vertical impact of the wheel onto the crossing nose and thus with higher contact pressures than on the regular rail. The angular velocity of the wheel set determines the sliding between the wheel and the crossing parts. It is commonly assumed that specific combinations of contact pressure and slip determine the type and degree of arising damage. In Figure 6, this scheme is illustrated. In the following, the two mechanisms (vertical impact and slip) are described separately (in contact mechanics it is valid and quite common to separate the normal and tangential contact problem).

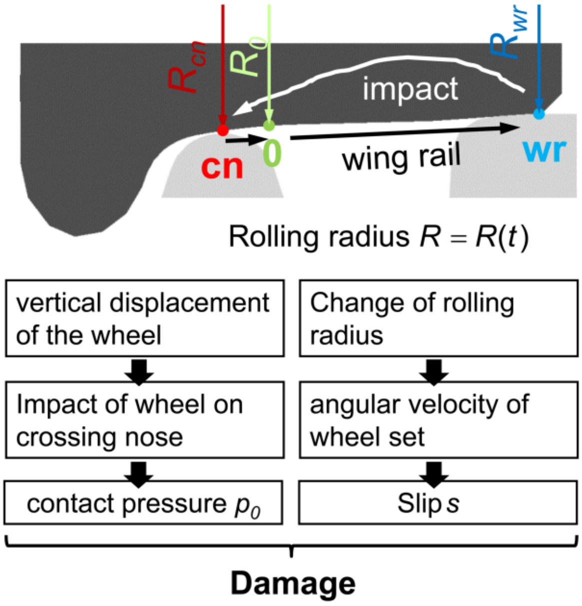

Figure 6: Schematic diagram of the loading of the crossing nose. At the top, the occurring contact positions on the wheel are shown and as they change on the wing rail, during the impact and on the crossing nose.

3.1 Vertical Movement of the Wheel – Impact

The impact of the wheel on the crossing nose is caused by the change of the moving direction of the wheel. Since the wheel is moving downward during its run on the wing rail (e.g. by a distance of 3 mm for a new wheel), it has to climb up again to the initial level on the crossing nose. In Figure 7a, this movement of the wheel centre is shown for the standard load case. The grey line gives the vertical displacement of the wheel centre, the green line the displacement of the crossing and the black line the relative displacement of wheel and crossing. Below the diagram, a picture of a crossing is shown that corresponds to the wheel positions.

In the beginning (wheel position of 0 – 0.2 metres) the wheel stays at about the same level. As the wing rail starts to deviate at a wheel position of 0.2 m, the wheel centre starts to move downwards. It continues its downward movement up to a position of 1.7 m, where it impacts onto the crossing nose. There, it starts to move upwards again until it reaches the same level it had in the beginning. At the impact, there is an angle α (impact angle) between the relative wheel movement before and after the impact. For the shown load case, this angle is 0.35°. The crossing is pressed downwards at the impact thereby reducing the impact forces. In Figure 7b, the wheel movements for the different wheel profiles are shown. It can be seen that the worn wheel drops by nearly 4 mm and has with a value of 0.66° a higher α than the calculation with the new wheel. The hollow worn wheel has nearly no conicity of the wheel tread and thus does not lower its vertical position on the wing rail during its run towards the crossing nose. At a wheel position of 1.6 m, however, it suddenly drops from the wing rail on the crossing nose accompanied by a higher impact angle α of 0.86°. This shows that there is a general tendency that decreasing wheel conicities lower the impact angle α but this is valid only to a certain extent. The impact angle is mainly determined by the contact geometry. The other parameters (axle load, train speed, crossing support) have nearly no influence on it.

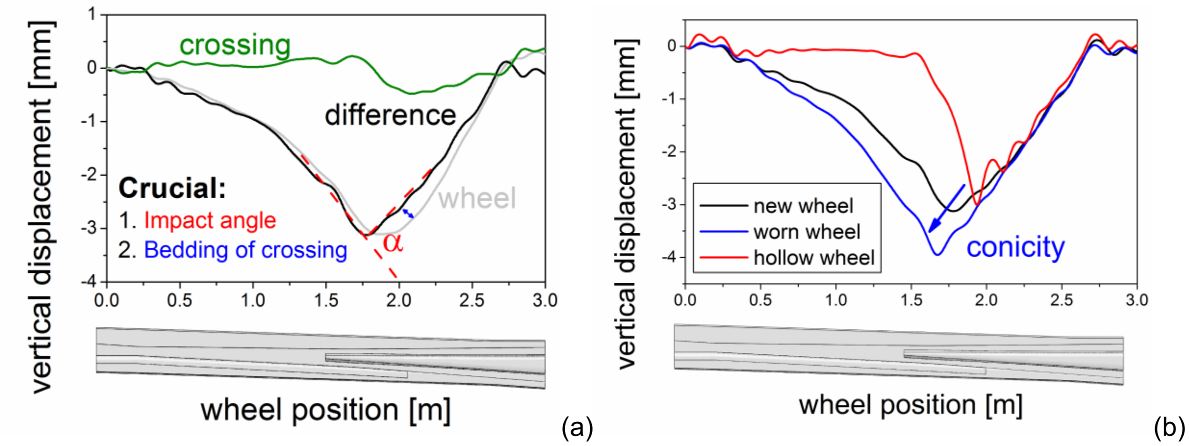

Figure 7: a) The vertical displacements of the wheel (grey line), a reference point on the crossing (green line) and the relative displacement (black line) as the wheel runs over the crossing in the standard load case. The impact angle α is shown in the diagram (red) and the effect of the crossing's support is indicated with a blue arrow. b) The relative displacement of the wheel for the three wheel profiles.

For a known impact angle α, the vertical impulse of the wheel can be written as the impacting mass of the wheel (m_{wheel}) times the impact velocity, which results from the train speed *v* times the impact angle α (for a small α):

$$P = m_{wheel}\,\alpha\,v \tag{1}$$

This impulse results in an impact with vertical loads higher than the train's weight per wheel (the static load f_0). Depending on this impulse and the crossings bedding, the static load f_0 is increased to reach the impact force f_{imp}:

$$f_0 \xrightarrow{P,\ \text{support}} f_{imp} \tag{2}$$

Details about the interrelation of the bedding and the impact force are given in [5]. Stiffer supports and higher impulses increase the impact force. Generally, these equations show that the impact forces rise with increasing train speeds, wheel masses, static loads, stiffer beddings and also for worn wheels whereas slightly hollow-worn wheel reduce the impact angle and thus impact forces. Severely hollow-worn wheels, on the other hand, drastically increase the impact angle and thus impact forces. In Figure 8, the development of the vertical contact force of the standard load case is shown along the wheel position. The wheel moves from the left to the right. At a wheel position of 0 m, it is placed on the wing rail, causing some oscillations of the contact forces. At a wheel position of 0.2 m, the wing rail starts to deviate and the wheel suddenly has to move downwards, which excites more oscillations of the vertical contact force. As the wheel approaches the crossing nose, the amplitudes of these oscillations decrease due to dashpots connected to wheel and the crossing. During the impact of the wheel on the crossing nose, the contact force is significantly higher than the static load. During the further run of the wheel on the crossing nose some more oscillations of the contact force occur, but due to the broadening of the crossing nose they produce less contact stresses and are less relevant as the first impact. The effect of the dynamic contact force f_{imp} on arising stresses during this first impact is strongly dependent on the position of impact x_{imp}. Both values are shown in Figure 8.

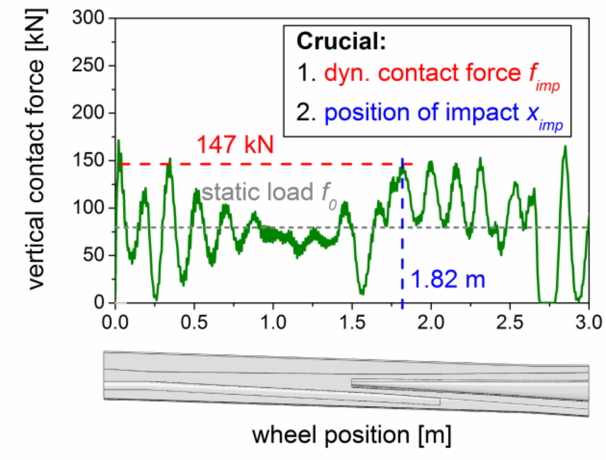

Figure 8: The vertical contact forces between the wheel and the crossing for the standard load case. The dynamic contact force during the impact f_{imp} (red) reaches a value of 147 kN at a wheel position of impact x_{imp} of 1.81 m.

In Figure 9, the vertical contact forces for all 7 load cases are shown for wheel positions from 1.5 to 3 metres, where the impact occurs. In the left diagram, the three wheel profiles are compared. The earlier impact of the worn wheel (load case 2) can be seen as well as the later impact of the hollow wheel (load case 3), causing extremely high contact forces of 500 kN. The middle diagram in Figure 9 shows the results for the three train speeds are shown. The impact position x_{imp} is the same for the three cases, but the contact forces of the impact increase with increasing train speed v. On the right, the standard load case is compared with load case 6 (heavy haul) and load case 7 (rigid support). For the heavy haul case, the level of the vertical contact force is generally higher and thus high contact forces arise. For rigid support of the crossing, the amplitudes of the oscillations are increased, causing high contact forces. It can be seen that a stiffer support has a similar effect as higher train speeds.

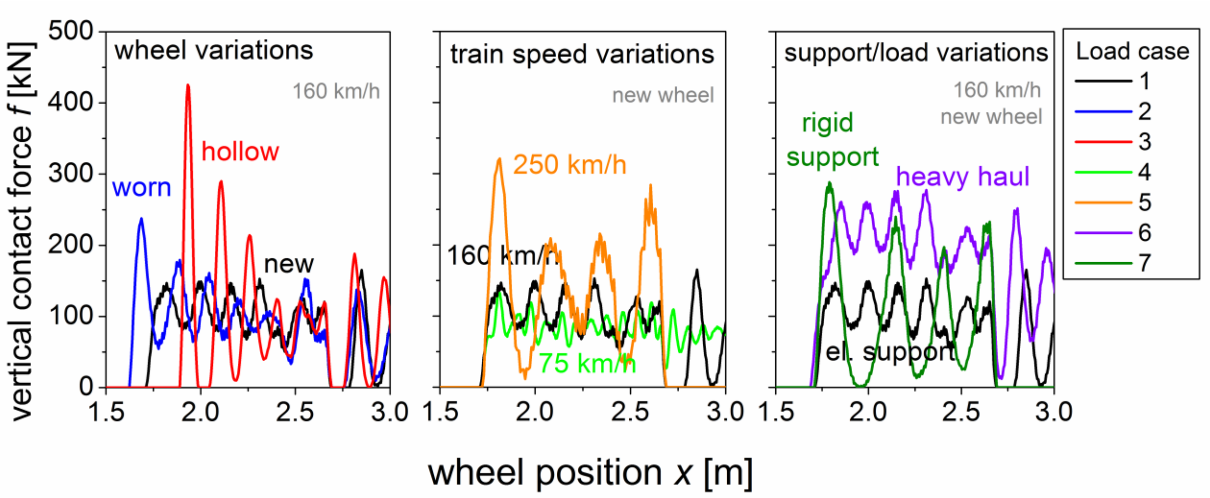

Figure 9: The vertical contact forces of all seven load cases. On the left, the three wheel profiles are shown, in the middle the three train speeds and on the right the cases with higher axle load and rigid support. The region of the crossing nose is shown (wheel position of 1.5 m to 3 m)

The important factor for the damage is not the impact force but the contact pressure. Since the contact situation of wheel and crossing changes throughout the wheel's run over the crossing, a given contact force causes different pressures at different positions. The contact radius of the crossing (R_c) is defined in Figure 10. According to the theory of Hertz [6, 7], the maximum elastic contact pressure p_0 is influenced by the impact force f_{imp} and the contact radius R_c of the crossing according to

$$p_0 \propto \sqrt[3]{\frac{f_{imp}}{R_c^{\ 2}}} \tag{3}$$

This means that a smaller contact radius R_c (as is the case at the tip of the crossing) leads to significantly higher contact stresses than a larger contact radius (at the wing rail, at the crossing nose far away from the tip). To give an idea about these dependencies, two cases of contact forces and contact radii can be put into equation 3: Increasing f_{imp} from 150 to 300 kN (100%) increases the contact pressure by 26%. Lowering the contact radius R_c from 6 to 3 cm (-50%) increases the contact pressure by 59%.

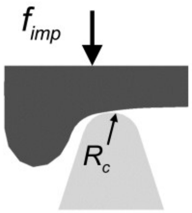

Figure 10: Definition of the contact radius of the crossing nose R_c.

Figure 11 shows the maximum contact pressures p_0 for all investigated load cases arising in the crossing nose during the impact. Generally, the peaks of the contact pressures and the contact forces are at the same position but there is a tendency to lower contact pressures towards larger wheel positions (increasing contact radius R_c), as equation 3 predicts. For the different wheel profiles which impact at different positions, the effect of the contact radius is important. The contact pressures produced by the hollow wheel (load case 3) are lower than the contact pressures of the worn wheel (load case 2), even though the hollow wheel drops onto the crossing nose and thus causes very high contact forces.

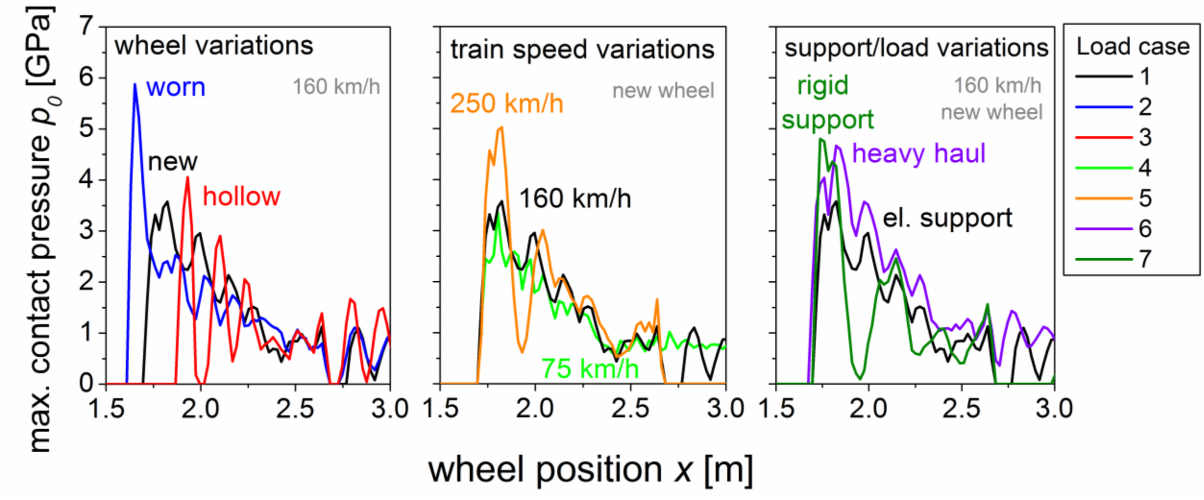

Figure 11: The highest arising contact pressures on the crossing nose for all the calculated load cases.

3.2 Angular Velocity of Wheel – Slip

The changing contact radius of the wheel running over the wing rail and the crossing nose produces a moment on the axle since the longitudinal velocity of the wheel cannot change and the change of the angular velocity is constrained. This moment tends to change the angular velocity of the axle ω towards a ω_f that corresponds to a free rolling wheel, where ω_f is calculated as the train speed v divided by $R_{f,}$, which denotes this contact radius for free rolling wheel. The inertia of the wheel set and the contact of the second wheel of the wheel set partly hinder that adaption of ω. As the wheel impacts with the crossing nose, it contacts usually at the same time at two points: One on the wing rail (with a radius of R_{wr}) and one on the crossing nose (R_{cn}) The angular velocity of the wheel set tends to adapt to this contact radius R_{cn} . This process is partly hindered by the second wheel of the axle, which runs on the regular rail. Any misfit between the angular velocity ω and the wheel radius R_f causes slip. As long as the wheel is not driven or brakes, this misfit is the main cause of slip when the wheel changes from the wing rail to the crossing nose. As the radius of the wheel at the point contacting with the wing rail R_{wr} is smaller than the radius at the point contacting with the crossing nose R_{cn}, the angular velocity is increased before and decreased during the impact of the wheel onto the crossing nose.

Before the wheel impacts with the crossing nose the wheel adapts and increases its angular velocity due to its decreasing contact radius on the deviating wing rail but depending on the time available and its rotational inertia, the adaption is not always complete. The more complete this adaption works out the higher is the resulting slip during the impact.

As a maximum value of the slip during impact, it can be assumed that the angular velocity of the axle fully adapts to R_{wr} and then it adapts to the radius R_{cn} on the crossing nose. Using the definition of Carter for the slip s [8], in which the velocities are expressed by the rolling radii, the maximum possible slip s_{max} can be written as

$$s_{\max} = \frac{2\left(R_{cn} - R_{wr}\right)}{R_{cn} + R_{wr}} \tag{4}$$

This maximum possible slip s_{max} depends on the wheel profile, too. Less conicity allows for less slip and higher conicity will produce a higher s_{max}. In Table 2, the wheel radius on the wing rail, the crossing nose, their difference $\Delta R = R_{cn} - R_{wr}$ and the resulting s_{max} are shown. It can be seen that the worn wheel allows with a value s_{max} of 0.94% for more slip than the standard load case with 0.88%. For the hollow wheel a s_{max} of 0.46% is calculated.

Table 2: The radii of the different wheels during the impact - R_{wr} on the wing rail and R_{cn} on the crossing nose. The difference between these radii is called ΔR. The maximum possible slip according to that radius difference s_{max} is shown for the three wheel profiles.

Wheel profile	R_{wr} [mm]	R_{cn} [mm]	ΔR [mm]	s_{max} [%]
New	497.2	501.6	4.4	0.88
Worn	497	501.7	4.7	0.94
Hollow-worn	497.5	499.8	2.3	0.46

In reality, this full adaption of the wheel's angular velocity to R_{wr} before the impact does not occur to this extent. In Figure 12, the angular velocity of the wheel set for the standard load case is shown together with the fictitious angular velocities for the assumption of a free rolling of the wheel on the wing rail (ω_{wr}) or the crossing nose (ω_{cn}). It can be seen that before the impact, the wheel set tends to increase its angular velocity by $\Delta\omega$, but does so only to a certain extent. The difference between ω and ω_{cn} at the impact produces the slip. This means that lower $\Delta\omega$ values cause less slip. The dynamic equation for angular motion states that an angular acceleration ¿ can be calculated from the moment on the axle *M* divided by the moment of inertia *I*. Disregarding the second wheel of the wheel set, which runs on a straight regular rail, ¿ can be written as $f_0\mu R / I$, where f_0 is the static wheel load, μ the coefficient of friction between the wheel and the wing rail and *R* the wheel radius. The change $\Delta\omega$ can be approximated by multiplying ¿ with the time *t* that the moment acts (which is the time that the wheel runs a distance *l* on the wing rail). The lower the train speed, the longer the time t on the wing rail ($t=l/v$). This gives the proportionality of the change of the angular velocity of the wheel set as:

$$\Delta\omega \propto \frac{f_0 \; \mu \; R}{I \; v} \tag{5}$$

It follows from relation 5 that $\Delta\omega$ and thus the slip is larger for higher axle loads f_0, higher coefficients of friction μ, larger wheel radii, lower velocities *v* and lower wheel set inertias.

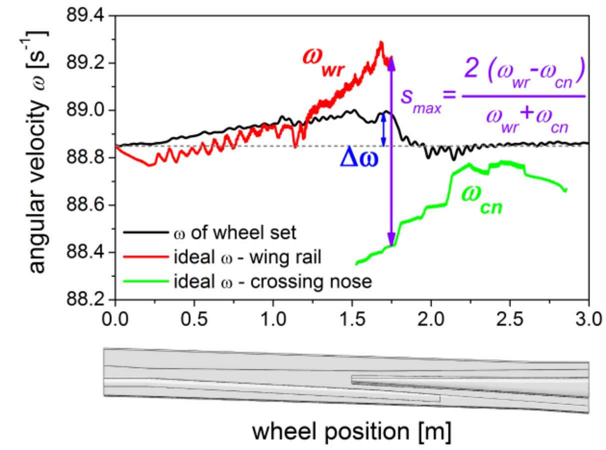

Figure 12: The angular velocity of the wheel for the standard load case. The change of the angular velocity prior to the impact is called $\Delta\omega$ and shown in the diagram.

Figure 13 shows the calculated angular velocities for all load cases as the wheel runs over the crossing. On the left, the calculations for three wheel profiles are compared. It can be seen that the wheel's angular velocity increases more before the impact in the case of the worn wheel (load case 2) than for the new wheel, which is a result of its higher conicity. The hollow wheel (load case 3) changes its angular velocity only little before the impact as the rolling radius of the wheel does not change as much. Regarding the train speeds, the dependency of relation 5 can be seen in the central diagram of Figure 13. The adaption of the angular velocity $\Delta\omega$ becomes more distinctive for lower train speeds. The higher $\Delta\omega$ for higher axle loads can be seen in the right diagram of Figure 13, where the angular velocity of the axle increases most in load case 6 (heavy haul). The load case 7 with rigid support of the crossing causes oscillations of the angular velocity compared to the standard load case, which are excited by the vertical oscillations.

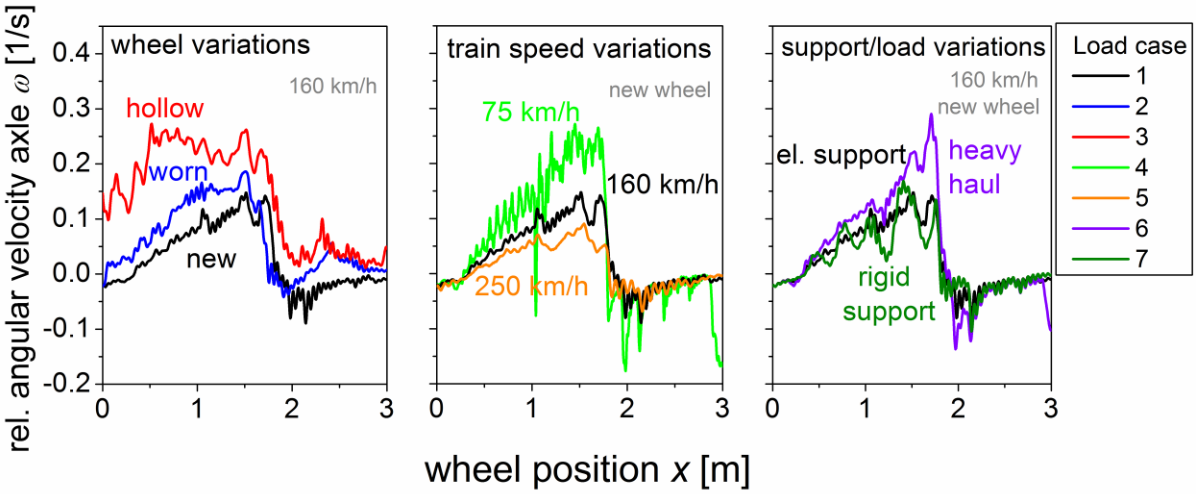

Figure 13: The relative angular velocities along the wheel position for all load cases.

As shown in Figure 12, the slip can be calculated from the values of the angular velocity of the axle ω and the angular velocity for free rolling of the wheel on the crossing nose ω_{cn}. This can be done in the same way for the wing rail.

Finite element results of the slip *s* on the crossing nose are shown in Figure 14. Comparing the three wheel profiles, it can be seen that the new wheel profile (standard load case) causes the highest slip with a maximum of 0.65%. For the worn wheel (load case 2), the slip is slightly lower with a maximum of 0.55%. The hollow wheel (load case 3) produces very little slip, which becomes even negative because of the reversed conicity of the hollow wheel. The higher $\Delta\omega$ at lower train speeds causes the slip to increase with decreasing train speed. In the right diagram of Figure 14, it can be seen that the slip for the rigid support (load case 7) is nearly identical to the elastically supported standard load case. Load case 6 (heavy haul) produces also higher slip due to the higher $\Delta\omega$.

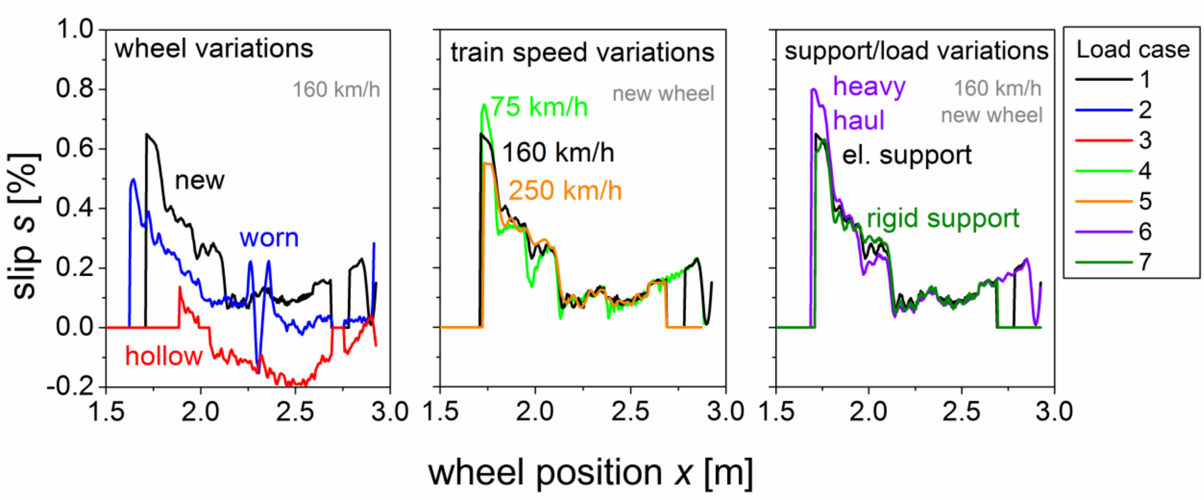

Figure 14: The slip for the seven load cases.

3.3 Contact pressure and slip of all load cases

As damage is related to the arising values of contact pressure and slip their maximum values are shown in Figure 15 for all load cases. The position of the plotted points indicates their type and level of loading. Towards the upper right corner of the diagram the overall loading of the crossing increases, featuring the highest potential for damage on the crossing nose. For the load cases of Figure 15 Table 3 gives relevant calculated load values and parameters.

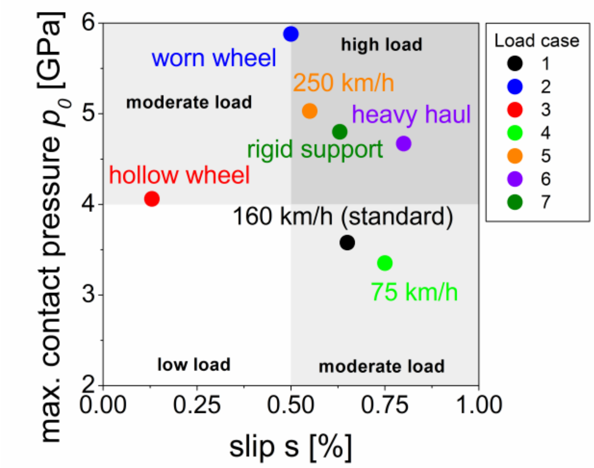

Figure 15: The maximum contact pressures of the impact and the corresponding slip of all load cases plotted in one diagram.

From Figures 11 and 15 it can be seen that the contact pressures in the models reach maximum values between 3 and 6 GPa. The maximum contact pressure clearly rises with increasing train speed. Load case 7 with rigid support produces clearly higher contact pressures than the elastically supported standard load case. Also, the load case 6 (heavy haul) produces higher contact pressures. The highest maximum contact pressures of all seven load cases are produced by load case *2* with the worn wheel, where due to the worn outer wheel tread the wheel impacts earlier on the narrow part of the crossing nose. Load case 3 with the hollow wheel, although producing very high contact forces, shows only slightly higher contact pressures than the standard load case.

The slip is mainly influenced by the wheel profile. For the worn wheel, the slip is reduced compared to the standard load case. For the hollow wheel, the slip is reduced even more because of its low wheel tread conicity. Lower train speeds produce higher slips because of the better adaption of the angular velocity of the axle as predicted by relation 5. Load case 6 (heavy haul) shows also higher slip than the standard load case. This is due to the enforced adaption of the angular velocity to the rolling radius on the wing rail by higher axle loads. It has to be remarked that not only the slip *s* should be regarded but also the slip velocity, which is higher at higher train speeds and can be calculated from the shown results.

Table 3: Results of the seven load cases. The impulse P is calculated using equation 1. The impact force f_{imp}, the impact position x_{imp}, the highest contact pressure p_0 and the slip s associated with the impact are results from the finite element model.

Case		Impact angle α [°]	m_{wheel} [kg]	Impulse *P* [kg m/s]	Impact force f_{imp} [kN]	Impact position x_{imp} [m]	p_{0max} [GPa]	Slip s during impact [%]
1 - standard	160 km/h	0.35	1025	278	147	1.82	3.58	0.65
2	Worn wheel	0.86	1025	684	430	1.93	5.88	0.5
3	Hollow wheel	0.66	1025	525	238	1.65	4.06	0.13 (-0.2)
4	75 km/h	0.35	1025	130	134	1.80	3.35	0.75
5	250 km/h	0.35	1025	435	321	1.82	5.02	0.55
6	Heavy haul	0.35	1500	407	260	1.82	4.67	0.8
7	Rigid support	0.35	1025	278	288	1.74	4.8	0.63

4 The role of plastic material behaviour

The crossing material plays an important role in what kind and to what extent damage occurs. A model that can predict the performance of a crossing depending on the material must somehow regard the plastic material behaviour of the crossing. In the following a method for describing effects due to the plastic deformation of the crossing nose is presented. Two selected materials with significantly different plastic stress strain curves are compared, see Figure 16a. Details about the material modelling methodology are given in **Paper C** and **Paper D**.

Due to the high numerical efforts the previously described three metre crossing model does not allow for cyclic calculations. On the one hand, calculation times would explode and on the other hand, the finite element mesh of the crossing nose remains too coarse to accurately model the effects of cyclic loading which mainly influences (a) the change of the contact stresses due to the geometry change and (b) the build-up of residual stresses. Therefore, a reduced model with only the wheel and the crossing nose (the *impact model*) was developed allowing for detailed investigations. It is shown in Figure 16b. The wheel can now repeatedly be moved on the crossing nose using loads and kinematic conditions from the previous model and applied in this impact model. The presented results are taken after 81 cycles of wheel impacts at four different positions to account to some extent for the statistically distributed loading of the crossing nose.

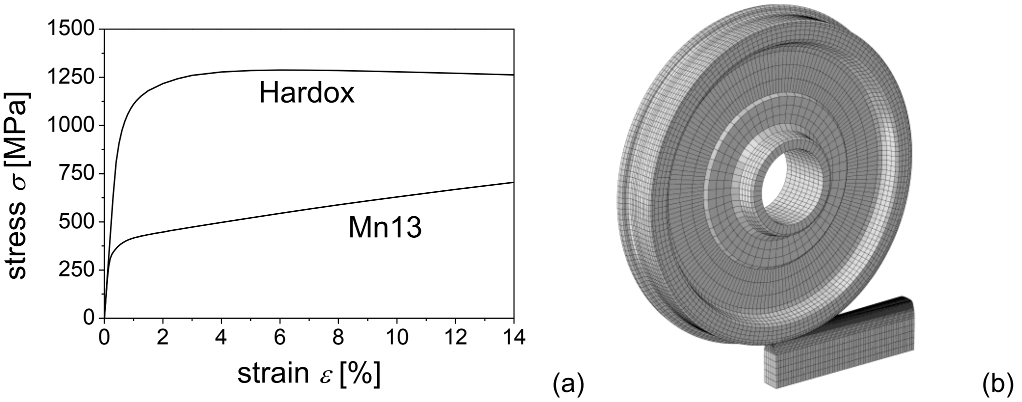

(a) (b)

Figure 16: a) The stress-strain curves for the two presented materials and b) the geometry of the impact model.

As the yield stress of Mn13 is lower than the yield stress of Hardox, more plastic deformation and less contact stresses are produced in the Mn13 crossing. This is illustrated in Figure 17a, where the contour plot of the vertical stresses in the 81st cycle of loading is shown in the cross-section of the highest contact pressures. It can be seen that the Mn13 crossing has severely adapted to the loading (bigger contact patch) and thus reduced the vertical contact stresses to about 1000 MPa. For Hardox, having plastically deformed less than Mn13, this effect is less pronounced with vertical stresses of about 2000 MPa.

In Table 4, the results of the 81st cycle of loading are shown. Figure 17b shows a contour plot of the residual stress component in the longitudinal direction in the crossing nose for both materials. Under the surface, compressive stresses develop in both materials. In the Hardox crossing nose, they are higher and closer to the surface (-500 MPa in a depth of 3 mm) than in the Mn13 crossing nose (-200 MPa in a depth of 6 mm). Below the area of the compressive stresses, there are some tensile stresses which are below 150 MPa for both materials.

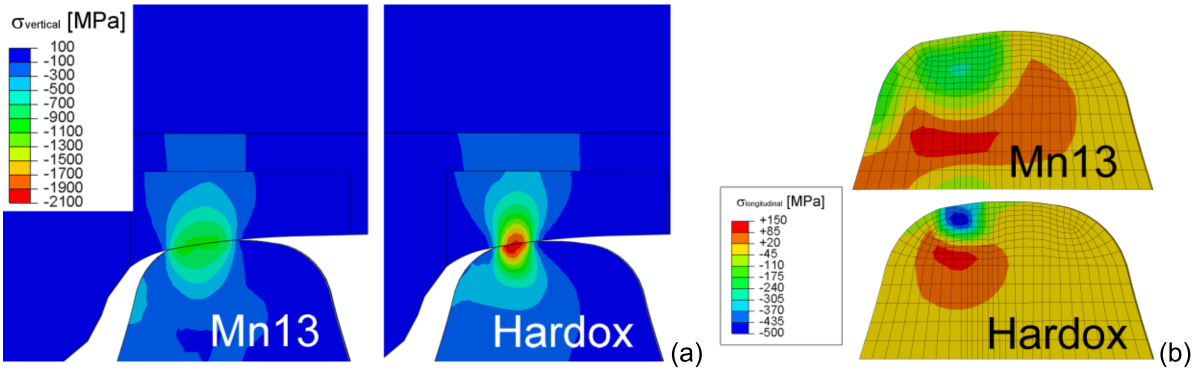

Figure 17: a) Contour plots of the vertical stresses S22 in the cross-sections at the wheel position producing the highest contact pressure for the two crossing materials Hardox and Mn13. It can be seen that Hardox reaches compressive stresses of up to 2000 MPa whereas the Mn13 only reaches stresses of about 1000 MPa. b) Contour plots of the longitudinal residual stresses in the crossing nose after 80 cycles of loading.

Working with a hierarchical modelling system from global to a near micro description these results can now be applied in a two-dimensional model. In addition to the maximum contact pressure p_0, the half longitudinal contact length a and the slip s are needed as input values for a further dimensional reduction of the model.

Table 4: The loads from the 81st cycle of loading for the two crossing materials Hardox and Mn13.

	Max. contact pressure p_{max} [MPa]	Half contact length a [mm]	Slip [%]
Hardox	2020	11	0.3
Mn13	1063	9.2	0.28

5 Studying the loading of a surface crack

Micro-models investigating crack initiation and crack growth represent one step towards a deeper understanding of damage phenomena. The results of the contact pressures, slips and contact patch sizes of the impact model (see Table 4) can be transferred to a two-dimensional model that contains a surface crack (this crack model is shown in Figure 18). With the crack model, the loading of the crack can be calculated in terms of the crack driving forced represented by the calculation of the J-integral (J_{tip}) based on the concept of configurational forces. This method also predicts a direction of crack propagation. The modelled crack has an angle α_c of 30° and a crack depth a_d of 1 mm. The calculated J-integral is shown in Figure 19a for Mn13 and 19b for Hardox as the wheel runs over it.

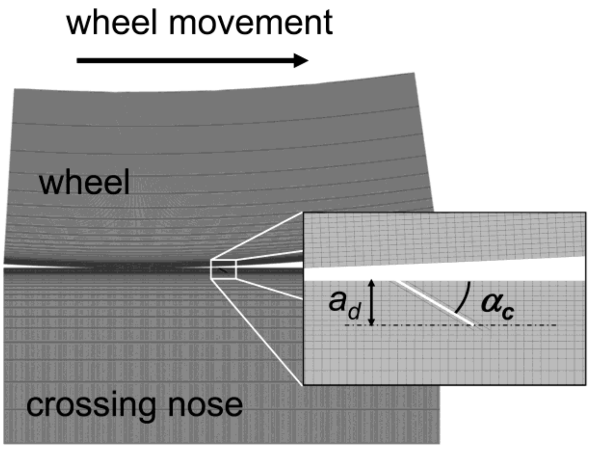

Figure 18: FE mesh of the crack model.

The results of the crack model are shown with and without applied residual stresses. In Figure 19, the J- Integral J_{tip} is plotted over the wheel position. At a wheel position of 0 mm, the wheel centre is directly located over the crack tip. The wheel moves from the left to the right over the crack. For both materials, the highest J_{tip} values are reached after the wheel has completely passed the crack. Regarding the results without residual stresses, the Hardox crossing reaches with a value of 3990 J/m^2 a higher J_{tip} value than the Mn13 crossing with 1980 J/m^2. This is caused by the lower contact pressures of the Mn13 crossing. Applying residual stresses from the impact model has only a small effect on the J_{tip} value for Mn13. For Hardox, the residual stresses clearly reduce J_{tip} to a maximum value of 1560 J/m^2, which is even lower than for the Mn13 crossing. For a prediction of the crack growth rate (e.g. in nm per load cycle), good measurements for crack growth are needed. As currently no measurements under realistic mixed mode conditions exist (highly deformed surface layers and crack propagation in the shear mode - Mode II), no final statement can be made about the suitability of the materials for crossing noses. The model results indicate, however, that the plastic adaption and residual stresses in the crossing can influence the loading of cracks. It shows clearly that only a general approach and integration of all significant parameters in the models can finally produce reliable predictions of a crossing's performance.

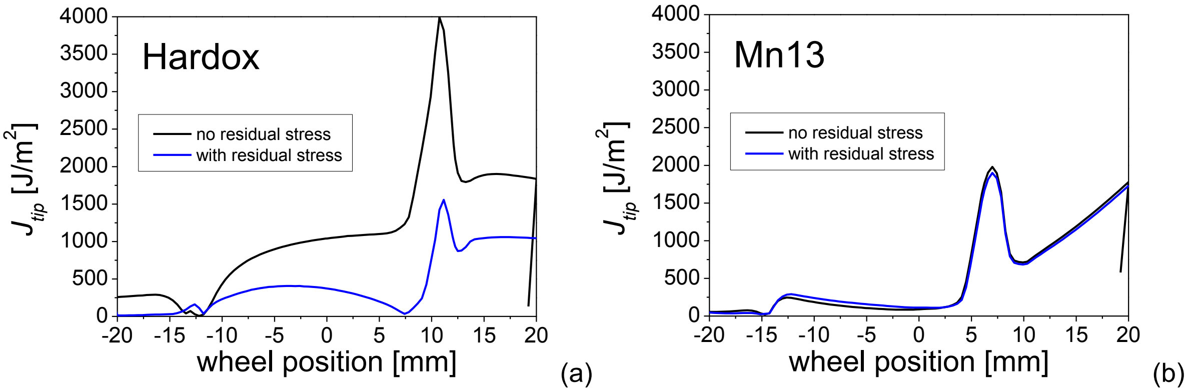

Figure 19: Results of the J_{tip} values in the crack model for c) Hardox and d) Mn13 crossing material.

6 Conclusions

Simplified models supported by results of a dynamic FE model explain how the resulting loads on the crossing nose are caused by parameters such as the wheel profile, trains speed etc. It is commonly assumed that damage is related to the occurrence of contact pressure and slip. The crossing nose is the part of the crossing where the highest amount of damage occurs. The direction in which the wheel runs from the wing rail to the crossing nose is identified as more critical than the opposite direction. Due to the conical wheel tread, the wheel is forced to move vertically as it runs along the crossing. On the wing rail it moves downwards and on the crossing nose it moves back to the initial level. There is a position in which the wheel transits from the wing rail to the crossing nose and the change in the direction of the vertical movement produces an impact with high contact forces. The change from the downward movement to the upward movement during this impact (described by the impact angle α) is an important parameter for the arising contact forces, which is determined by the crossing and the wheel geometry. Contact forces increase with increasing impact angles α, axle loads, train speeds and also for stiffer vertical supports of the crossing. Another important parameter of the impact is its longitudinal position. Hollow wheels impact later on the crossing nose and wheels mainly worn on the outside of the wheel tread earlier. As the crossing nose becomes narrower towards its tip, the earlier impacts produce higher contact pressures.

The conicity of the wheel influences the described vertical movement and also angular velocity of the wheel. The wheel always attempts to change its angular velocity towards free rolling. The angular velocity of free rolling is determined by the wheel radius and the train speed. A lower contact radius needs a higher angular velocity for free rolling. The angular velocity of the wheel as it runs through a crossing panel is thus increased on the wing rail (the contact radius of the wheel decreases) and accelerated on the crossing nose. During the transition of the wheel from the wing rail to the crossing nose, the wheel contacts both wing rail and the crossing nose. From the difference in the wheel radii at these two contact points, a maximum possible slip s_{max} can be calculated. This difference of the radii and thus the maximum slip is higher for higher conicities of the wheel treads- The maximum possible slip on the crossing nose is thus higher for wheels worn on the outside of the wheel tread and lower for hollow-worn wheels.

In reality, the wheel does not fully adapt to its angular velocity for free rolling on the wing rail and thus less slip than s_{max} is produced on the crossing nose. Therefore, this adaptation is influenced by various parameters and the slip thus decreases with higher train speed, higher rotational inertias of the axle, lower axle loads, lower wheel radii and lower coefficients of friction between the wheel and the wing rail.

The high contact pressures calculated with the models using elastic behaviour of wheel and rail indicate that there will be plastic deformation of the crossing nose due to the contact loading. The amount of deformation is of course depending on the material of the crossing. Since material selection for crossing noses is an important issue, the effect of the plastic material behaviour is studied in a model for the repeated loading of a crossing nose. It is shown that the plastic deformation changes the geometry and usually lowers the contact pressures on the crossing nose (the crossing adapts towards the wheel profile). This effect is more distinctive for materials with lower yield stresses. Also, the plastic strains cause residual stresses in the crossing, which are mainly compressive close to the surface. The materials with higher yield stresses produce higher compressive residual stresses in the crossing nose which are located closer to the surface than in materials with lower yield stresses. The compressive stresses on the surface reduce crack growth rates if cracks exist. In a model that calculates the loading of a one mm deep surface crack, the effect of the reduced loading by the geometric adaption of the crossing and the influence of residual stresses on the crack driving force is shown.

Acknowledgements

Financial support by the Austrian Federal Government (in particular from the Bundesministerium für Verkehr, Innovation und Technologie and the Bundesministerium für Wirtschaft und Arbeit) and the Styrian Provincial Government, represented by Österreichische Forschungsförderungsgesellschaft mbH and by Steirische Wirtschaftsförderungsgesellschaft mbH, within the research activities of the K2 Competence Centre on “Integrated Research in Materials, Processing and Product Engineering”, operated by the Materials Center Leoben Forschung GmbH in the framework of the Austrian COMET Competence Centre Programme, is gratefully acknowledged.

References

[1] E. Kassa, J. Nielsen, Dynamic interaction between train and railway turnout: full-scale field test and validation of simulation models, Vehicle System Dynamics, 46 (2008) 521-534.

[2] J.F. Archard, Contact and rubbing of flat surfaces, Journal of Applied Physics, 24 (1953) 981-988.

[3] A. Ekberg, E. Kabo, Fatigue of railway wheels and rails under rolling contact and thermal loading-an overview, Wear, 258 (2005) 1288-1300.

[4] H. Jahed, B. Farshi, M.A. Eshraghi, A. Nasr, A numerical optimization technique for design of wheel profiles, Wear, 264 (2008) 1-10.

[5] F.D. Fischer, E.R. Oberaigner, W. Daves, M. Wiest, H. Blumauer, H. Ossberger, The Impact of a Wheel on a Crossing, ZEVrail Glaser Annalen, 129 (2005) 336-345.

[6] H. Hertz, Über die Berührung fester elastischer Körper, Journal für die reine und angewandte Mathematik, 92 (1881) 156-171.

[7] J. Kunz, Kontaktprobleme und ihre praktische Lösung, Konstruktion, 61 (2009) 54-58.

[8] F.W. Carter, On the action of a locomotive driving wheel, Proceedings of the Royal Society of London, A 112 (1926) 151-157.

Paper A

A Wheel Set / Crossing Model Regarding Impact, Sliding and Deformation- Explicit Finite Element Approach

M. Pletz
W. Daves
H. Ossberger

Submitted to
Wear

A Wheel Set / Crossing Model Regarding Impact, Sliding and Deformation- Explicit Finite Element Approach

M. Pletz[1,2], W. Daves[1,2], H. Ossberger[3]

[1]Materials Center Leoben Forschung GmbH, Leoben, Austria
[2]Institute of Mechanics, Montanuniversität Leoben, Leoben, Austria
[3]VAE GmbH, Zeltweg, Austria

Abstract

A dynamic finite element model for the process of a wheel passing the crossing panel of a turnout is presented. This model accounts for the dynamic process, the elastic deformations of the wheel and the elastic-plastic deformations of the crossing. The axle and the second wheel are represented in terms of their influence on the angular velocity of the wheel.

The model provides the dynamical contact forces between the wheel and the crossing parts, the vertical wheel displacement, the development of the angular velocity of the wheel as well as the stress fields and the plastic deformations in the crossing. Results that indicate the loading of the surface, such as the contact pressure and the microslip, are also provided by the model. From them, the frictional work and the maximum of the frictional power are derived. Those values are associated with surface damage such as wear and Rolling Contact Fatigue (RCF). An empirical relationship between the frictional work and wear is widely used and called Archard’s wear law. For the formation and propagation of surface cracks there is no simple relationship.

Results for the wheel initially running on the wing rail and then impacting onto the crossing nose (facing move) and the other direction (trailing move) are presented for three velocities.

The presented model can help in the optimization of crossings in terms of geometry, bedding and material, depending on the loading conditions such as train velocity, axle load and wheel profile for both the facing and trailing move.

1 Introduction

Turnouts are an important part of the railway track system. They consist of a switch and a crossing panel. In the crossing panel there is a discontinuity in the rail, which causes a high dynamic loading. This impact loading of the crossing panel is investigated in this work.

In Figure 1, a crossing is shown and the different parts are highlighted. As it can be seen, the wheel has to change from running on the wing rail to the crossing nose (facing move) or vice versa (trailing move).

Recently, demands on the track structure have increased. Higher velocities and axle loads are used which can cause severe problems concerning damage in the crossing. New geometric or material concepts for crossings can meet these increased demands.

The process of a wheel passing a crossing panel, however, is highly complex, including dynamic effects with contact and complex geometries. Optimization and the introduction of new technologies thus cannot be done intuitively. Field tests can be carried out to investigate the performance of crossings in the track, and are done prior to the wide usage of new crossing concepts.

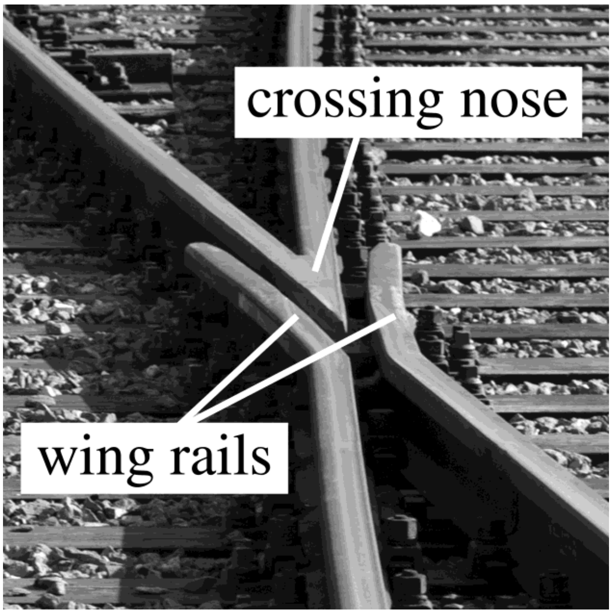

Figure 1: Typical manganese steel crossing

In the development of new concepts or the improvement of existing ones, numerical models can help to shorten development times. This can be done both by predicting the performance of possible design concepts and improving the understanding of the mechanisms of loading.

According to previous finite element (FE) studies [1], the contact forces between the wheel and the crossing nose reach values from two to four times the static wheel load for the investigated geometrical conditions and velocities. The forces during the impact are estimated to be more than seven times the static wheel load in analytical calculations assuming elastic material [2].

These large contact forces between wheel and rail can cause severe damage at crossing noses. Out of these reasons great efforts should be undertaken in decreasing the dynamic response between wheel and track. A mass-spring model for the analysis of an elastic-plastic beam on a foundation subjected to mass impact is presented by Yu et al. [3]. Recent analytical investigations using mass spring models are performed by Fischer et al. [4, 5]. Li et al. [6] developed a model in which ballast and subgrade are modelled separately by two-dimensional finite elements to enable the investigation of the effect of track and vehicle parameters on vertical dynamic wheel-rail forces. Nielsen and Igeland [7] present a technique for solving problems concerning the vertical dynamic interaction between a moving vehicle and a track structure discretized by finite elements. With numerical calculations based on multibody dynamics, as performed by Kassa for a train running through a complete turnout [8], the deformability of wheel set material and rail material is usually neglected. Following Nielsen et al. [9], multibody dynamics models fail to represent high frequency train-track interaction. The classification of the response of the crossing to the impact in a “high frequency contact process” and a “low frequency bending process” is outlined in [10] and clearly shown in [11]. Andersson and Dahlberg presented in [12] and [13] a very extensive study applying a sophisticated system of finite elements for the turnout.

Stress and strain analyses are the key to understand and predict the wear and fatigue behaviour of contacting and impacting bodies. Johansson [14] performed a calculation on a section of a crossing nose loaded by a Hertzian contact pressure distribution. There exists a lot of work in the literature on the topic of wheel-rail contact calculations. The majority of them use simplifications. Saulot and Baillet [15] use a two-dimensional FE model to investigate contact dynamic instabilities. A three-dimensional FE model of a rail, on which they applied moving contact pressure distributions according to Hertz [16] and the analysis tool CONTACT [17], is presented by Ringsberg and Josefson [18]. Sladkowski and Sitarz [19] as well as Telliskivi and Olofsson [20] applied global forces calculated by multibody dynamics programs to the wheel centre of their three-dimensional FE models of wheel and rail.

The cyclic response of a crossing is analysed by Yan et al. [21]. A very sophisticated three-dimensional dynamic simulation of a wheel impacting on the rail joint region is performed by Wen et al. [22]. The common criticism on the FE studies of Yan et al. as well as of Wen et al. might be that the rolling of the wheel is neglected. Finite element simulations, reflecting the three-dimensional contact combined with dynamical rolling of the three-dimensionally modelled wheel and rail including elastic-plastic material properties are done by Wiest et al. in [1, 23, 24, 25].

A representation of the realistic geometry of wing rail and crossing nose was archived by the authors due to increased computing power in combination with the established knowledge about modelling the complicated and highly dynamic transition process.

In [26, 27], a model containing the realistic geometry of the crossing parts and a representation of the whole wheel set is presented. The results of the facing move are presented there.

The presented model, being based on an explicit finite element formulation, has certain limitations:

- high calculation times (5-48 h/cycle) compared to multibody system methods,
- only a length of 3 metres of the crossing is modelled,
- assumptions about the wheel position (fixed lateral position, no steering of the bogie).

Using the present model allows for calculating the realistic slipping between the wheel and the wing rail and the crossing nose depending on

- the angular velocity of the wheel,
- the contact positions of the wheel on the crossing parts (wing rail and/or crossing nose),
- the geometry of the involved parts,
- the plastic material behaviour of the crossing parts,
- the inertia of the bodies.

The dynamical loading of the crossing in combination with the slip between the wheel and the crossing parts can lead to wear, rolling contact fatigue and severe plastic deformation of the crossing. The dynamic situation can be illustrated by the developments of the contact forces and the angular wheel velocity. Damage, however, is related to the local contact situation with the pressure and microslip (local tangential velocity difference of contacting surfaces) that cause stresses and plastic strains in the crossing parts.

In this work, the accumulated equivalent plastic strain after one crossover is calculated to indicate the loading of the material in terms of plastic deformation, e.g. ratchetting.

The frictional work is widely used to calculate wear, e.g. based on Archard’s wear law [28]. It is thus evaluated in the presented model.

Archard’s law, however, is based on experimental data and a wear coefficient is only valid for one microslip/pressure combination. Krause and Poll [29] state that the frictional power per surface area indicates the shift between different wear mechanisms with different wear coefficients. The maximum occurring frictional power per surface area is thus also evaluated in this work.

2 Finite Element Model

2.1 Setup of the model

The finite element model represents the full three-dimensional geometry of one wheel, the crossing nose and the wing rails (see Figure 2a-d). The crossing model represents a manganese cast crossing of the standard design 760-1:15 for a UIC60 rail. The wheel (UIC-ORE 1002 Profile) is modelled using elastic material properties save for the hub with a radius of 116.5 mm which is considered rigid (see Figure 2d). To ensure a proper description of the dynamic process, the rigid plate is used for representing the mass of the remaining part of the first wheel and the moment of inertia of the remaining part of the first wheel, the axle and the second wheel.

In Figure 3, the mechanical model illustrating the assumptions of the presented crossover calculation is shown. The parts of the model which are represented by explicit finite elements are dark grey and denoted by (Ia) and (Ib). The bottom of the crossing is rigidly connected to a parallel spring/damper combination, giving a rough representation of the crossings bedding (II). For the initial positioning of the wheel on the rail, the wheel centre is connected to a vertical damping element that removes initial oscillations of the contact force (III), as described in [23]. An initial damping coefficient k_p of 4×10^6 Ns/m is used and then reduced to a value of 53 000 Ns/m, which is a realistic value for the primary suspension of the bogie. The wheel centre is connected to a frictional element (rotation around the x- axis) that represents the second wheel and is described in section 2.2.

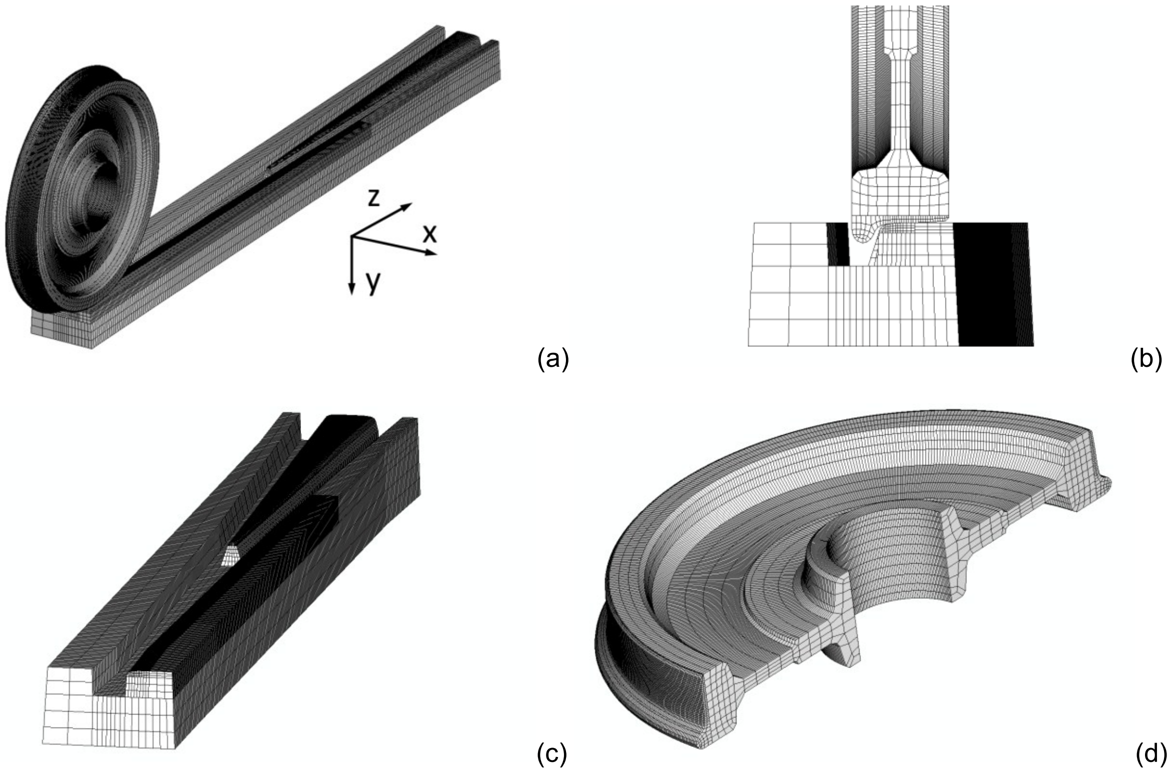

(a) (b)

(c) (d)

Figure 2: Finite element model: (a) Wheel and crossing, (b) cross section, (c) crossing parts and (d) wheel mesh.

In the centre of the wheel, the used coordinate system is shown. The x-axis denotes the lateral direction, y the vertical direction and z the longitudinal. The reference point of the rigid axle of the wheel is positioned in the origin of the coordinate system. In this point, loads are applied on the wheel. The wheel's rotation in the z and y direction is disabled. Also, the wheel is held in the x (lateral) direction on a position that corresponds to the second wheel running along the check rail. In the z (longitudinal) direction, the wheel centre, the vertical dashpot and the rotational frictional element are moved with a constant velocity. A point mass is attached to the centre of the wheel so that the wheel has a total mass of 1025 kg. The moment of inertia of the two wheels and the axle about the x-axis of 135.5 kgm^2 is provided at the reference point.

In the x- direction, an initial angular velocity is applied in the wheel around its centre.

The angular velocity during the transition process is not constrained, thus representing a free rolling wheel.

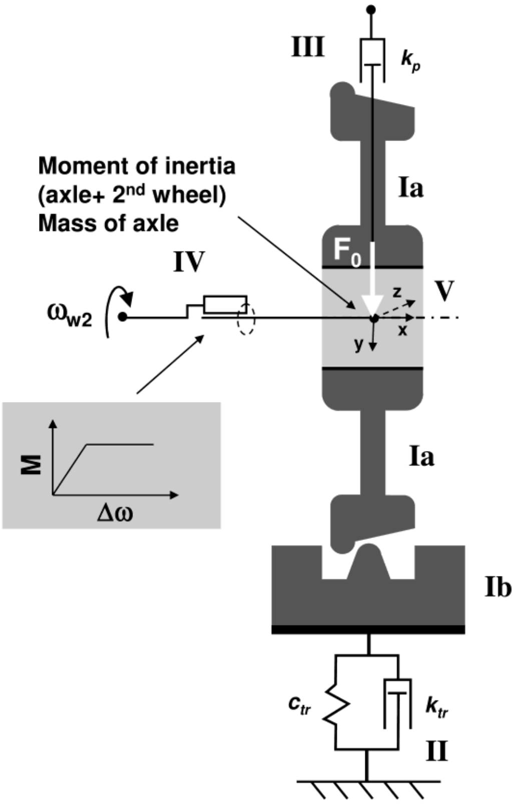

Figure 3: The mechanical model for the wheel and the crossing. (I) The parts of the wheel and the crossing that are calculated using finite elements (dark grey), (II) the representation of the crossing's bedding, (III) the vertical damping element attached to the wheel, (IV) the rotational frictional element with a schematic moment- angular velocity curve and (V) the coordinate system used in the model.

The manganese steel crossing is modelled with a length of 3 metres using about 100 000 elements. The total number of elements in the model amounts to 250 000. The calculations are performed using the finite element code ABAQUS/Explicit [30]. The mesh-size of the hexahedral elements in contact is not larger than 3 mm. This mesh size ensures a correct description of the contact forces and slipping behaviour. However, it will still create some quantitative errors in the results of stresses and strains. The used material data for the wheel (elastic) and crossing parts (Mn13) are printed in Table 1. A friction coefficient of 0.3 is assumed between wheel and crossing parts.

The used static wheel load is 79 700 N, corresponding to an axle load of 14.2 tons. The mass of the wheel including half of the axle is set to 1025 kg. The whole mass of the crossing parts, denoted in Figure 3 as (Ib), adds up to 680 kg.

Property	Manganese steel (Mn13)	Wheel (elastic)
Young's modulus [GPa]	190	210
Poisson's ratio [1]	0.3	0.3
Density [kg/m³]	7800	7800
Yield stress [MPa]	360	-

Table 1: Material properties from the tension test.

2.2 Simplified model of the second wheel on the regular rail

A full finite element model of the whole axle with both wheels would lead to unacceptable computation times. From the second wheel, only the effect on the angular velocity of the axle is relevant. Therefore, the second wheel is represented using one single element. This element possesses an angular frictional behaviour, which is described in the following paragraphs.

It is assumed that the second wheel is running along the check rail, which defines the lateral position of the wheel set. Since the regular cross-section of the rail does not change in the longitudinal direction, the second wheel runs with a constant contact radius R_2 throughout the process. With v_0 being the translational velocity of the wheel, a rotational velocity of $\omega_{2,0} = v_0/R_2$ corresponds to the free rolling of the second wheel. Any other rotational velocity produces frictional forces, which tend to change the rolling velocity of the wheel set.

When the whole contact patch between the second wheel and the rail is in full slip, the second wheel produces a torsional moment M on the axle that is given by $M = \mu F_0 R_2$ with μ being the coefficient of friction and F_0 the static vertical load on the second wheel. With small deviations of the rotational velocity of the axle from $\omega_{2,0}$, stick and slip regions within the contact patch develop. A traction–slip relationship has thus to be used for the calculation of the torsional moment M.

To obtain a satisfactory estimate of M on the axle, the second wheel and the rail have been modelled in a separate but similar finite element investigation. Using this model, a fixed rotational velocity of the wheel leads to a corresponding moment on the axle. In Figure 4, the results for this model and the linearised function used for the described frictional element are plotted.

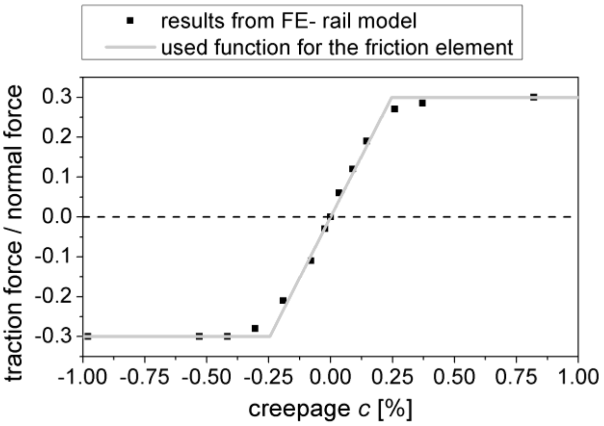

Figure 4: Function used for the traction curve of the second wheel on the regular rail

The longitudinal creepage c is defined by the following relation:

$$c = 2\ \frac{v_t - v_c}{v_t + v_c}$$

with $v_t > 0$ and $v_c > 0$. In this equation, v_t is the translational velocity of the wheel and v_c the circumferential velocity of the wheel, see Carter [31] and Kalker [32]. For small creepages, the creepage can be calculated as the microslip divided by the translational velocity of the wheel.

2.3 Damage related output variables

As damage related variables of the calculation, the accumulated equivalent plastic strain (PEEQ), the microslip and the contact pressure are regarded. Additionally, the frictional work and frictional power produced in the crossings surface are calculated from pressure and microslip. From the contact pressure $p(t)$, the sliding velocity $v_s(t)$ and the coefficient of friction μ, the frictional power $p_f(t)$ can be calculated as:

$$p_f(t) = \mu \cdot p(t) \cdot v_s(t)\,.$$

The dimension of the frictional power is W/m^2. This frictional power $p_f(t)$ is closely related to the maximum arising temperature in the contacting surfaces, since this temperature will be highest while the highest input rate of frictional heat occurs. In the literature [31], however, it is stated that the frictional power also indicates a shift in the wear phenomena. The integral of the frictional power over the time gives the frictional work:

$$w_f = \int_t p_f(t) \cdot dt\,.$$

The frictional work is widely associated with wear. Its dimension is J/m^2. In Archard's wear law [28], for example, the wear depth equals the frictional work times an empirical wear constant divided by the hardness of the material.

3 Results and Discussion

3.2 Dynamic results of the model

In Fig 5, contact forces for the three trains speeds of 75 km/h, 160 km/h and 250 km/h and both facing and trailing move are shown. For the velocity of 160 km/h, the vertical displacements of the wheel centre and the crossing is shown in Figure 6. The results are plotted over the position of the wheel, which ranges from 0 m (wheel on the straight part of the wing rail) to 3 m (wheel on the crossing nose). For all cases, the initial placing of the wheel on the wing rail causes oscillations in the contact force. Vertical displacements of the wheel, however, are only small in this area.

In Figure 5 (a), (c) and (e), the results for the contact force in the facing move are shown. In this direction of passing, first oscillations are excited at a wheel position of 0 m, which depend on the train speed. At a wheel position of 0.2 m, the wing rail starts to deviate. For the wheel, featuring a conical wheel tread, this causes a vertical, downward movement that produces some oscillations in the contact force, depending on the train speed. The amplitudes of these oscillations are reduced along the next metre, caused by dissipation in the vertical damping element of the wheel and the crossings bedding. Plastic deformation plays only a small role in this dissipation. As the wheel approaches the crossing nose (1 m – 1.75 m), some more oscillations occur. They are caused by another change in the vertical movement of the wheel, as it can be seen in Figure 6(a). At a velocity of 250 km/h, the wheel in this area even loses contact with the wing rail - it bounces.

At a wheel position of about 1.75 m, the wheel impacts onto the crossing nose. As the wheels vertical velocity has to change abruptly, oscillations of the contact force arise. Those oscillations, however, are reduced because the wheel is still contacting the wing rail as it impacts onto the crossing nose. In the model with 250 km/h, this effect is only small, and very high contact forces arise. Dissipation in the vertical damper and the contact patch again reduces these oscillations in the following 0.5 m. At a wheel position of 2.7 m, again some oscillations are excited due to the ending ramp of the crossing in the model.

In Figure 5 (b), (d) and (f), results for the contact forces in the trailing move are presented. The train moves in the opposite direction in this case (from right to left in the diagram) and the initial placing of the wheel is on the crossing nose with a wheel position of 2.9 m. At a wheel position of 2.7 m, there is a kink in the crossing nose, causing a downward movement of the wheel and an excitation of oscillations. As the wheel approaches the wing rail, these oscillations become smaller. The wheel changes from the crossing nose to the wing rail at a wheel position of about 1.75 m, producing an impact. At a wheel position of 0.2 m, some oscillations occur due to a change in the rolling plane of the wing rail, which have no significance for the loading of the crossing nose.

As an elastic bedding of the crossing is used in the model, both the vertical displacement of the wheel centre and of the whole crossing can be evaluated. The vertical movement of the crossing is determined by the contact force between the wheel and the crossing, the crossing mass and its bedding. In Figure 6, results of these vertical movements are shown for a train speed of 160 km/h. As the wing rail starts to deviate at a wheel position of 0.2 metres, the wheel starts to lower its vertical position in the facing move (Figure 6a). Up to this position, the spring in the bedding is compressed due to the vertical contact force. As the contact force drops at 0.2 metres, the spring can uncompress and the crossing’s vertical position rises by about 0.2 mm. As the wheel impacts on the crossing nose (at a wheel position of 1.8 metres), the wheel centre moves upward again. As this impact produces increased vertical contact forces, the crossing is pressed down by about 0.8 mm, compressing the spring of the bedding. Towards the end of the model (x = 3 m), the crossing’s and the wheel’s vertical positions approach a similar level as at the start of the simulation.

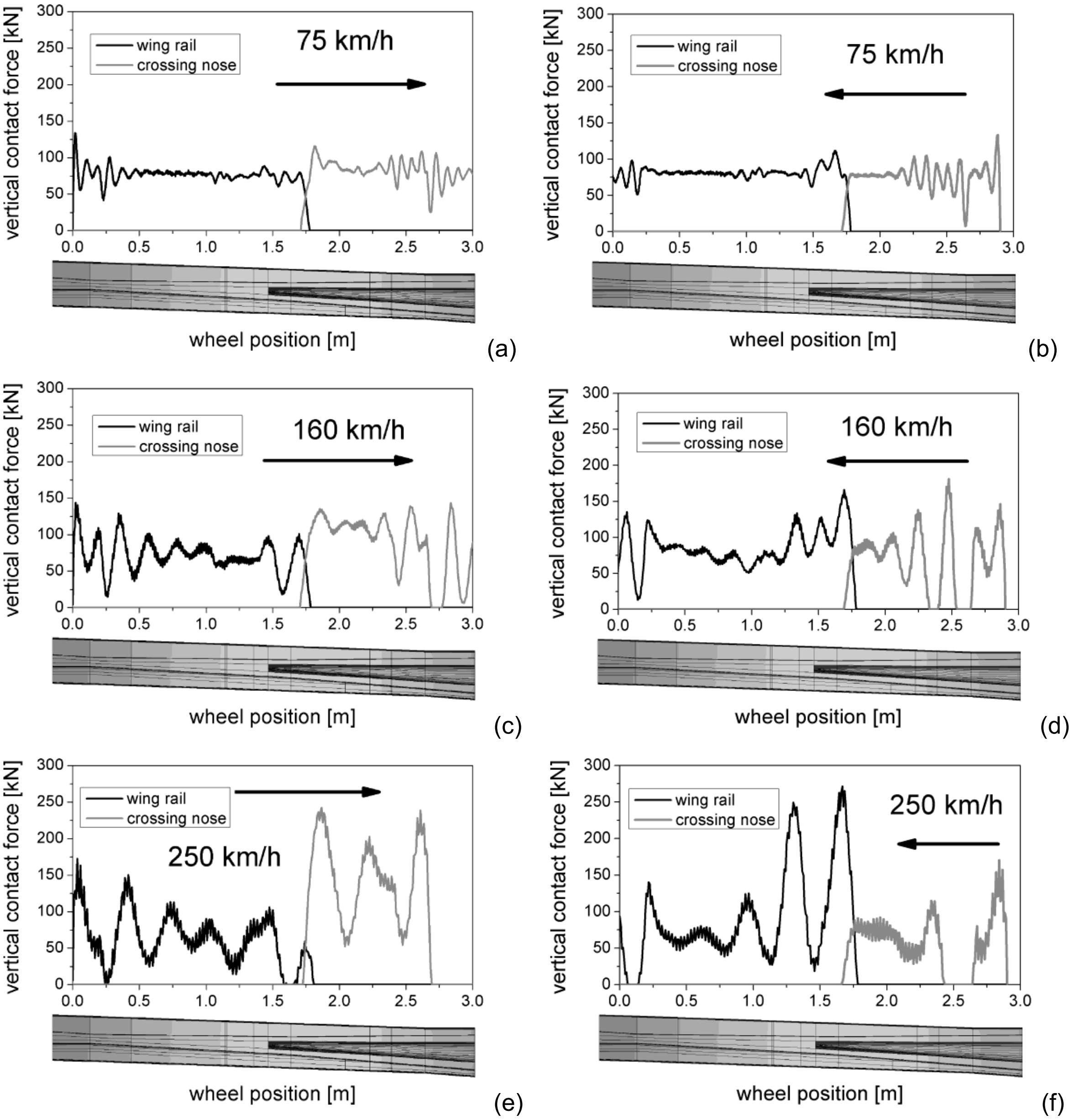

Figure 5: Vertical contact forces between wheel, wing rail and crossing nose. Facing move and a train speed of (a) 75 km/h, (c) 160 km/h and (e) 250 km/h. Trailing move and a train speed of (b) 75 km/h, (d) 160 km/h and (f) 250 km/h.

The movement of the crossing reduces the contact forces compared to a rigidly bedded crossing. The damping element in the bedding of the crossing and its mass decelerate the vertical movement of the crossing. At increased train speeds this effect is more significant adding to increased impact forces at higher train speeds.

In the trailing move similar effects take place. As the wheel starts to move downward at a position of about 2.7 m, the crossing moves upward. The impact in this direction of the wing rail presses the crossing down and both parts approach their initial level at the end of the model (at a wheel position of 0 m).

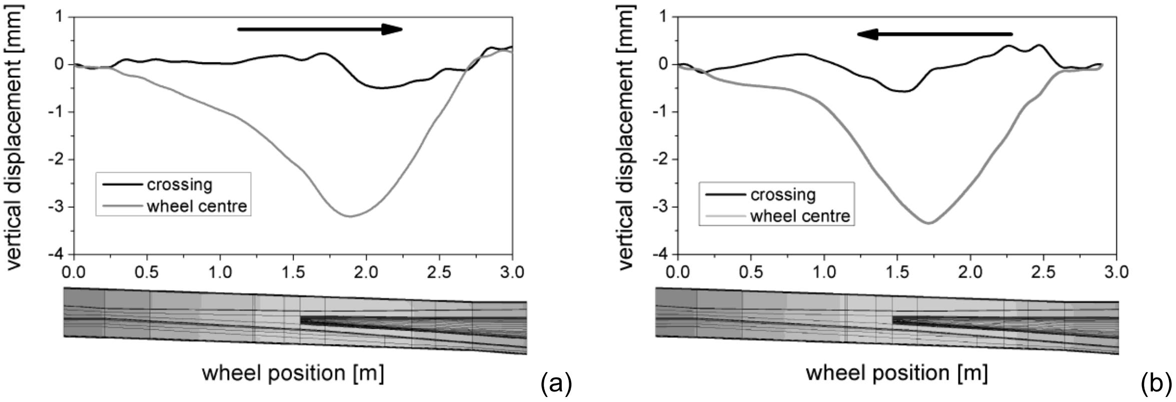

Figure 6: Vertical displacements of the wheel centre and the crossing at 160 km/h for (a) the facing and (b) the trailing move.

Figure 7 shows the angular velocity of the first wheel running over the crossing (ω) relative to the angular velocity of a free rolling second wheel on the regular rail (ω_2) for three train speeds. This relative angular velocity ω_r can be written as $\omega_r = (\omega - \omega_2)/\omega_2$.

In the facing move, the wheel approaches the crossing from the wing rail. Along this wing rail, the change in the contacting radius of the wheel (it decreases) causes the axle to increase its angular velocity. The second wheel and the inertia of the axle tend to hinder that acceleration. The inertia effect can be clearly seen in comparing the velocities: The change in the 75 km/h model is very pronounced, but with higher velocities this difference becomes smaller. The wheel runs onto the crossing nose at a wheel position of 1.7 m, where it has a bigger rolling radius. Within about 0.2 m, the angular velocity of the wheel decreases. The wheel causes similar loading of the crossing nose as an accelerating wheel on the regular track. This discrepancy in the angular velocity determines the creepage between wheel and crossing nose and thus the microslip. Then the angular velocity of the wheel returns to its initial value as the crossing nose leads into the regular rail.

In the trailing move, there is only a slight change (decrease) of the axle's angular velocity before the impact. At the impact the angular velocity of the axle is increased corresponding to a braking wheel in the regular track. The angular velocity then decreases until it finally reaches its initial value at the end of the crossing.

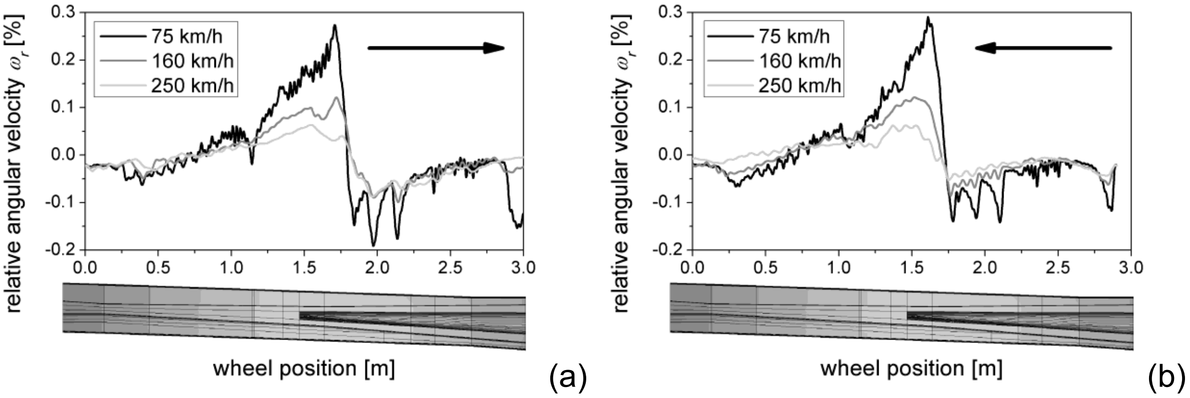

Figure 7: The angular velocity of the wheel set running over the crossing relative to the free rolling velocity of the second wheel on the regular rail for three train speeds. The difference from the angular velocity for free rolling produces a creepage on the regular rail, the crossing nose and the wing rail. The crossing is passed in (a) facing and (b) trailing move.

3.2 Comparison with Multi Body System (MBS) Calculations and field tests

As the crossover process is very complex, a direct validation of the model is a challenging task. The loading is usually based on a statistical distribution of train velocities, axle loads, bogie types and wheel profiles. In this work one single case is investigated, and for this case only the first passing of the wheel. The high computational times of such finite element models does not yet allow for in-depth parametric studies and cyclic calculations, but this will be done in the future.

Other groups that use MBS to describe the crossover process can do such parametric studies and have compared those to measurements of geometric changes in the crossing nose [33, 34]. For the dynamic process, measurements were carried out in the Härad site in Sweden, which were compared to results of MBS calculations by Kassa at al [35]. In Figure 8, those measurements and MBS results for the facing move with 60 km/h and a static load of 125 kN are compared to the corresponding results of the presented model. Note that the bedding of the FE crossing model has not been calibrated with the test data as this has been done for the MBS models. The qualitative development of the contact forces agree for the different methods. The transition of the wheel from the wing rail to the crossing nose occurs at a position of about 47.4 metres. For the three calculations the main peaks of the contact forces are reached there. In the measurements some higher peaks of the contact forces occur after the transition, which are not captured by the models.

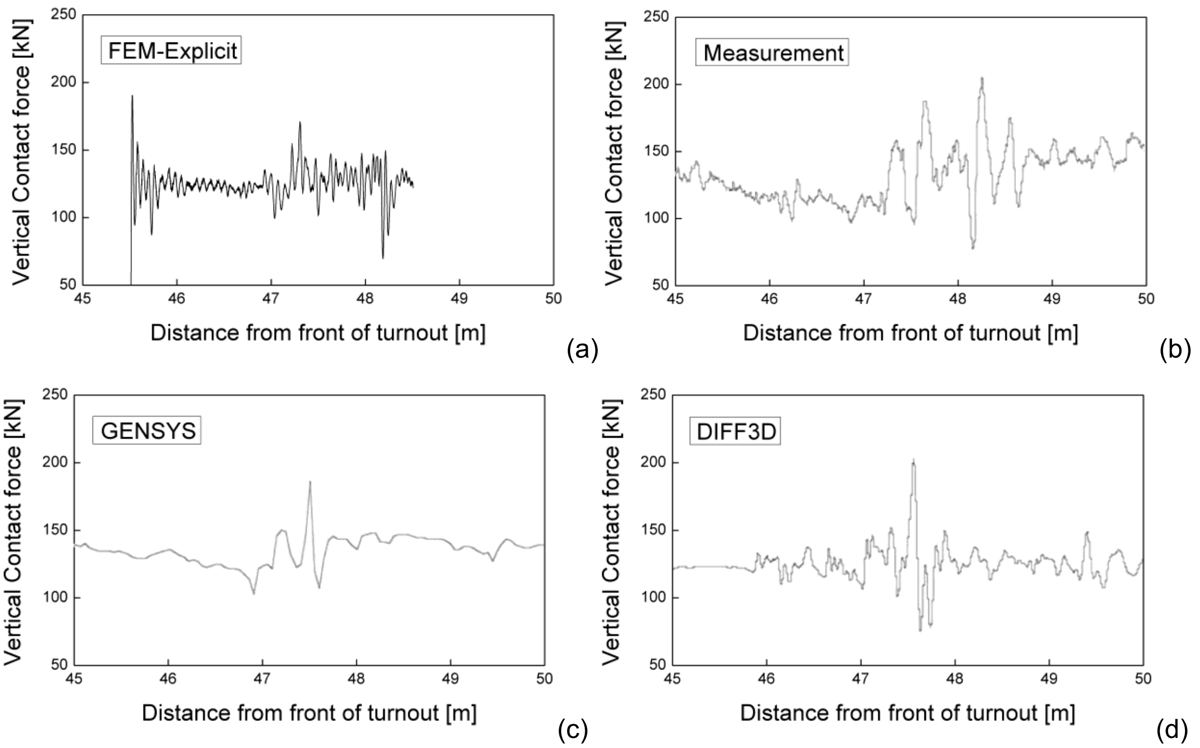

Figure 8: Comparison of the vertical contact forces of (a) the presented model with (b) measurements in the track and results of multi-body calculations with the commercial code (c) GENSYS and (d) DIFF3D. Static load of 125 kN and train velocity of 60 km/h in the facing move, see also [35]

3.3 Results for the damage related output variables

In Figure 9, variables that indicate the loading of the crossing nose and the wing rail are shown for the 160 km/h model and the facing move. A close-up of the area where the transition of the wheel takes place is displayed. In Figure 9(a) and 9(b), the frictional work and the maximum frictional power are plotted. These output variables are associated with wear and surface damage, and reach their maximum at the crossing nose. The frictional work has a maximum of 0.019 J/mm^2 and the frictional power is 156 W/mm^2.

Figure 9(c) shows the maximum of the arising microslip. It can be seen that the values are highest at a position on the crossing nose (0.7 m/s) where the wheel impacts on it, but not so pronounced as the frictional work and power, which also accounts for the high contact pressures in that region.

In Figure 9(d), the accumulated equivalent plastic strain (PEEQ) is shown as a contour plot on the crossing parts, values of which are clearly higher on the crossing nose with a maximum of 3.5 %. Comparing the vertical contact forces with this PEEQ it can be seen that not only the value of the vertical contact force but also the contact geometry determines the plastic strains. On the tip of the crossing nose, for example, the same vertical load causes much higher plastic deformations than on the broader part of the nose or the wing rail.

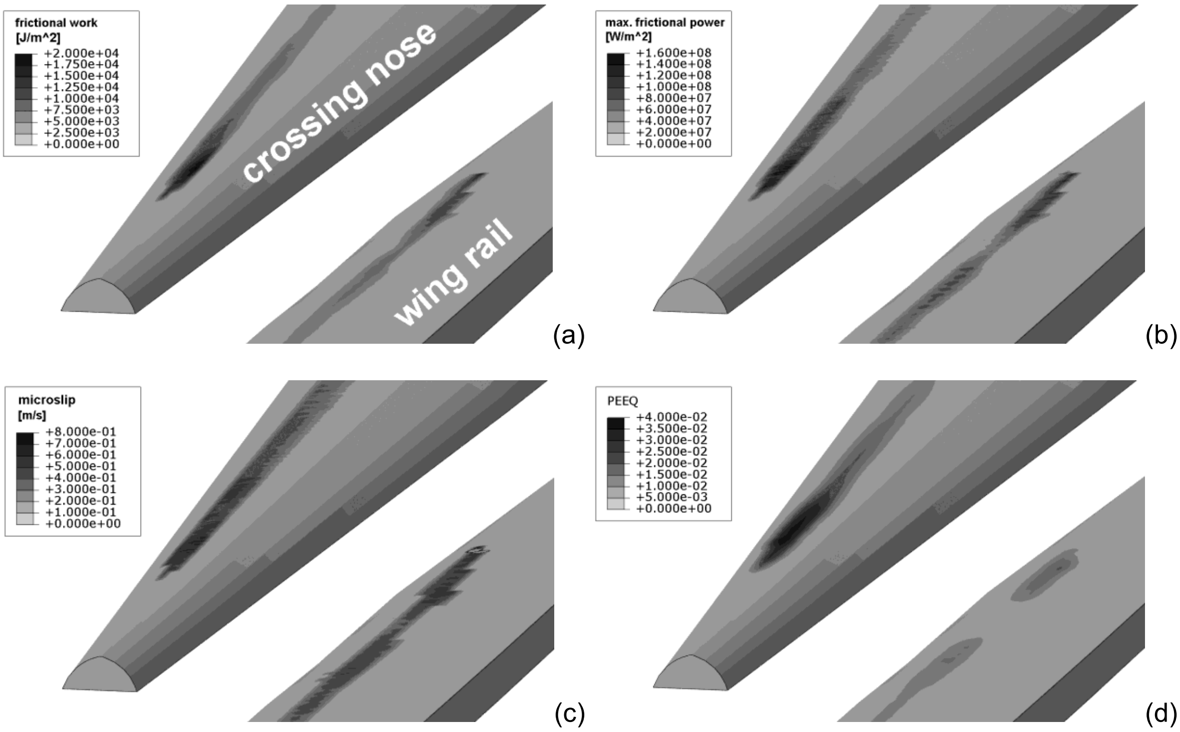

Figure 9: Results for the 160 km/h model and facing move of the wheel: Contour plots at the surface of the crossing nose of (a) frictional work, (b) max. frictional power, (c) max. microslip and (d) accumulated equivalent plastic strain (PEEQ).

The same output can be shown in diagrams containing the maximum of the output variables in the cross-sections of the crossing, which is done in Figure 10. For the frictional power and the frictional work, this would be a certain position on the surface of the crossing parts. For the PEEQ, the maximum is usually beneath the surface.

It can be seen that the maximum of the output variables is situated in the area where the wheel changes from the wing rail to the crossing nose or vice versa. The geometric situation at the tiny tip of the crossing nose and the fact that the wheel contacts the wing rail with its outer edge of the tread causes increased loading that is not indicated by the contact forces alone.

The frictional work and the frictional power show a similar behaviour for both directions. Only a slight increase at the position where the impact occurs can be determined.

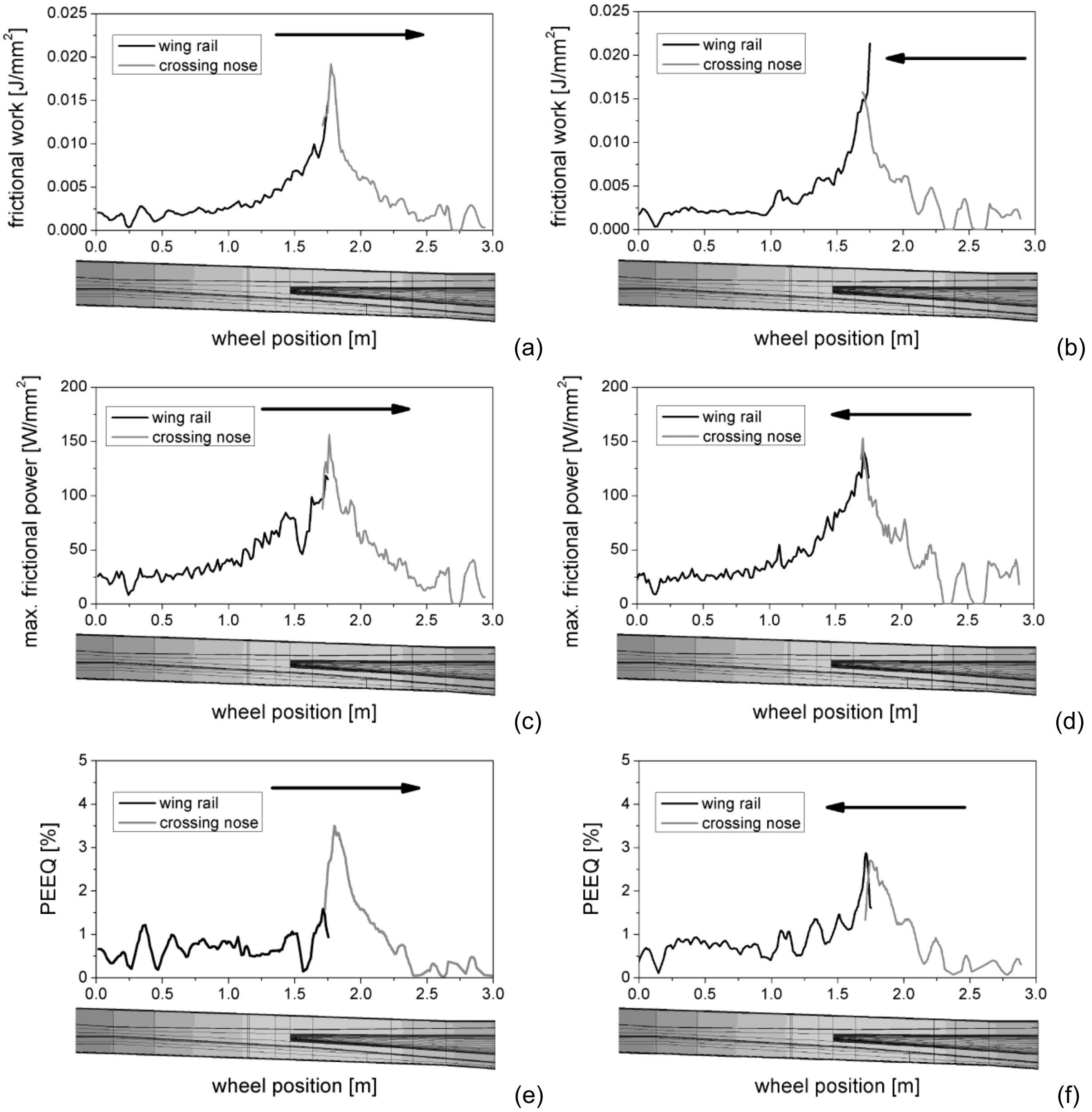

Figure 10: Diagrams of the maximum results for each wheel position of the 160 km/h model. is the curves show the frictional work in (a) the facing move and (b) the trailing move, the maximum of the frictional power for (c) the facing move and (d) the trailing move and the PEEQ in (e) the facing move and (f) the trailing move.

The plastic deformation (in this case the accumulated equivalent plastic strain - PEEQ) thus is a better indicator for the impact of the wheel. In Figure 10(e) and 10(f), this PEEQ is plotted for the facing and the trailing move. In the facing move, the maximum of the PEEQ arises on the crossing nose and is very distinctive. In the trailing move, the impact of the wheel on the wing rail increases the PEEQ on the wing rail. On the crossing nose, however, nearly the same extent of plastic deformation is produced as on the wing rail.

3.4 Comparison of the results for both directions and three velocities

In Table 2, the maxima of the different results for the three train velocities and both directions of passing are compared. The maximum of the vertical contact force due to the impact of the wheel on the crossing nose considerably increases with increasing velocity, reaching a value of 242 kN (facing move) and 271 kN (trailing move) at 250 km/h. The dynamic factor *d* representing the ratio of the impact force to the static load (79.7 kN) reaches values of 1.41 up to 3.4. The maximum of the accumulated equivalent plastic strain (PEEQ) amounts to 2.96 % (facing move) and 2.42 % (trailing move) for the model with 75 km/h. For the facing move, it increases with increasing velocity to 3.5 % (160 km/h) and 5.77 % (250 km/h). Regarding the trailing move it shows only a small increase of the maximum of the PEEQ to 2.7 % (160 km/h) and 2.95 % (250 km/h). The facing move causes the highest values of the PEEQ always in the crossing nose. For the trailing move the PEEQ at 75 km/h also leads to high values in the crossing nose. Due to the increased impact forces at the wing rail at higher velocities (160 km/h and 250 km/h) the PEEQ becomes higher in the wing rail than in the crossing nose.

Note that these plastic strains are calculated for the first passing of a wheel, when neither the material has previously hardened or softened nor the crossing nose has adapted its geometry to the loading. Therefore, the first plastic strain increment is very high compared to later progressive plastic deformation after several thousands of wheels have passed the crossing.

The microslip v_s, defined as the relative velocity between two contacting points, also increases with the train velocity. On the wing rail and the crossing nose about the same maxima of microslips arise. The creepage is higher in the 75 km/h model than for the other two train speeds, where nearly the same creepages arise. This is caused by the velocity- dependent adaption of the wheel’s angular velocity to the rolling situation on the wing rail before running onto the crossing nose. At lower speeds the angular inertia of the axle has the smallest effect and thus the adaption occurs fast causing a bigger misfit in the rotational velocity of the wheel at the change to the crossing nose. This effect can be seen in Figure 7.

Train speed	**75 km/h**		**160 km/h**		**250 km/h**	
Move	facing	trailing	facing	trailing	facing	trailing
Max. vertical contact force at impact [kN]	116	112	136	166	242	271
Dynamic factor	1.45	1.41	1.55	2.08	3.04	3.4
Max. acc. equiv. plastic strain- crossing nose [%]	2.96	2.42	3.5	2.7	5.77	2.95
Max. acc. equiv. plastic strain- wing rail [%]	1.23	1.53	1.6	2.88	1.23	3.62
Highest microslip v_s [m/s]	0.54	0.59	0.69	0.55	1.11	0.91
Highest creepage $c \approx v_s/v_t$ [%]	2.59	2.82	1.55	1.24	1.59	1.31
Maximum frictional work w_f [J/mm^2]	0.0215	0.0185	0.0192	0.0158	0.0141	0.0153
Maximum frictional power p_f [W/mm^2]	111	139	156	181	194	220

Table 2: The maxima of the relevant output variables for three train speeds and two directions of passing.

Due to this inertia effect that causes a decrease in the creepage with increasing velocity the calculated maximum frictional work for the facing and the trailing move decreases. The highest values of the frictional work are calculated in the crossing nose for the facing move with 75 km/h as 0.0215 J/mm^2. Since the maximum of the frictional power depends on the highest amount of microslip, the frictional power increases with increasing train velocity. The frictional power reaches values of up to 220 W/mm^2 on the wing rail for the trailing move with 250 km/h.

4 Conclusions

A dynamic finite element model for a wheel set passing a crossing is developed. The parameters of this model are the axle load, the passing velocity, the passing direction, the geometry and the material behaviour of wheel and crossing. There are two aspects of the process, which are of special interest: The vertical impact of the wheel and the change in the angular velocity of the wheel.

The model provides results for the contact forces between the wheel and the crossing parts. The impact of the wheel on the crossing nose can thus be studied. The crucial parameter for that impact is the angle between the velocity vectors when the wheel changes from the wing rail to the crossing nose. This is illustrated by the results for the vertical displacement of the wheel centre. Additionally, the model calculates the angular velocity of the wheel, which increases in the area of the wing rail and decreases as the wheel runs onto the crossing nose.

The impact of the wheel on the crossing nose is associated with high contact stresses and high plastic deformations. The change in the angular velocity of the wheel, on the other side, is associated with slip between the wheel and the crossing parts.

The contact pressure and the microslip are important variables for the surface damage of the crossing. High microslips in combination with high contact pressures can lead to wear and rolling contact fatigue. The frictional work and the maximum of the frictional power are measures for this damage and are thus evaluated in the presented model.

In crossings damage is observed in areas where the presented model calculates the highest frictional powers and frictional works. Empirical laws state that the frictional work is proportional to the wear depth. A detailed explanation of the interrelation between frictional work, frictional power and damage still has to be established using micro-models and experiments.

The presented model provides a practical tool for the optimization of crossings in terms of geometry, bedding and material. The mechanisms that cause the loading of the critical parts can be described, providing a better understanding of the process. New crossing concepts can be investigated before manufacturing prototypes and conducting field tests, thus reducing the development time. Serving as a tool for track engineers, the model will be able to explain the influence of velocity, bedding, axle load and wheel profiles on the crossings lifetime.

Acknowledgements

Financial support by the Austrian Federal Government (in particular from the Bundesministerium für Verkehr, Innovation und Technologie and the Bundesministerium für Wirtschaft und Arbeit) and the Styrian Provincial Government, represented by Österreichische Forschungsförderungsgesellschaft mbH and by Steirische Wirtschaftsförderungsgesellschaft mbH, within the research activities of the K2 Competence Centre on “Integrated Research in Materials, Processing and Product Engineering”, operated by the Materials Center Leoben Forschung GmbH in the framework of the Austrian COMET Competence Centre Programme, is gratefully acknowledged.

The authors specially thank Elias Kassa for providing the data for the MBS and field measurement comparison, shown in section 3.2.

References

[1] M. Wiest, W. Daves, F.D. Fischer and H. Ossberger: ZEVrail Glas. Ann., 2005, vol. 129 (11-12), pp 461-467 (in German).

[2] F.D. Fischer, H. Steiner and R. Schossmann: ETR (Eisenbahntechnische Rundschau), 1979, vol. 28 (7/8), pp 597-602 (in German).

[3] T.X. Yu, X.W. Chen and Y.Z. Chen: Computers and Structures, 2002, vol. 80, pp 1965-1973.

[4] F.D. Fischer, E.R. Oberaigner, W. Daves, M. Wiest, H. Blumauer and H. Ossberger: ZEVrail Glas. Ann., 2005, vol. 129 (8), pp 336-345.

[5] F.D. Fischer, W. Daves and H. Dirschmid: ZEVrail Glas. Ann., 2005, vol. 132, pp 187-190.

[6] M.X.D. Li, T. Ekevid and N.-E. Wiberg: An Integrated Vehicle-Track-Ground Model for Investigating the Wheel/Rail Dynamic Forces due to High Axle Loads, Proceedings of the 6th International Conference on Contact Mechanics and Wear of Rail/Wheel Systems, Gothenburg, Sweden, 2003, pp 295-300.

[7] J.C.O. Nielsen and A. Igeland: J. Sound Vibr., 1995, vol. 187 (5), pp 825-839.

[8] E. Kassa: Simulation of Dynamic Interaction between Train and Turnout, Licentiate Thesis, Chalmers University of Technology, Department of Applied Mechanics, Gothenburg, Sweden, 2004.

[9] J.C.O. Nielsen, R. Lundén, A. Johansson and T. Vernersson: Vehicle Syst. Dyn., 2003, vol. 40 (1-3), pp 3-54.

[10] H.H. Jenkins, J.E. Stephenson, G.A. Clayton, G.W. Morland and D. Lyon: Railway Eng. J., 1974, vol. 3, pp 2-16.

[11] S. Iwnicki: Fatigue Fract. Engng. Mater. Struct., 2003, vol. 26 (10), pp 887-900.

[12] C. Andersson and T. Dahlberg: Proc. Instn. Mech. Engrs., Part F. J. Rail Rapid Transit, 1998, vol. 212, pp 123-134.

[13] C. Andersson and T. Dahlberg: Vehicle Syst. Dyn. Suppl., 1999, vol. 33, pp 131-142.

[14] G. Johansson, M. Ekh and K. Runesson: Int. J. Plasticity, 2005, vol. 21, pp 955-980.

[15] Saulot and L. Baillet, Finite Element Simulation of Wheel-Rail Contact Dynamic Instabilities Under Sliding Conditions, Proceedings of World Tribology Congress III, Washington, D.C., USA, 2005, pp 249-250.

[16] K.L. Johnson: Contact Mechanics, Cambridge University Press, Cambridge, UK, 1985.

[17] J.J. Kalker: Three-dimensional Elastic Bodies in Rolling Contact, Kluwer, Dordrecht, the Netherlands, 1990.

[18] J. Ringsberg and B.L. Josefson: Proc. Instn. Mech. Engrs., Part F. J. Rail Rapid Transit, 2001, vol. 215, pp 243-159.

[19] Sladkowski and M. Sitarz: Wear, 2005, vol. 258, pp 1217-1223.

[20] T. Telliskivi and U. Olofsson: Proc. Instn. Mech. Engrs., Part F. J. Rail Rapid Transit, 2001, vol. 215, pp 65-72.

[21] W.Y. Yan, T. Antretter, F.D. Fischer and H. Blumauer: "Numerical Analysis of the Cyclic Response of a Crossing Component in a Switch", in "Proceedings of the XIX. Verformungskundliches Kolloquium", Montanuniversität Leoben, Austria, 2000, pp 78-83.

[22] Z. Wen, X. Jin and W. Zhang: Wear, 2005, vol. 258, pp 1301-1309.

[23] M. Wiest: Modelling of Wheel-Rail/Crossing Interactions, 12, Nr. 642, VDI-Verlag, Düsseldorf, 2007.

[24] M. Wiest, Kassa, E., Daves, W., Nielsen, J.C.O. and H. Ossberger: Wear, 2008, vol. 265, pp 1439-1445.

[25] M. Wiest, Daves, W., Fischer, F.D. and Ossberger, H.: Wear, 2008, vol. 256, pp 1431-1438.

[26] M. Pletz, W. Daves, F.D. Fischer and H. Ossberger, "A Dynamical Wheel Set: Crossing Model Regarding Impact, Sliding and Deformation", in "Proceeding at the 8th International Conference on Contact Mechanics and Wear of Rail/Wheel Systems", Florence, Italy, pp 801-809, 2009.

[27] M. Pletz, W. Daves and H. Ossberger, "Dynamic Finite Element Model of a Wheel Passing a Crossing Nose", in "Proceeding at the The Tenth International Conference on Computational Structures Technology", Valencia, Spain, 2010.

[28] J.F. Archard: J. of Appl. Phys., 1953, vol. 24, pp 981-988.

[29] H. Krause and G. Poll: Wear, 1986, vol. 113, pp 103-122.

[30] Abaqus, ABAQUS User's Manual, version 6.7, 2009, www.abaqus.com.

[31] F.W. Carter: Proc. R. Soc., 1926, vol. A112, pp. 151-157.

[32] J.J. Kalker: Wear, 1991, vol. 144, pp 243-261.

[33] A. Johansson, B. Palsson, M. Ekh, J.C.O. Nielsen, M.K.A. Ander, J.

Brouzoulis and E. Kassa: Wear, vol. 271, 2011, pp 472-481.

[34] D. Nicklisch, J. C. O. Nielsen, M. Ekh, A. Johansson, B. Pålsson, J. M. Reinecke and A. Zoll, “Simulation of wheel–rail contact and subsequent material degradation in switches & crossings”, in “Proceedings of the 21st International Symposium on Dynamics of Vehicles on Roads and Tracks”, Stockholm, Sweden, 2009.

[35] E Kassa and J C O Nielsen: Vehicle Syst. Dyn. Suppl., 2008, vol. 46, pp 521-534.

Paper B

A Wheel Passing a Crossing Nose- Dynamic Analysis under High Axle Loads using Finite Element Modelling

M. Pletz
W. Daves
H. Ossberger

in

Proceedings of the Institution of Mechanical Engineers, Part F: Journal of Rail and Rapid Transit, (2012)

A Wheel Passing a Crossing Nose- Dynamic Analysis under High Axle Loads using Finite Element Modelling

M. Pletz[1,2], W. Daves[1,2], H. Ossberger[3]
[1]Materials Center Leoben Forschung GmbH, Leoben, Austria
[2]Institute of Mechanics, Montanuniversität Leoben, Leoben, Austria
[3]VAE GmbH, Zeltweg, Austria

Abstract

A finite element model for the process of a wheel passing a crossing is presented. In the dynamic model, one wheel, the wing rails and the crossing nose (frog) are modelled. The bogie, the whole wheel set and the bedding of the crossing are represented as a system consisting of masses, springs, dampers and frictional elements.

With the model, the rolling/sliding behaviour between wheel and crossing can be studied. Due to the conical shape of the wheel tread and multiple contacts between wheel and the crossing parts, sliding occurs during the transition of the wheel from the wing rail to the crossing nose or vice versa. At the same time, an impact occurs that produces high contact forces.

The parameters of the model are the train speed and passing direction, the wheel and the crossing geometry, the axle load and the bedding of the crossing. In this work, the crossover process is studied for high axle loads and compared to results of simulations using normal axle load. Further parameters are three train velocities, both directions of passing and different crossing materials. The loading of the crossing nose is calculated for all cases (axle load, train speed and direction) and materials.

1 Introduction

Turnouts are an important part of the railway track system. They consist of a switch and a crossing panel. In this work the dynamic process in the area of the crossing panel is studied. There occurs a vertical impact of the wheel on the crossing nose (facing move) or on the wing rail (trailing move). In these areas of high dynamic loading, also slip between the wheel and the crossing parts occur. Hence the crossing parts feature wear and/or different kinds of damage. Crossings thus have a big influence on the maintenance costs of the tracks. For the service or the replacement of crossings in the track, there are often only small time intervals available. This is another reason for the importance of increasing and the lifetime of the crossing parts.

One approach to increase the performance of the turnout is to optimize the impacts to minimize the dynamic effects. Numerical models play an important role in this optimization. However, for a complex system as the crossing with its wing rails and the crossing nose (shown in Figure 1) it is an ambitious task to develop realistic numerical models. These simulations should regard all main influences like e.g. the dynamic impact, the slip between the wheel and the crossing parts and remain able to calculate the resulting stresses and strains in the crossing.

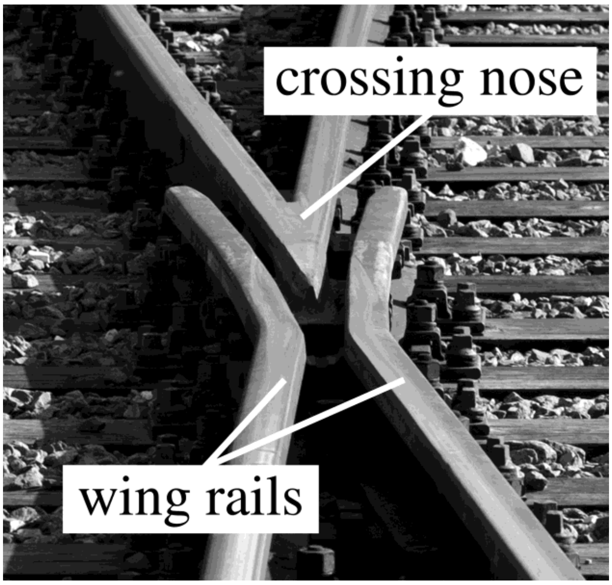

Figure 1 Picture of a crossing with its wing rails and crossing nose.

A review on dynamic calculations of train/track interaction was done by Knothe and Grassie [1]. One method that is widely used is the Multibody System (MBS) method that represents the train and the track by springs, dashpots and masses. For the contact simplified models are usually employed. Plastic material behaviour is not directly considered. Kassa [2] and Kassa and Nielsen [3, 4] developed MBS models for turnouts. A modelling approach that uses MBS and other methods to predict deformation and damage was done by Johansson et al. [5]. A comparison of this approach to measurements in the track was done in the work of Nicklisch et al. [6].

In the work of Bruni et al. [7], two approaches (MBS and simplified finite element) for the loading of crossings are investigated. Results of these models are compared to acceleration measurements in the track.

In the work of Wiest [8] and Wiest et al. [9], analytical, quasistatic and explicit methods are used to calculate the loading of crossings.

Within this paper a geometrically realistic model for the crossover process is presented. First results of that model have already been reported by the authors in [10, 11]. One objective of this work is the comparison of the dynamic effects in the vertical direction for elastic as well as two different elastic-plastic crossing materials. The case of a regular axle load of 14.2 metric tons is compared to a heavy haul case of 32.4 metric tons (36 short tons), which is a realistic case for the US freight traffic.

Heavy haul operators often use moderate velocities, so that wear and damage in the rails and turnout parts can be kept in a tolerable range. This practice is numerically investigated in this work by comparing the vertical contact force and von Mises stress in the crossing parts for different passing velocities. For different materials, it can thus be predicted whether plastic deformation will occur or not. On the one hand, plastic deformation can accumulate with many passing wheels and be considered as damage. On the other hand, the plastic deformation can cause the crossing nose to geometrically adapt and thus lower the contact pressure [12]. During the passing of a wheel over the crossing there is an area where the wheel is both in contact with the wing rail and the crossing nose. This area is of particular interest and will be called the *transition area*.

2 Dynamic Finite Element Model

In the presented model, the crossing is regarded along a length of three metres. Within this length, the transition of the wheel from the wing rail to the crossing nose (or vice versa) can be investigated. In Figure 2 the model's geometry and the generated mesh is shown.

We investigate a manganese cast crossing of the standard design 760-1:15 for UIC60 rails. The wing rail features no superelevation. The wheel is modelled using an unworn UIC-ORE 1002 profile. The whole model contains 250 000 elements and the computational time on a common up-to date computer with 4 CPUs lies between 10- and 50 hours.

Kassa et al. [3,4] presented calculations regarding the whole train with its boogies and the whole track. Presently these simulations cannot be performed in a similar way using finite element simulations. Therefore, certain assumptions have to be made in the present work to reduce the computational costs. One necessary assumption is that during the transition process the centre of the wheel is restricted to a certain lateral position determined by the second wheel, which is assumed to be running along (and touching) the check rail. This assumption seems to be reasonable for a crossover process in the diverging route.

The rotation of the wheel around the vertical axis and the longitudinal axis is disabled. The wheel is damped in the vertical direction representing the primary suspension by a damping coefficient of 53 kNs/m. The longitudinal velocity of the wheel is held constant throughout the calculation at a velocity of 64.4, 96.6 and 120.7 km/h (corresponding to40, 60 or 75 mph). In the vertical direction, a static wheel load of 79 700 N is applied to the case of a regular axle load and 174 906 N for the heavy haul case. The friction coefficient between the wheel and the rail is assumed to be 0.3.

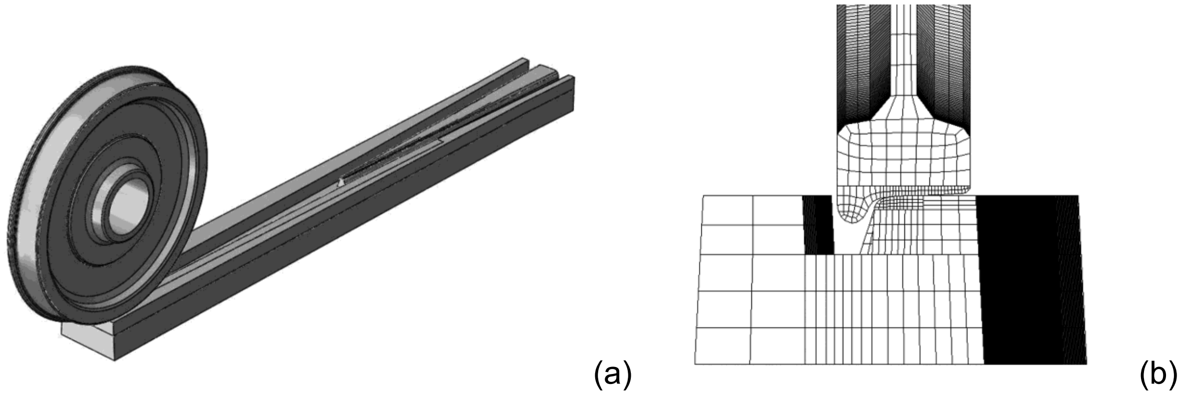
(a) (b)

Figure 2 a) Geometry and b) mesh of the finite element model

For an accurate description of the angular velocity (and thus the slip) of the wheel, resp. wheel set, the second wheel has to be regarded in the model. This is done using a special purpose element that produces a torsional moment on the axle depending on the angular velocity of the wheel set. For the assumption that the second wheel is running along the check rail, reasonable results for the angular velocity of the wheel set are obtained. Details about this special purpose element are described by the authors in [7].

The three-metre part of the crossing possesses a total mass of 680 kg. The material is modelled with either elastic or elastic-plastic material behaviour. The mass of the wheel is set to 1025 kg in the case of the regular axle load and 1500 kg in the heavy haul case, respectively. The wheel is modelled with the elastic material behaviour of steel. For the crossing materials models with different material descriptions are used: a) the same elastic behaviour as for the wheel, b) elastic-plastic material behaviour of non-pre-hardened Manganese steel (Mn13) and c) elastic-plastic material behaviour of a maraging steel (Marage). The elastic constants and the yield stresses of the used materials are given in Table 1. Since it is intended to compare very different but commonly used crossing materials, Manganese steel is chosen that shows with 200 MPa a very low yield stress whereas the maraging steel exhibits with 1700 MPa a very high yield stress. The plastic curves shown in Figure 3 illustrate the different hardening behaviour of the two steels. A kinematic hardening model is used to describe the material behaviour.

In the work presented in [7] the model uses rigid bedding of the crossing. So both the support by the pad/sleeper/ground as well as the bending of the crossing between the sleepers is neglected. For a more realistic bedding an activated mass, a spring constant and a damping constant have to be regarded. For the sake of simplicity the complex bedding system with a changing stiffness along the length of the crossing is reduced to a single element of a spring and a damper in a parallel setup. The whole bottom of the crossing is connected rigidly and supported by this spring-damper element. The spring constant of the bedding is set to 90 kN/mm, the damping constant to 250 Ns/mm and the spring supported mass amounts to 680 kg.

Table 1 The material parameters used in the model

Property	**Wheel (elastic)**	**Manganese steel (Mn13)**	**Maraging steel (Marage)**
Young’s modulus [GPa]	210	201	189
Poisson ratio	0.3	0.3	0.3
Density [kg/m^3]	7800	7800	7800
Yield stress [MPa]	-	200	1700

The model can describe the full cyclic elastic-plastic material behaviour of the crossing. The plastic deformation strongly affects the contact stresses. In this work, different load cases (axle loads, velocities and directions of passing) with elastic crossing material are compared in terms of their arising stresses that can lead to plastic deformation. From the von Mises stresses of this elastic calculation, it can be predicted whether certain materials would plastically deform under this load.

In a separate model with elastic-plastic representation of the crossing material, the plastic strains are calculated for one load cycle and two materials Mn13 and Marage.

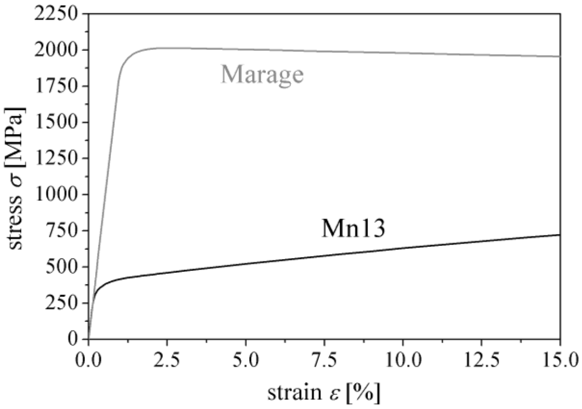

Figure 3 Plastic curves for the two used materials Manganese steel (Mn13) and maraging steel (Marage).

3 Results and Discussion

3.1 Dynamic results for one case of loading (forces, velocities, displacements) with elastic material

In Figure 4a, the vertical contact forces between the wheel and the wing rail and the crossing nose are plotted. The sketch of a crossing below the diagram, having the same length scale as the abscissa, allows to identify the wheel position on the crossing.

At the start of the calculation, the wheel is placed on the wing rail at a wheel position of 0 m. Then the wheel moves from left to right corresponding to a facing move. In a dynamic calculation the placing of the wheel leads to oscillations especially of the vertical contact force, see Figure 4a. These oscillations are visible from the start of the calculations at wheel position 0 metres until a longitudinal wheel position of about 0.2 metres is reached. After 0.2 metres of rolling these start oscillations are significantly damped. At about 0.2 metres the wing rail starts to deviate from the straight direction and causes the conical-shaped wheel to move downward as it can be seen in the diagram of the vertical displacements in Figure 4b. This change in the translational movement of the wheel causes oscillations of the contact force. The amplitude of these oscillations decreases during the following metre since the plastic deformation in the crossing material and a vertical damping element connected to the wheel centre cause energy dissipation.

At a wheel position of about 1.7 m, the wheel impacts on the crossing nose. The direction of the wheel's movement changes as can be seen in Figure 4b. The contact force at the crossing nose reaches a value significantly higher than the static load. During this transition there is an area in which the wheel is both in contact with the wing rail and the crossing nose. After the impact, contact forces nearly as high as during the impact are calculated, but due to changes in the size of the contact patch the local stresses become significantly smaller.

As the contact point on the wheel changes during its run on the wing rail, then from the wing rail to the crossing nose and, to a lesser extent, during its run on the crossing nose, the angular velocity of the axle also changes. In the model, the wheel has a constant longitudinal velocity, which means that a decrease in the rolling radius of the wheel causes an increase of the angular velocity of the axle. This can be seen in Figure 4c at a wheel position of up to 1.7 metres. As the wheel impacts on the crossing nose, the rolling radius is suddenly changing to a larger value which causes the angular velocity of the axle to decrease. This change of the angular velocity of the axle is associated with a slip of the wheel on the crossing parts. Important parameters for the calculation of this velocity change are the inertia of the axle and of the two wheels, the friction coefficient and the train velocity.

The vertical contact force between the wheel and the crossing parts and the size of the contact patch determines the stresses and strains in the contact zone. High vertical contact forces are responsible for high stresses and high plastic deformations only in the case of a small contact patch. The stresses in the crossing depend on the contact radii of the crossing where the wheel contacts. If the wheel contacts near the tip of the crossing nose, a very small contact radius (therefore small contact patch) produces much higher contact stresses as contacts in other regions. To make this visible the maximum arising von Mises stresses in all cross sections of the crossing parts are plotted along the running direction, see Figure 4d. It can be seen that for the low axle load and 96.6 km/h, the von Mises stresses reach values of up to

1700 MPa in the region where the wheel impacts onto the crossing nose. In further Figures these Mises stresses will predict whether, and on which location of the crossing parts, plastic deformation will be produced.

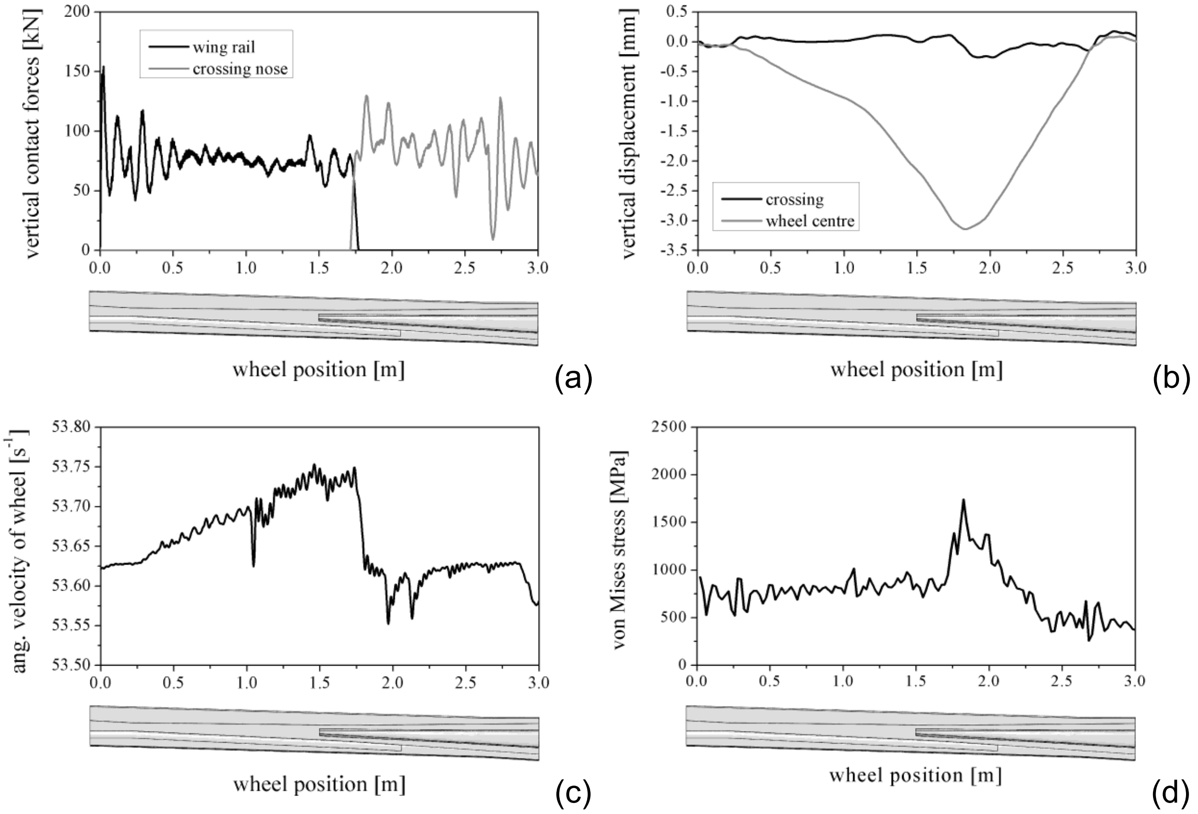

Figure 4 Results for elastic material behaviour, the low axle load, facing move and a train speed of 96.6 km/h. The curves show a) the vertical contact forces between the wheel and the crossing parts, b) the vertical displacements of the wheel and the crossing, c) the angular velocity of the axle and d) the highest von Mises stress in each cross section of the crossing.

3.2 Dynamic Results for Different Running Velocities and Axle Loads, elastic case

Both the axle load and the running velocity have a crucial influence on the dynamic process. In the following the evolution of the vertical contact forces between wheel and crossing parts are compared for two different axle loads and three train velocities that are relevant for heavy haul cases. Results for both directions of passing are presented.

In Figure 5a, b the vertical contact forces are shown for a train speed of 96.6 km/h. The dark lines give the values for the low axle load (14.2 tons). The contact forces of the heavy haul case with an axle load of 32.4 tons are plotted light gray. The dashed horizontal lines represent the corresponding static loads of these two cases.

The impact of the wheel on the crossing nose (facing move) can be seen in figure 5a, where the contact force has a peak at a wheel position of about 1.6 metres. The whole development of the contact forces looks similar for the two axle loads; however, their mean values are different. Due to the higher static load, the heavy haul case shows a longer *transition area*. In the trailing move, the wheel impacts on the wing rail and causes a peak in the contact forces on the wing rail, see figure 5b.

In the following, all maximum values of the contact force evolution during the simulated 12 cases are compared. The results are shown for two axial load cases (14.2 and 32.4 metric tons) and three assumed/calculated velocities of 64.4, 96.6 and 120.7 km/h.

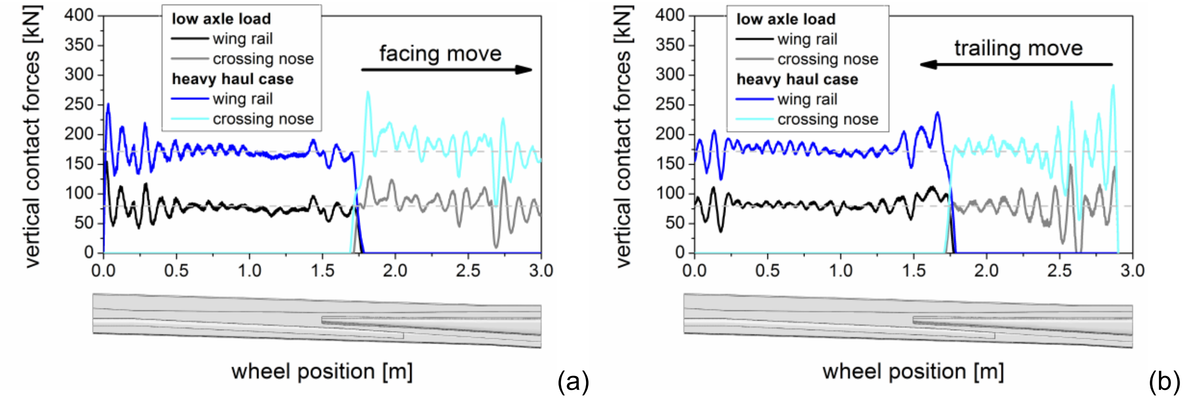

Figure 5 Contact forces between the wheel and the crossing parts for elastic crossing material at a train speed of 96.6 km/h. The results are shown for two axle loads. Transition in a) facing move and b) trailing move.

In Figure 6a the maximum vertical contact forces at the impact are shown. For comparison of the different axle loads, also the dynamic factor of the impact is presented in figure 6b. The dynamic factor is defined as the maximum arising contact force divided by the static load.

Initially, as one would expect intuitively, the vertical contact forces increase with increasing train speed as can be seen in Figure 6a,b. For the case of the low axle load and the facing move, however, there is a slight decrease in the contact forces towards higher velocities. This illustrates the complexity of the process, in which the wheel due to its vertical oscillations might approach the crossing nose in a way that produces less contact forces at a higher velocity. In all cases the dynamic factor reaches values between 1.2 and 1.7.

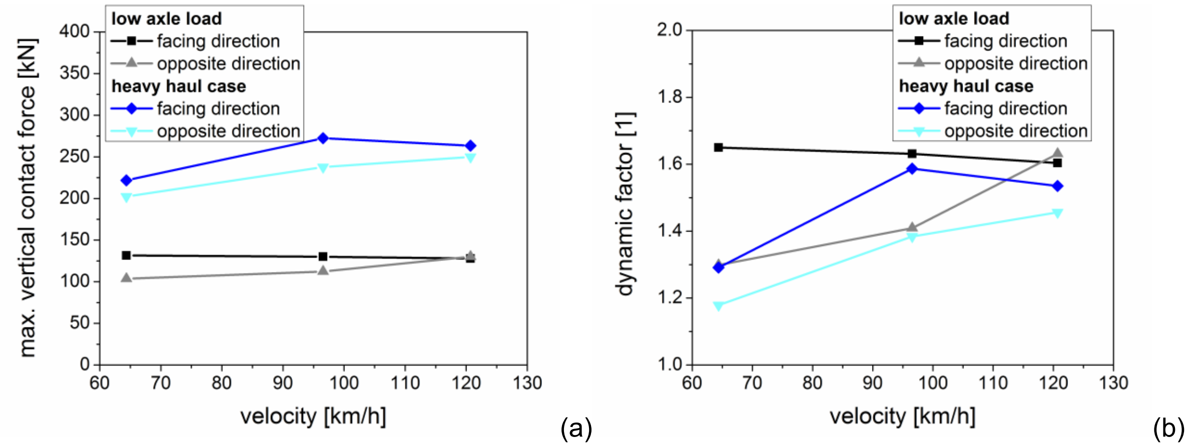

(a) (b)

Figure 6 Comparison between the three velocities, two passing directions and the two axle loads. The curves show a) peaks of the contact forces at the impact and b) dynamic factors of this impact for elastic crossing material.

3.3 Stress Results for Different Running Velocities and Axle Loads

The development of the vertical contact forces characterizes the dynamic process. The highest values of stress or strain in the crossing parts are caused by high contact forces in a combination with narrow contact patches (e.g. at the tip of the crossing nose).

For the evaluation of the material response, von Mises stresses are a better indicator than the vertical contact forces. In figure 7, the development of the von Mises stress along the crossing parts is shown for 96.6 km/h using an elastic crossing material.

The development of the von Mises stress during the facing move (Figure 7a) shows a clear difference in its level for the two axle loads. For the low axle load, a maximum von Mises stress of 1740 MPa is reached, whereas for the high axle load the maximum amounts to 2320 MPa. Note that up to this point the material behaviour is assumed purely elastic, thus overestimating the arising stresses. On the diverging wing rail (wheel position of 0.2 to 1.7), a von Mises stress of 700 MPa (low axle load) or 1200 MPa (high axle load) arise. After the impact of the wheel on the crossing nose, the contact radius of the crossing increases and thus the stresses decrease. Results of the von Mises stresses for the trailing move are shown in Figure 7b. The results are similar to the ones for the facing move, with the difference that lower maxima of the von Mises stresses are reached because the wheel does not impact onto the narrow part of the crossing nose with its small contact radius. The von Mises stresses amount to 1370 MPa for the low and 2080 MPa for the high axle load.

The maximum of the von Mises stress is located always at the tip of the crossing nose, even if the wheel passes the crossing in the trailing move and impacts on the wing rail. This is due to the small radius of the tip of the crossing nose.

If the von Mises stress exceeds the initial yield stress of the crossing material, plastic strain occurs.

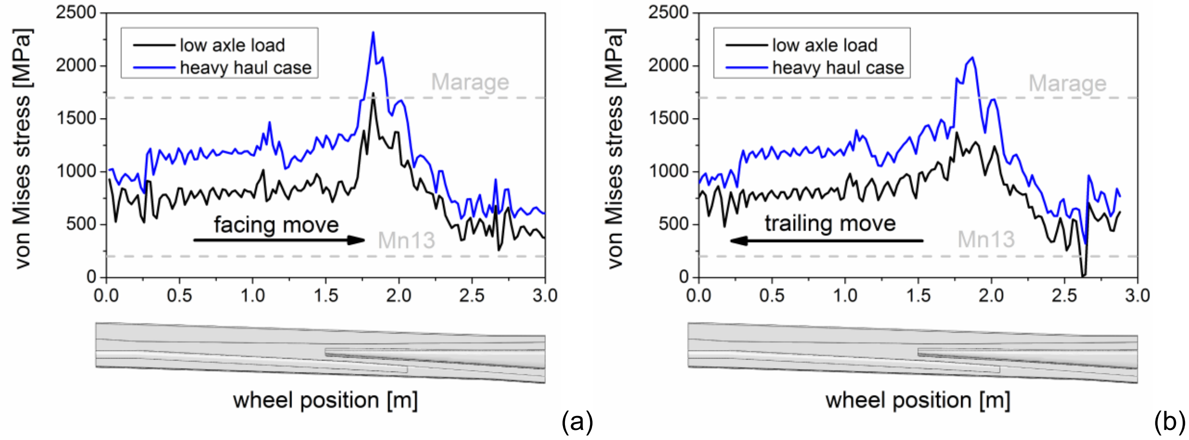

Figure 7 Highest von Mises stress at a train speed of 96.6 km/h. Results for both axle loads. Transition in a) facing move and b) trailing move. The yield stresses of crossing materials are indicated by dashed lines.

A direct comparison of the highest von Mises stresses for the different moves, train speeds and axle loads is shown in Figure 8. In addition, the yield stresses for the Manganese steel (Mn13) and the maraging steel (Marage) are indicated by horizontal dashed lines.

There is a clear tendency to higher von Mises stresses with increasing train speed which is more pronounced for the facing move. The maximum von Mises stresses are always detected in the crossing nose. They are higher for the facing move in which the wheel impacts on the crossing nose. For the low axle load, the maximum von Mises stress amounts to about 1400 MPa and increases only slightly with the train speed for the case of the trailing move. For the low axle load and facing move, the von Mises stress reaches up to 1590 MPa at 64.4 km/h and increases to 1830 MPa at 120.7 km/h. The levels of the von Mises stresses are generally higher for the high axle load. For the trailing move they are about 2100 MPa and in the facing move they increase from 2110 MPa at 64.4 km/h to 2360 MPa at 120.7 km/h.

Again these values are overestimating the arising stresses in elastic-plastic crossings.

For the heavy haul case with an axle load of 32.4 tons the yield stresses of both Mn13 and Marage are exceeded for the whole range of investigated train speeds. In the trailing move the yield stress of Marage is never exceeded for the case of the low axle load of 14.2 tons. In the facing move the low axle load only causes plastic strains in Marage at higher velocities.

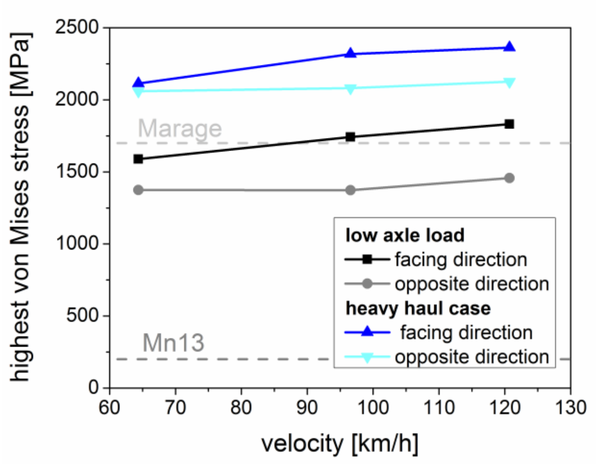

Figure 8 The maximum von Mises stress for the two directions of passing and the three train speeds. The yield stresses of Mn13 and Marage are shown as dashed lines.

3.4 Investigations using plastic material behaviour

The loading of the crossing parts is investigated using plastic material behaviour. This is of interest, since plastic deformation can cause adaption of the crossing nose or wing rail with the effect that vertical contact forces are reduced. The plastic deformations after one crossover are shown for the two materials Mn13 and Marage.

A measure for the plastic deformation is the accumulated equivalent plastic strain (PEEQ). In Figure 9a and 9b, this PEEQ is shown as a contour plot on the surface of the crossing parts. The maximum of PEEQ in the wing rail or the crossing nose is evaluated at each cross section along the longitudinal axis. The PEEQ values are plotted in Figure 9c for the low axle load and in Figure 9d for the high axle load. For the Manganese steel (Mn13), the highest plastic strains are calculated on the crossing nose with an accumulated equivalent plastic strain of 3.2 % (low axle load) and 5.8 % (high axle load). The highest PEEQ in the wing rail amounts to 1.3 % (low axle load) and 2.9 % (high axle load). For Marage, there is no plastic deformation calculated for the case of the low axle load and 96.6 km/h. For the case of the high axle load, there is some small, very localised plastified region in the crossing nose. The PEEQ values reach a maximum of 0.4 %, as can be seen in Figure 9d.

These plastic strains cause a geometrical adaption of the crossing nose and the wing rail. The used manganese steel for crossings behaves very soft during the first loading, but hardens very quickly during the following cycles. Depending on the further loading, very soon elastic shakedown can be reached due to the hardening of the material and the changes of the crossing's geometry.

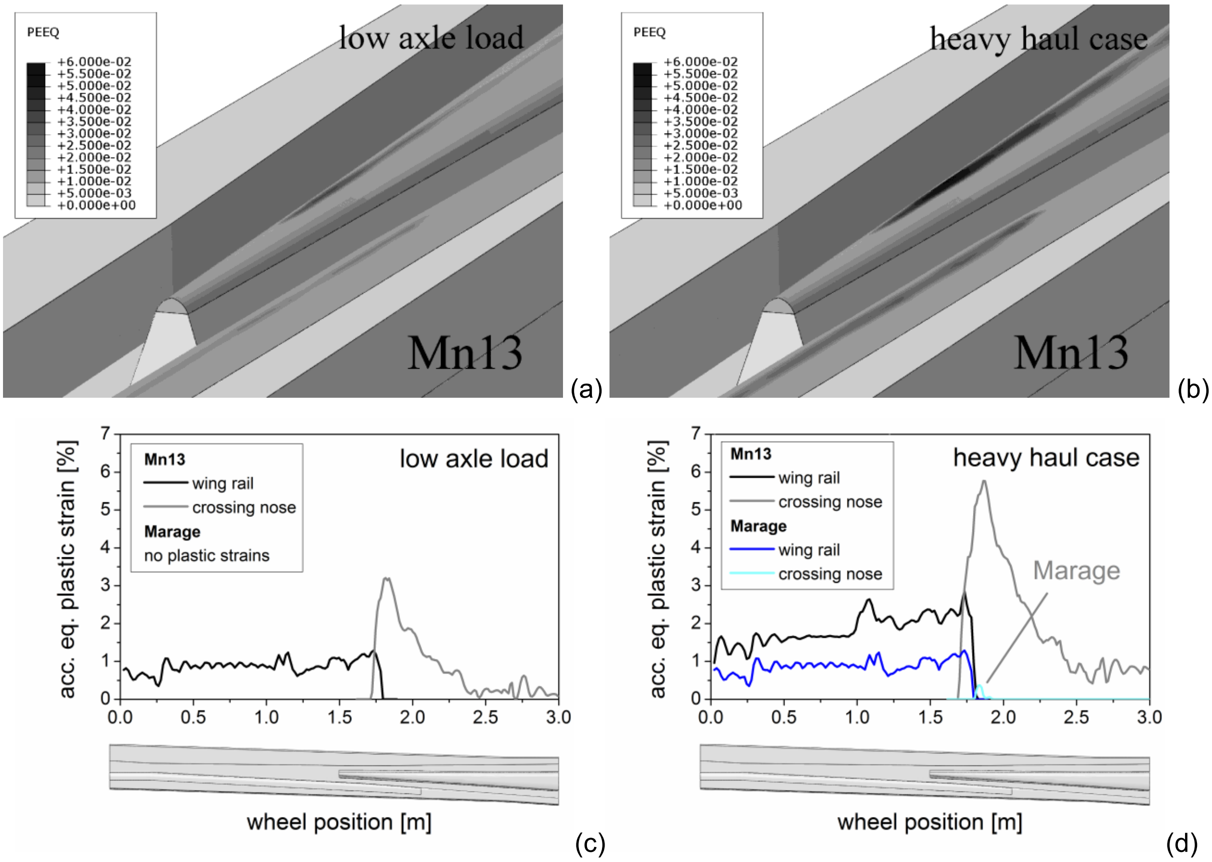

Figure 9 The accumulated equivalent plastic strain (PEEQ) after one crossover of the wheel in the facing move at 96.6 km/h. Contour plots of the PEEQ for the Mn13 crossing are shown for a) the low axle load and b) the high axle load. The maximum of PEEQ in the crossing parts along the longitudinal direction (wheel position) are shown for both materials and for c) the low axle load and d) the high axle load. For the low axle load, no plastic strain appears in the Marage crossing.

This will be investigated in a future work, where the adaption of the crossing and its effect on the loading will be studied. First results show that at the tip of the crossing nose contact pressures can significantly be reduced by this geometric adaption. If these results can be verified, this means that the plastic deformation plays an important role in the development of wear and damage in the track. The calculated plastic strains shown in Figure 9 indicate a positive effect on the performance of the crossing (due to the geometric adaption).

3 Conclusions

A dynamic finite element model is developed for the crossing part of a turnout. Using this model, the heavy haul case is investigated and compared to a regular axle load.

The model calculates the impact of the wheel on the crossing nose (facing move) or the wing rail (trailing move), leading to dynamic contact forces which cause high stresses and, depending on the material, plastic deformation. The results show that also in cases with moderate dynamic contact forces high stresses are reached in the crossing nose. During the trailing move, the maximum stresses still occur in the crossing nose despite the fact that the impact occurs on the wing rail.

It is shown that the vertical contact forces during the impact of the wheel on the crossing nose generally increase with higher running velocities of the train. For the heavy haul case this effect is more distinctive than for the low axle load. The forces, however, increase by less than 20 % in the investigated velocity range.

By evaluating the von Mises stress in the crossing parts of an elastic calculation, a prediction whether the crossing will plastically deform can be made. It is shown that for the very soft Manganese steel the crossing plastically deforms in all investigated cases of velocities and axle loads. For hard maraging steel it is shown that for the high axle load there is some plastic deformation and for the low axle load very little (only in the facing move and at 120.7 km/h) or none. Hard materials such as maraging steel crossings can show some advantages at higher loads when some kind of plastic deformation can take place. This plastic adaption of the crossing can reduce the contact stresses and thus the driving force for wear and RCF. The plastic adaption of maraging steel is much less pronounced in applications with low axle load.

Acknowledgements

Financial support by the Austrian Federal Government (in particular from the Bundesministerium für Verkehr, Innovation und Technologie and the Bundesministerium für Wirtschaft und Arbeit) and the Styrian Provincial Government, represented by Österreichische Forschungsförderungsgesellschaft mbH and by Steirische Wirtschaftsförderungsgesellschaft mbH, within the research activities of the K2 Competence Centre on “Integrated Research in Materials, Processing and Product Engineering”, operated by the Materials Center Leoben Forschung GmbH in the framework of the Austrian COMET Competence Centre Programme, is gratefully acknowledged.

References

[1] Knothe, K.L. and Grassie, S.L. Modelling of Railway Track and Vehicle/Track Interaction at High Frequencies. Vehicle System Dynamics, 1993, 22(3-4), 209-262.

[2] Kassa, E. Dynamic train-turnout interaction: mathematical modelling, numerical simulation and field testing. PhD Thesis 2007, Chalmers University of Technology, Gothenburg, Sweden.

[3] Kassa, E. and Nielsen, J.C.O. Stochastic analysis of dynamic interaction between train and railway turnout. Vehicle System Dynamics, 2008, 46(5), 429-449.

[4] Kassa, E. and Nielsen, J.C.O. Dynamic train-turnout interaction in an extended frequency range using a detailed model of track dynamics. Journal of Sound and Vibration, 2009, 320(4-5), 893-914.

[5] Johansson, A., Paulsson, B., Ekh, M., Nielsen, J.C.O., Ander, M.K.A., Brouzoulis, J. and Kassa, E. Simulation of wheel/rail contact and damage in switches & crossings. Wear, 2010, 271(1-2), 472-481.

[6] Nicklisch, D., Kassa, E., Nielsen, J., Ekh, M. and Iwnicki, S. Geometry and stiffness optimization for switches and crossings, and simulation of material degradation. Proc. IMechE, Part F: Journal of Rail and Rapid Transit, 2010, 224(4), 279-292.

[7] Bruni, S., Anastasopoulos, I., Alfi, S., Van Leuven, A. and Gazetas, G. Effects of train impacts on urban turnouts: Modelling and validation through measurements. Journal of Sound and Vibration, 2009, 324(3-5), 666-689.

[8] Wiest, M. Modeling of wheel-rail/crossing interactions. PhD Thesis 2007, University of Leoben, Austria.

[9] Wiest, M., Kassa, E., Daves, W., Nielsen, J.C.O. and Ossberger, H. Assessment of methods for calculating contact pressure in wheel-rail/switch contact. Wear, 2008, 265(9-10), 1439-1445.

[10] Pletz, M., Daves, W. and Ossberger, H. A Dynamical Wheel Set: Crossing Model Regarding Impact, Sliding and Deformation. 8th International Conference on Contact Mechanics and Wear of Rail/Wheel Systems, Florence, Italy, 2009, pp. 801-809.

[11] Pletz, M., Daves, W. and Ossberger, H. Dynamic Finite Element Model of a Wheel Passing a Crossing Nose. Tenth International Conference on Computational Structures Technology, Valencia, Spain, 2010, on-line.

[12] Wiest, M., Daves, W., Fischer, F.D. and Ossberger, H. Deformation and damage of a crossing nose due to wheel passages. Wear, 2008, 265(9-10), 1431-1438.

Paper C

The Plastic Adaption of Railway Crossings due to Dynamic Contact Loading – an Explicit Finite Element Study

M. Pletz
W. Daves
H. Ossberger

To be submitted

The Plastic Adaption of Railway Crossings due to Dynamic Contact Loading – an Explicit Finite Element Study

M. Pletz[1,2], W. Daves[1,2], S. Eck[2], H. Ossberger[3]
[1]Materials Center Leoben Forschung GmbH, Leoben, Austria
[2]Institute of Mechanics, Montanuniversität Leoben, Leoben, Austria
[3]VAE GmbH, Zeltweg, Austria

Abstract

A model for the description of the plastic adaption of the crossing nose of a turnout and its effect on the contact forces and contact stresses is presented. A wheel initially running on the wing rail and impacting on the crossing nose has been modelled. In one case, the impact position of the wheel on the crossing nose was varied to account for changing loading situations in the track. A comparison with a non-realistic situation of a wheel impacting always at the same position of the nose was performed to identify the influence of the cyclic material response.

The main results of the model are the contact forces between the wheel and the crossing nose, the plastic strains, the change of the crossing profile, and the contact pressure. The evolution of these values has been described for the first 20 cycles. It has been found that a significant decrease of the contact pressure is caused by plastic adaption of the crossing material.

Three different cyclic material descriptions (a Hadfield type austenitic steel, a grain refined construction steel and a tempered hot working tool steel) have been used in the model. The parameters of the corresponding cyclic elastic-plastic material models have been derived from monotonic tensile tests as well as low cycle fatigue tests.

1 Introduction

Turnouts are an important part of the railway track structure and consist of switch and crossing panels. A typical crossing is shown in Figure 1, consisting of two wing rails and the crossing nose. At the crossing panel, there is a discontinuity in the track. This results in a vertical impact of the wheel on the crossing nose or the wing rail, depending on the direction of passing. Due to the conicity of the wheel tread, sliding between the wheel and the crossing parts is inevitable in the region of the impact. The impact and the slip play an important role in the formation of damage such as wear, rolling contact fatigue (RCF) or severe plastic deformation and thus determine the lifetime of crossings.

Kassa et al. calculated this impact and the resulting loading of the crossing parts by using *multi body systems (MBS)* methods [1, 2]. Wiest et al. studied the impact on the crossing nose using, amongst others, explicit finite element (FEM) models [3]. This work has been continued by the authors, resulting in a crossing model with realistic geometry [4].

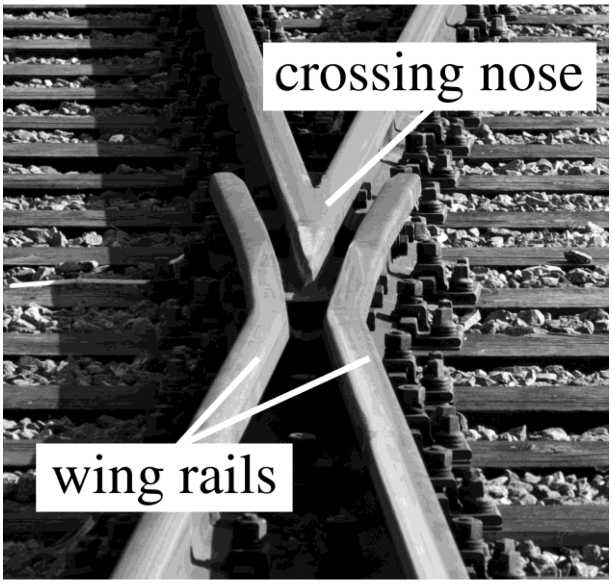

Figure 1: Crossing nose and the wing rails of a turnout.

Due to the specific loading conditions, common rail materials are usually not used as crossing parts. In fact, special steel grades are used to withstand the high dynamic loads and the sliding of the wheel. In Austria, Canada and Australia, austenitic Manganese steel (“Hadfield steel” with ~ 13wt.% Mn) is commonly used for crossings [5]. It has a very low yield stress, but a good hardening behaviour that plays an important role in its suitability for crossings. To increase the hardness on the surface of those crossings, they are often explosion hardened. Another class of steels used as crossing material are tempered high alloyed steels with a very high yield stress such as the maraging steel that is referred to in the ASTM norm as “Marage 300”. A material of an average yield stress is the grain refined construction steel sold by

SSAB under the brand name “Hardox 400”, which is used for tramway crossings and all kinds of applications where wear-resistance is of importance [6].

Depending on the mechanical behaviour of the crossing material, it often plastically deforms in the region where the wheel impacts on it. With this deformation the crossing nose tends to adapt to the geometry of the wheel. For high cycle numbers wear can have a similar effect due to material loss and resulting geometrical adaption. In rails adaption is probably not an ideal behaviour since conformal contact causes very high slip and results in wear or RCF. In crossing noses, however, the high contact pressure of the impact can be strongly reduced by this adaption, thus lowering wear and RCF.

The adaption of the crossing nose to the loading was investigated first by Wiest et al. with a FE model using simplified geometry and loading conditions. A clear decrease in the contact pressure and slight decrease of the dynamic load with proceeding plastic adaption has been found and published in [7]. Johansson et al. [8] have developed a model that can predict profile changes due to plastic deformation and wear. With this model a comparison with observed profile changes in the track has been conducted by Nicklish et al. [9]. It is based on a global MBS model, combined with a three-dimensional micro-model for the plastic contact pressure distributions, a two-dimensional model for calculating the plastic profile change and the FASTSIM [10] algorithm to predict wear. Up to 200 000 cycles were calculated, and a good agreement between profile measurements and simulations was reached. This methodology, however, needs some calibration and the use of several interfaces between different methods (MBS, FEM and FASTSIM).

In this work a dynamic finite element model is used to describe the plastic adaption of the crossing in the first 20 cycles. The contact situation and the elastic-plastic deformation of wheel and crossing are calculated in a single model. The model allows to study the effect of the plastic adaption on the dynamic contact forces and the contact stresses. As the material of the crossing plays an important role in this adaption process, the three materials Hadfield steel (in the following referred to as *Mn13*), Hardox 400 (*Hardox*) and Marage 300 (*Marage*) are used in the calculations. Elastic-plastic material models for these materials have been derived from mechanical tests. The FE model uses two types of loading: The wheel is impacting always at (a) the same position or (b) varying position on the crossing. The effect of these types of loading on the crossings adaption is described.

2 Methods

2.2 Mechanical tests

For the determination of the material parameters of the investigated crossing materials, monotonic tensile tests and low cycle fatigue (LCF) tests were conducted. The cylindrical specimens had an hourglass shape with a gauge length of 10 mm and a 10 mm diameter within this gauge length. The surface of the specimens was polished. In the monotonic tensile tests, the strain rate was 0.01 s^{-1}; strain rate dependency was not investigated. Strain-controlled LCF tests have been performed with two total strain amplitudes per material, as given in Table 1. The strain was applied with a saw-tooth wave shape with zero mean strain and a strain ratio R of -1. The first half cycle of loading was in compression and all experiments were conducted at room temperature.

Table 1: Strain amplitudes used in the LCF tests.

	Strain amplitudes ε_a of the LCF test	
Marage	1.1 %	1.5 %
Hardox	0.9 %	1.3 %
Mn13	0.9 %	1.1 %

2.2 Modelling

2.2.1 The crossing model

In previous work [4, 11, 12] a model for the crossing has been developed with the finite element code ABAQUS/Explicit [13]. In this model, a three metre part of the crossing is modelled, in which the wheel changes from the wing rail to the crossing nose. The mesh of the model can be seen in Figure 2. For the first passing wheel the influence of the train speed, the axle load, the wheel profile, the direction of passing and the crossing profile on the process can be investigated. The calculated results include the maximum vertical contact forces, the wheel movement, the longitudinal position of impact on the crossing nose, the contact pressure, the slip and the plastic strains. The following assumptions concerning the boundary conditions have been made: The longitudinal velocity of the wheel is held constant, there is no steering of the bogie and the wheel has a constant lateral position. Details about the model assumptions and results are given in [4].

With this *crossing model* that contains about 250 000 elements causing calculation times of 8h on an up-to-date four-core computer cyclic studies would be very time-consuming. The crossing model has elements with an edge-length of 3 mm in the contacting areas, which is sufficient for a good description of the dynamics and a rough but usually sufficiently accurate description of contact pressure, slip and plastic deformation. However, for a more detailed study of the adaption of the crossing nose (in terms of stresses and strains) the calculation times have to be reduced and the elements in the crossing nose have to be refined.

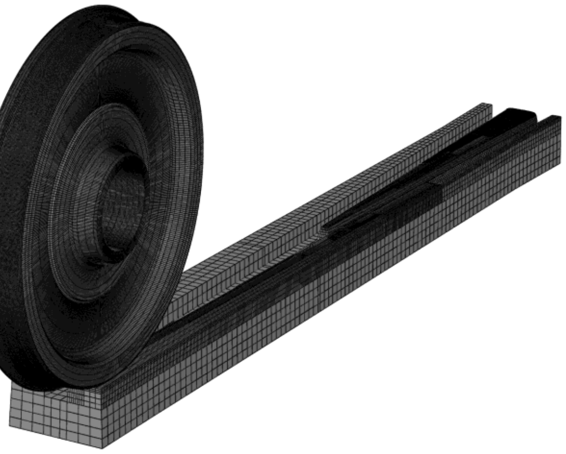

Figure 2: The crossing model with the wheel, two wing rails and the crossing nose. A total length of 3 metres is modelled.

2.2.2 The impact model

In the new *impact model*, only the 0.5 metre part of the crossing nose where the wheel impacts, has been modelled. The case of the facing move (wheel initially running on the wing rail and impacting onto the crossing nose) is investigated. The investigations consider a new wheel profile, a train speed of 160 km/h and an axle load of 14.2 tons. In Figure 3, the results of the *crossing model* are shown for this case. The corresponding region of the impact model (1.7 to 2.2 metres) is indicated by two lines. Within this distance, it can be seen that the wheel changes its vertical movement and the angular velocity of the wheel decreases. The results (e.g. the calculated accumulated plastic strains shown in Figure 3c) show that the impact of the wheel on the crossing nose is associated with high plastic deformations. The initial vertical wheel and crossing position and the wheel velocity, see also Figure 3, are subsequently used as initial conditions in the *impact model*.

Concerning the crossing geometry, a standard crossing of the type 760-1:15 (UIC 60 rails) is used. The unworn profile of an UIC-ORE 1002-type wheel has been used as wheel geometry. The mass of the wheel was 1025 kg and the moment of inertia of the whole axle is 135.5 kgm^2. The contact between the wheel and the crossing nose is modelled with a Coulomb friction coefficient of 0.3.

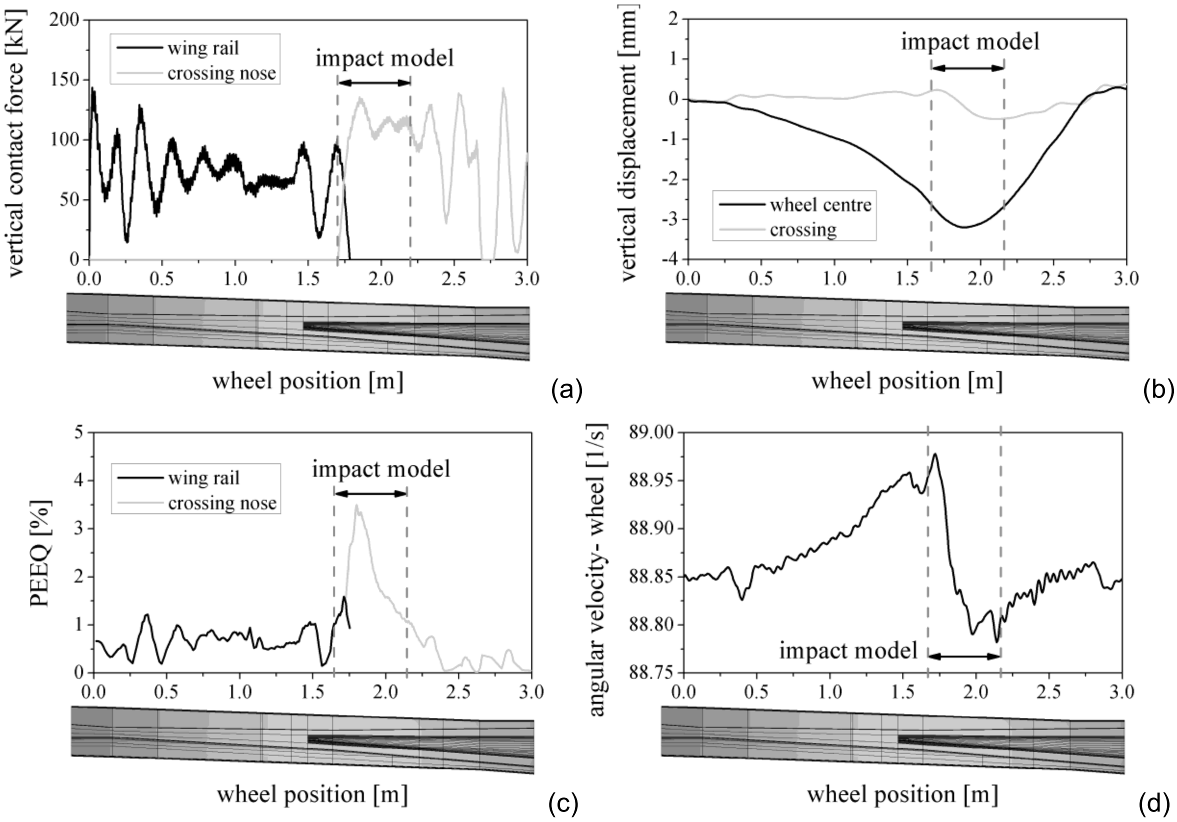

Figure 3: Results of the crossing model with a train speed of 160 km/h and facing move. The curves show (a) the vertical contact forces between the wheel and the crossing parts, (b) the vertical displacement of the wheel centre and the crossing, (c) the plastic strains in the Manganese steel crossing after one cycle and (d) the angular velocity of the wheel. The region that is separately modelled in the impact model is indicated by dashed lines.

The model uses explicit time integration and is solved with the commercial code ABAQUS/Explicit. In the model of the wheel and the crossing nose the mesh has been refined in the regions where the wheel and the crossing nose contact each other. Tie-constraints connect the parts with different element sizes and these connections are carefully put into areas where they do not alter the stress and strain results in the regions of interest. The crossing nose consists of three parts and contains a total of 134 000 elements. The wheel is divided into four parts and consists of 123 000 elements. The resulting edge length of the contacting elements is less than 1.8 mm.

In Figure 4 the mechanical model of the *impact model* is drawn. On the bottom, the crossing nose is rigidly connected to a spring/dashpot element that represents the structure below the crossing. A spring constant c_t of 180 kN/mm and a dashpot constant k_t of 250 kNs/m are assumed. At the bottom of the crossing nose, a point mass is applied to represent a total mass of the crossing of 680 kg – i.e. the same mass as used in the crossing model. The wheel is modelled with a rigid disk (radius of 116.5 mm) in its centre. The wheel is vertically damped by a dashpot (damping constant of 53kNs/m), which represents the primary suspension of the bogie. A vertical load of 79.7 kN (corresponding to an axle load of 14.2 tons) is applied in the wheel centre. In the longitudinal direction the wheel moves with a fixed velocity of 160 km/h. It has an initial angular velocity of 88.97 rad/s and is free to change its angular velocity throughout the calculation.

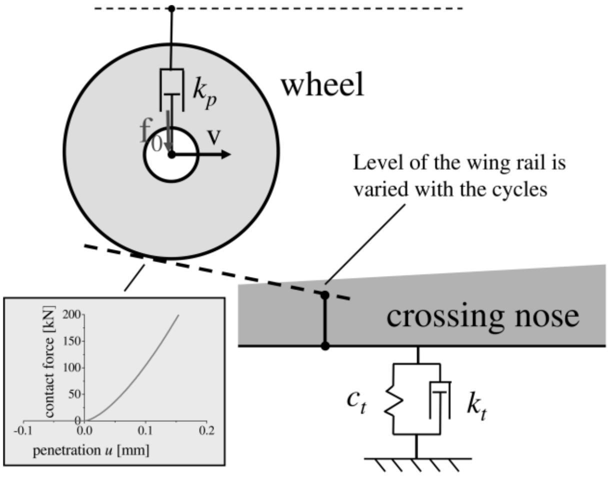

Figure 4: Impact model. The wheel is loaded by a static load and connected to a vertical dashpot that represents the primary suspension of the bogie. Concerning the bedding of the crossing the whole crossing nose is connected on the bottom to a spring/dashpot element. Before impacting onto the crossing nose the wheel runs on a simplified model for its contact to the wing rail. For this contact, the force/penetration curve based on the Hertz formulas is shown.

The wheel can approach the crossing nose along different levels (representing the running path of wheels due to e.g. worn and unworn wheel profiles) along the wing rail. Higher levels are associated with a later impact of the wheel on the crossing nose. In section 3.2.3, this will be used to account for the statistical distribution of wheel profiles, train speeds and axle loads. The vertical initial positions of the wheels have been varied between 0 mm and 1.6 mm, resulting in varied longitudinal impact positions between 0.05 m and 0.35 m.

To consider the influence of the second wheel on the angular velocity of the axle, a frictional element is used that has been developed for the *crossing model* [4]. The influence of the wing rail on the angular velocity of the wheel (the angular velocity increase before the impact) determines the initial angular velocity. In the *impact model* no further acceleration due to the wheel's run along the wing rail is considered.

To account for the contact of the wheel with the wing rail, the centre of the wheel is vertically connected to a contact spring. It is assumed that the contact situation does not change in the longitudinal direction. Using the Hertzian formulas [14], the contact stiffness can be derived from the elastic constants of the material and the geometry represented by the radii of the contacting bodies. For the wheel and wing rail, a Young's modulus of 210 GPa and a Poisson's ratio of 0.3 is used. A wheel radius of 0.5 m is assumed while the radius in the lateral direction is infinite. For the wing rail, the radius in the longitudinal direction is infinite and 40 mm in the lateral direction. These values result in a penetration of the contacting bodies *w* of

$$w(F) = 3.92 \cdot 10^{-8} \frac{N^{3/2}}{m} \cdot F^{2/3} \tag{1}$$

Although the geometry of the contact changes slightly along the wing rail, this formula is used for the whole distance. A constant inclination of the wing rail (angle of 0.223 degrees) is assumed, which defines the downward movement of the wheel during the start of the calculation.

Initially, the spring of the crossing's bedding and the contact spring are compressed according to the vertical load on the wheel. Subsequently, the vertical load is applied in the wheels centre, causing some oscillations of the contact force between the wheel and the simplified wing rail. At the point where the wheel impacts onto the crossing nose those oscillations have already faded away.

To start with, the calculations were carried out for different initial wheel positions and an elastic material behaviour of the crossing only. Results of this elastic model are shown in section 3.2.1. Subsequently, 21 cycles have been calculated with the lowest (or first) vertical wheel position (0 mm) and for the three materials including their plastic properties, see section 3.2.2. In another calculation, 21 wheels with 10 varying positions (0, 0.2, 0.4, 0.6, 0.8, 1, 1.2, 1.4, 1.6, 0, 0.2 mm, …) roll over the turnout. The different levels account for the different wheel profiles or train velocities that may appear in the track and results for this case are shown in section 3.2.3.

3 Results and discussion

3.1 Parameters of the plastic material model

Based on the tensile tests and the LCF tests with two strain amplitudes per material (Table 1) parameters for a Chaboche-type cyclic elastic-plastic material model [15] have been fitted. This material model can be directly integrated into ABAQUS, using three back-stress tensors for the kinematic hardening and one parameter for the cyclic isotropic hardening. The fitted parameters are given in Table 2.

Table 2: Elastic-plastic material parameters of the three investigated materials: *Mn13*, *Hardox* and *Marage*.

	Mn13	**Hardox**	**Marage**
E [GPa]	201	210	189
ν [1]	0.3	0.3	0.3
r_0 [GPa]	0.2	0.75	1.7
C_1 [GPa]	1000	500	2600
D_1 [1]	10000	5000	36000
C_2 [GPa]	40	120	340
D_2 [1]	400	600	3400
C_3 [GPa]	2	21.5	50
D_3 [1]	3	79	330
Q [GPa]	0.25	-0.25	-0.65
B [1]	3	1	0.8

In Figure 5, a part of the experimental results and the behaviour of the fitted material model are shown. In the tensile test, the three materials clearly differ, with *Mn13* having the lowest, *Hardox* the intermediate and *Marage* the highest yield stress. After the yield point, they show a completely different plastic behaviour. For *Mn13* and a strain amplitude of 0.9 % the full stress-strain curves are shown for the first, the fifth and the 50th cycle in Fig 5b. Plots of the cyclic maxima and minima of the three materials versus the cycle numbers are shown in Figure 5c and 5d. For tests with similar strain amplitudes (0.9% for *Hardox* and *Mn13* and 1.1% for *Marage*), different stress levels are obtained. *Mn13* shows strong hardening whereas both *Hardox* and *Marage* soften with proceeding cyclic loading. Generally, a good agreement between the experiments and the fitted material model has been reached. The experimental results show a slightly different material behaviour in tension and compression for all materials, but this discrepancy is considered negligible and therefore not included in the material model.

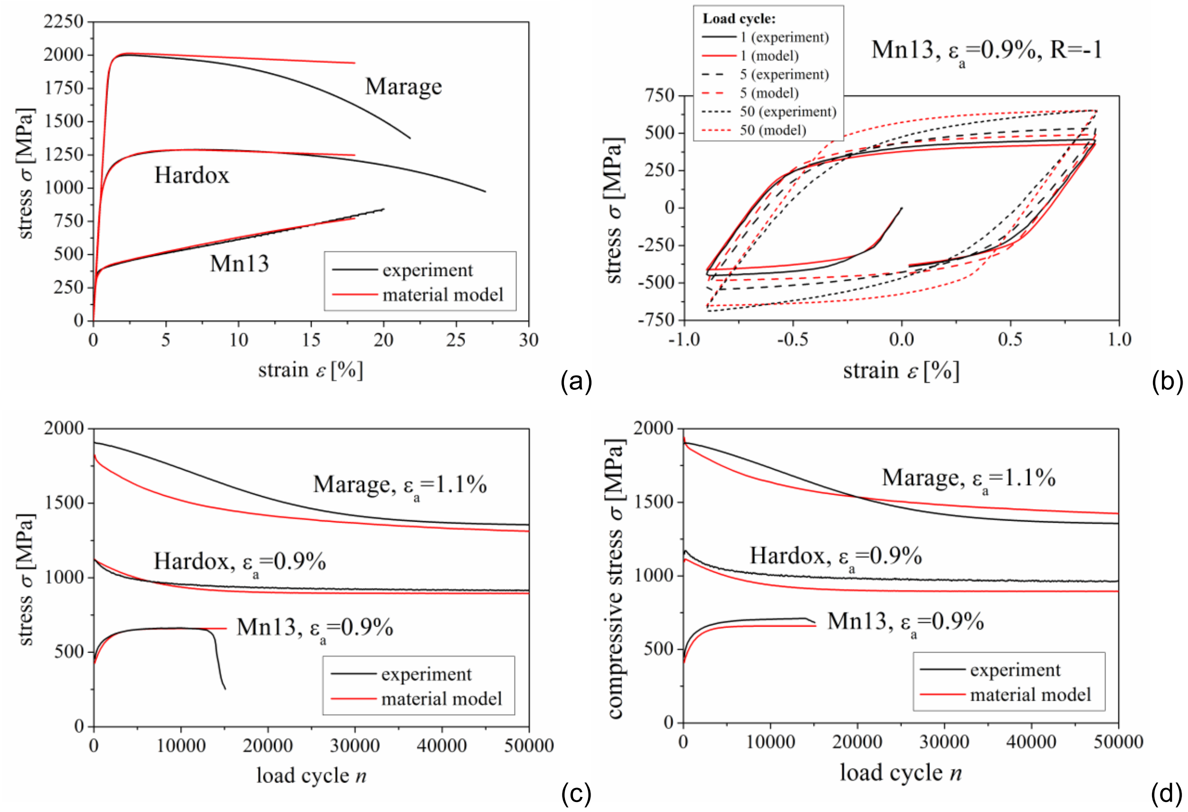

Figure 5: Measured (black curves) and fitted (grey curves) data for the three materials. The curves show (a) the tensile tests for all materials, (b) the cyclic response of *Mn13* with strain amplitude of 0.9 %, (c) the maximum cyclic stress for the lower stain amplitudes of the materials and (d) the corresponding minimum of the cyclic stress.

3.2 Results of the impact model

3.2.1 Elastic results of the impact model

In Figure 6, the results of the model with elastic crossing material and initial vertical wheel positions of 0, 0.4, 0.8, 1.2 and 1.6 mm are shown. The vertical contact forces resulting from the impact are shown in Figure 6a. Note that the definition of the wheel position differs from the *crossing model* shown in Figure 3. In the *impact model*, the position of 0 metres corresponds to the tip of the crossing nose. It can be seen that the impact produces forces that reach values of up to 210 kN, i.e. more than two times the static load (79.7 kN). The impact of the wheel occurs farther in longitudinal direction for the wheels with higher initial positions. The maximum contact forces are slightly higher for the later impacts of the wheel. The vertical displacements of the wheel centre are illustrated in Figure 6b. As the wheel initially runs on the wing rail, it linearly lowers its position. After the impact oscillations of the vertical wheel displacements can be seen. They correspond to the oscillations of the contact forces, see Figure 6a.

The calculated contact areas of the contact patch between the wheel and the crossing nose are shown in Figure 6c. The contact areas increase towards the end of the crossing nose as the contact radius of the crossing nose increases. The contact patch can reach a size of 150 mm^2 corresponding to a circle with a diameter of 14 mm. The division of the vertical contact forces by the contact area results in the average contact pressure plotted in Figure 6d.

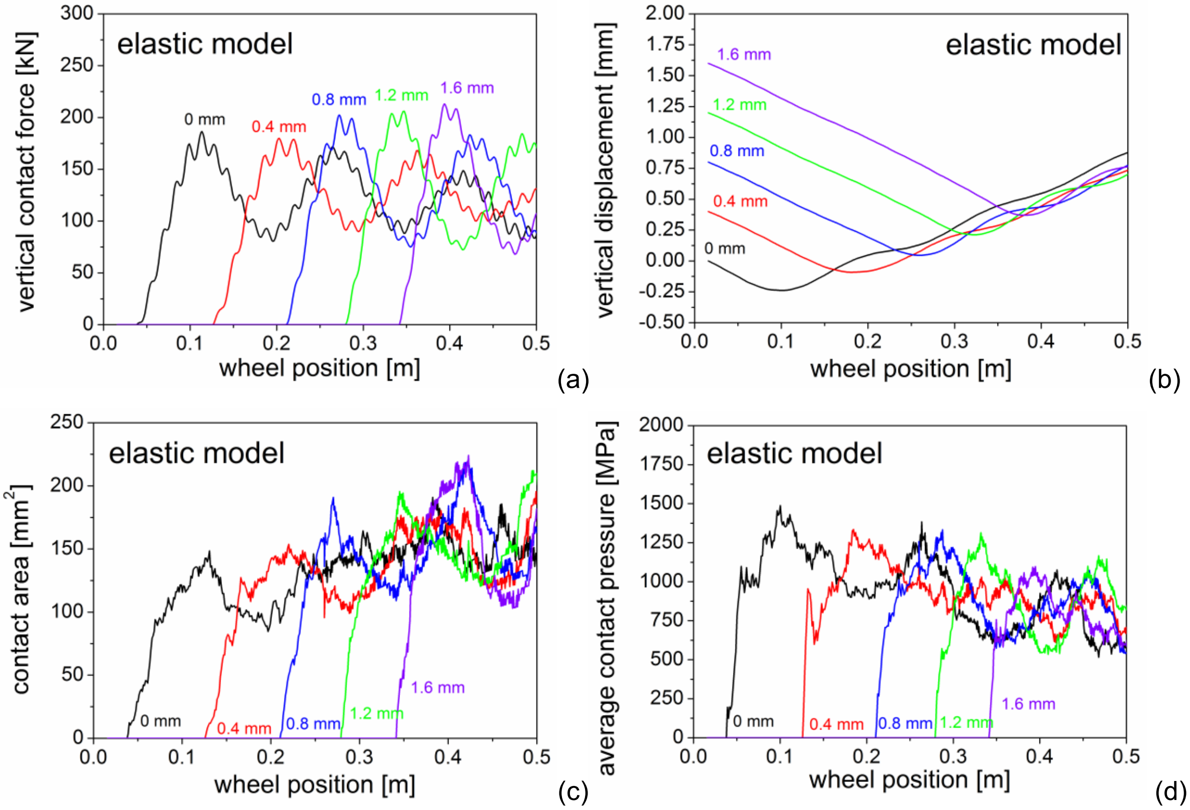

Figure 6: The results of the impact model with elastic behaviour of the crossing. For the levels of 0, 0.4, 0.8, 1.2 and 1.6 mm, (a) the vertical contact force between wheel and crossing nose, (b) the vertical displacement of the wheels centre, (c) the contact area and (d) the average contact pressure are shown.

3.2.2 Loading by wheels impacting at the *same position*

The results for a series of 21 wheels impacting onto the crossing nose with initial positions of 0 mm are plotted in Figure 7. The change in the vertical contact forces due to consecutive impacts as well as the change in the average contact pressure influenced by the ongoing plastic deformation is illustrated. The results for the three materials *Marage*, *Hardox* and *Mn13* are shown for the first, the 11th and the 21st cycle.

Fig 7a,c,e shows the evolution of the vertical contact forces. With *Marage* as crossing material, the calculations indicate nearly no change in the force results during the first 21 cycles. For *Hardox* the plastic deformation of the crossing causes a slight increase of the contact forces during progressing impacts. For *Mn13*, the highest contact forces are obtained further away from the tip of the crossing nose. Due to the plastic deformation and thus geometric adaption the contact forces of the first cycle are smaller than the forces of the calculations with elastic material response. At higher load cycles, however, the vertical contact forces reach higher values than in the case of the elastic calculations. This can be attributed to an excitation of additional oscillations due to the development of a deep dent caused by impacts of the wheel at the same position of the *Mn13* crossing nose. At a wheel position of about 0.35 m, the wheel nearly loses contact with the crossing nose. Concerning the dynamic contact forces this adaption in the form of a dent of the *Mn13* crossing is not beneficial. However, this dent will only be produced as a result of the unrealistic case of identical impacts meaning new wheels having exactly the same profile, same running position, same running velocity and same load during the loading of a new crossing nose.

The average contact pressure of the *same position* loading is shown in Figure 7b,d,f. In contrast to the contact force an effect of the small plastic deformation in the case of *Marage* crossings on the contact pressure is found. During the first cycle, the contact pressure is nearly identical with the elastic case (maximum of 1488 MPa). After 11 and 21 load cycles, however, some plastic deformation accumulates, causing the highest average pressure to drop from 1437 MPa (first cycle) to 1136 MPa (11th cycle) and 1134 MPa (21st cycle). A similar effect can be seen in the model with the *Hardox* crossing, where the plastic deformations are higher than the ones for *Marage* and the average pressure drops from 1408 MPa (first cycle) to 1102 MPa (11th cycle) and 1069 MPa (21st cycle) during the impact. For *Marage* and

Hardox crossings the plastic deformation of the first load cycle mainly causes that decrease of the average pressure. The following cycles contribute much less. The manganese steel crossing shows a clear adaption and decrease of the average contact pressure to 793 MPa during the impact of the first cycle. With the proceeding plastic deformation and geometrical adaption the average pressure is further lowered to 636 MPa in the 11th and 611 MPa in the 21st cycle despite the fact that the material hardens. Due to the opposing effects of the geometric adaption of the crossing and the hardening of the *Mn13*, the adaption process almost stops after a few cycles. Thus, elastic shakedown is nearly reached.

The cause for the evolution of contact forces and the decrease of the average contact pressure can be assigned to the change in the longitudinal and lateral crossing profile. This is illustrated in Figure 8. The longitudinal profile change of the crossing is shown in Figure 8a. The vertical position of the contact point initially rises linearly towards the end of the crossing. After 20 wheels have impacted on the crossing at the same position, some waviness of the crossing profile can be seen. For *Mn13*, this adaption is very pronounced with a dent depth of 0.35 mm, whereas for *Hardox* there is only a slight change (up to 0.07 mm dent depth) at the tip of the crossing, and for *Marage* there is nearly no change. As the wheel has to follow the deformed profile during the following impacts, additional oscillations are introduced into the system. The slower and later impact for the *Mn13* can be understood with this picture, as well as the higher contact forces and the bouncing of the wheel after the wheel has reached a position of 0.3 metres in the diagram, see Figure 7e.

In Figure 8b, the maxima of the accumulated equivalent plastic strain (PEEQ) are shown for the three materials after the 20th load cycle. The *Marage* crossing shows only little deformations with plastic strains of up to 0.74 %. For *Hardox*, the PEEQ reaches values of up to 5.8 % and for *Mn13* of up to 21.5 %. High plastic deformations are obtained for the *Mn13* crossing nearly over the whole modelled length of the crossing nose. At a wheel position of 0.1 m, the *Marage* and *Hardox* crossings show their highest PEEQ values. For *Mn13*, the highest PEEQ is reached at a wheel position of 0.2 m.

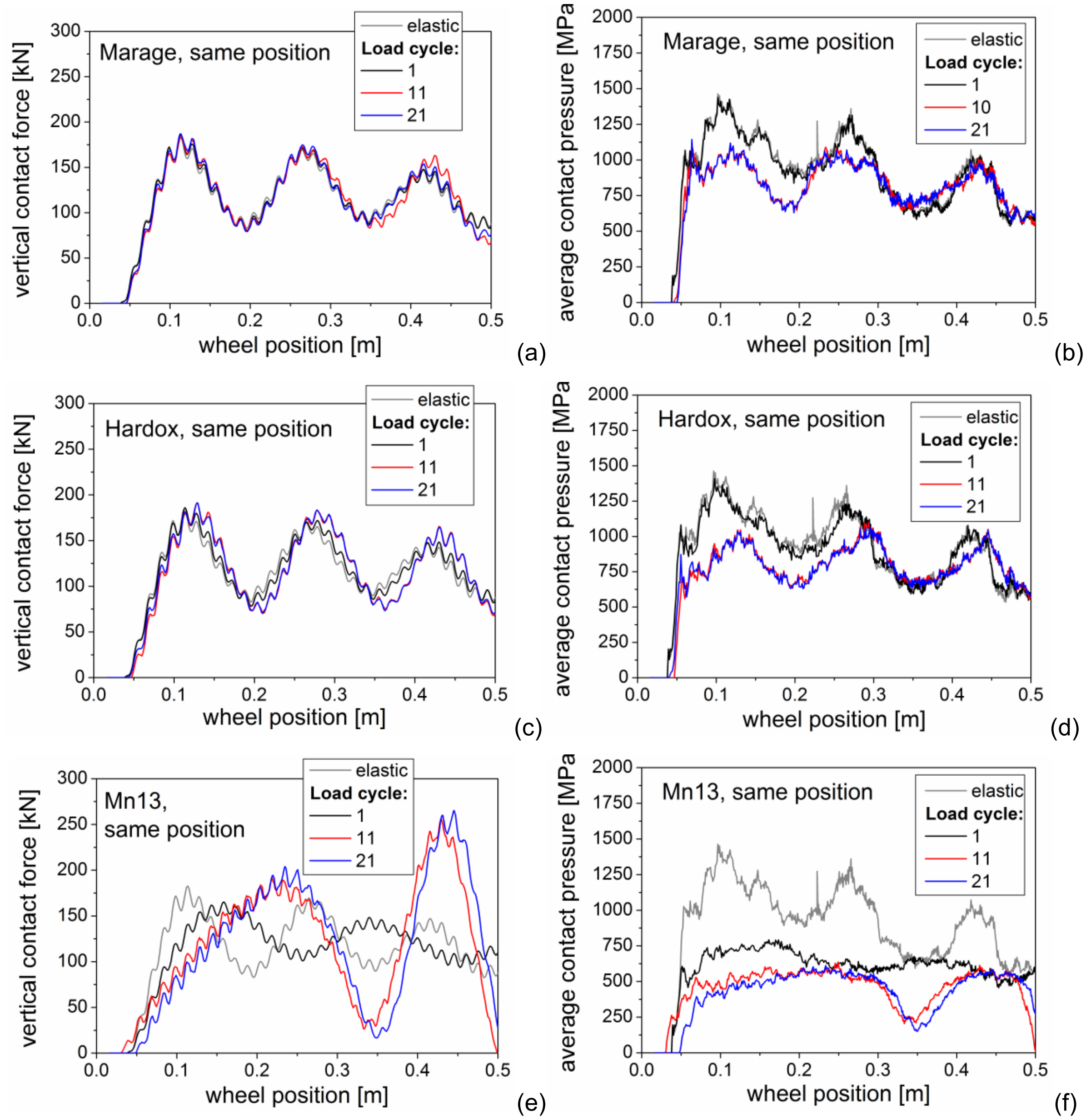

Figure 7: Evolution of the vertical contact force and the average contact pressure with the load cycles with the same initial wheel positions. The first, the 11th and the 21st cycle are illustrated. As a reference, the results of the elastic model are given in all diagrams. The curves show the results for (a),(b) *Marage*, (c),(d) *Hardox* and (e),(f) *Mn13* as crossing materials.

Deformed cross-sections of the crossing nose after 20 cycles of loading at the two longitudinal positions of 0.1 m and 0.2 m are shown in Figure 8c,d. A general tendency of the crossing nose to deform towards a conformal contact profile matching the wheel profile is observed. The corresponding deformation rate depends on the hardness of the crossing nose. It can be seen that *Marage* shows practically no plastic adaption during the first 21 cycles, whereas *Hardox* shows a slight adaption in the cross-section at a position of 0.1 m. *Mn13* easily adapts to the contact loading, particularly at a position of 0.2 meters, where the highest vertical contact forces arise. The adaption is associated with an increase in the size of the contact patch and thus in a decrease in the contact pressure.

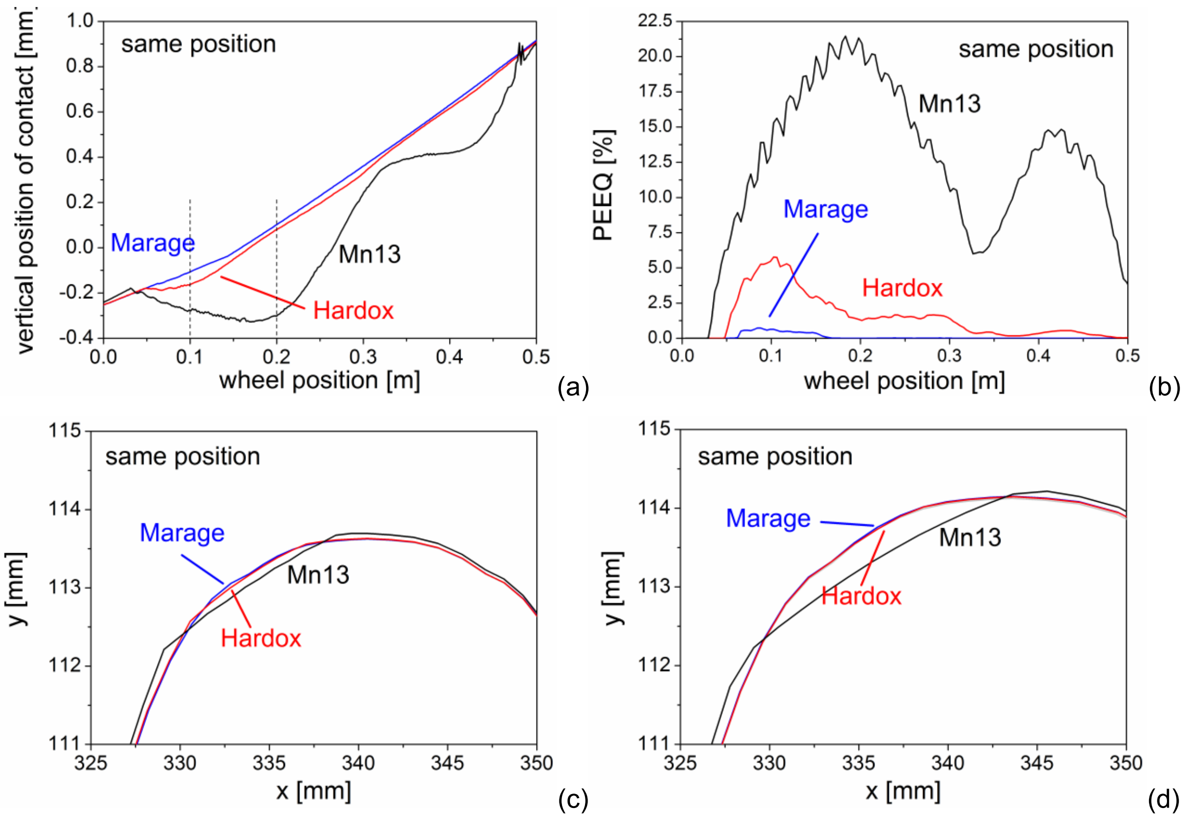

Figure 8: The crossing nose after 20 load cycles with *same position* loading for the three investigated materials. Results of (a) the vertical positions of the contact point over the wheel position, (b) the maximum accumulated equivalent plastic strain (PEEQ) at all wheel positions, the deformed crossing profile at a wheel position of (c) 0.1 metres and (d) 0.2 m. In the diagrams of the crossing profiles, different scales (factor of 5) have been used in the x and y direction to visualize the small profile changes.

3.2.3 Loading by wheels with *varying position*

Since in reality wheels on a train are different regarding the running profile, size and running position, consecutive wheels impact on statistically varying longitudinal positions on the crossing nose. Due to restrictions in computational time it is not possible to simulate real statistics of different wheels. Therefore, a limited set of possible positions has been chosen. The results are shown in the following.

Figure 9 shows the same results as for the *same position* calculations (Figure 7), but this time for the *varying* initial impacting *positions*, produced by 10 different wheel levels. Since this type of loading produces a distribution of the positions of the first impact at the crossing nose, less plastic deformation can be expected during the first 21 cycles at one distinct position. 10 different wheel positions have been considered;

during the first, the 11th and the 21st cycle the wheel impacts at the same longitudinal position (level of 0 mm), and therefore these cycles can be compared in the following diagrams.

In Fig 9a,c,e, it can be seen that the highest forces of the first cycle are slightly lower than the values of the elastic calculation. This is valid for all investigated materials. For the subsequent loading of the crossing, however, the contact forces slightly increase in the *Marage* and the *Hardox* simulations. For *Mn13*, the highest contact forces are not necessarily obtained during the first impact but sometimes during the following oscillations and a further position on the crossing. Compared to the calculations with *same position* of the wheel, the contact forces are reduced regarding the first impact and the following oscillations. This is a result of the plastic deformation and an advantageous adaptation of the geometry of the crossing nose.

The average contact pressure is shown in Figure 9b,d,f. Similar to the model with the same wheel position, the pressure decreases due to the plastic deformation mainly caused by the first load cycle. Later on, only small changes are obtained. In the *Mn13* crossing, due to the heavy plastic deformation the contact pressure in the first cycle is clearly lower (800 MPa) than in the elastic model. In the following load cycles, the highest average pressure reaches values of about 640 MPa. For *Hardox* and *Marage*, there is also a tendency of the average pressure to decrease with advancing cycles. For the model with *varying position* loading, however, there are some tolerances in the relative vertical position between rail and crossing. For *Marage*, this causes the average pressure of the 21st cycle with 1334 MPa to be higher than the 11th cycle with 1139 MPa because the wheel impacts earlier on the crossing nose.

In Figure 10a, the vertical position of the centre of the contact patch – representing the running level of the wheel - is shown after 20 wheels have passed (impacting at different positions). It can be seen that for the two better adapting materials (*Hardox*, and *Mn13*) a fairly uniform deformation and even shape of the crossing nose is produced in longitudinal direction. For *Mn13*, this results in a decrease of the vertical contact forces with progressing loadings. The accumulated equivalent plastic strains (PEEQ) are more or less uniformly distributed along the crossing. The highest values of the PEEQ after 20 cycles of loading are 0.5 % for *Marage*, 3 % for *Hardox* and 14.4 % for *Mn13*.

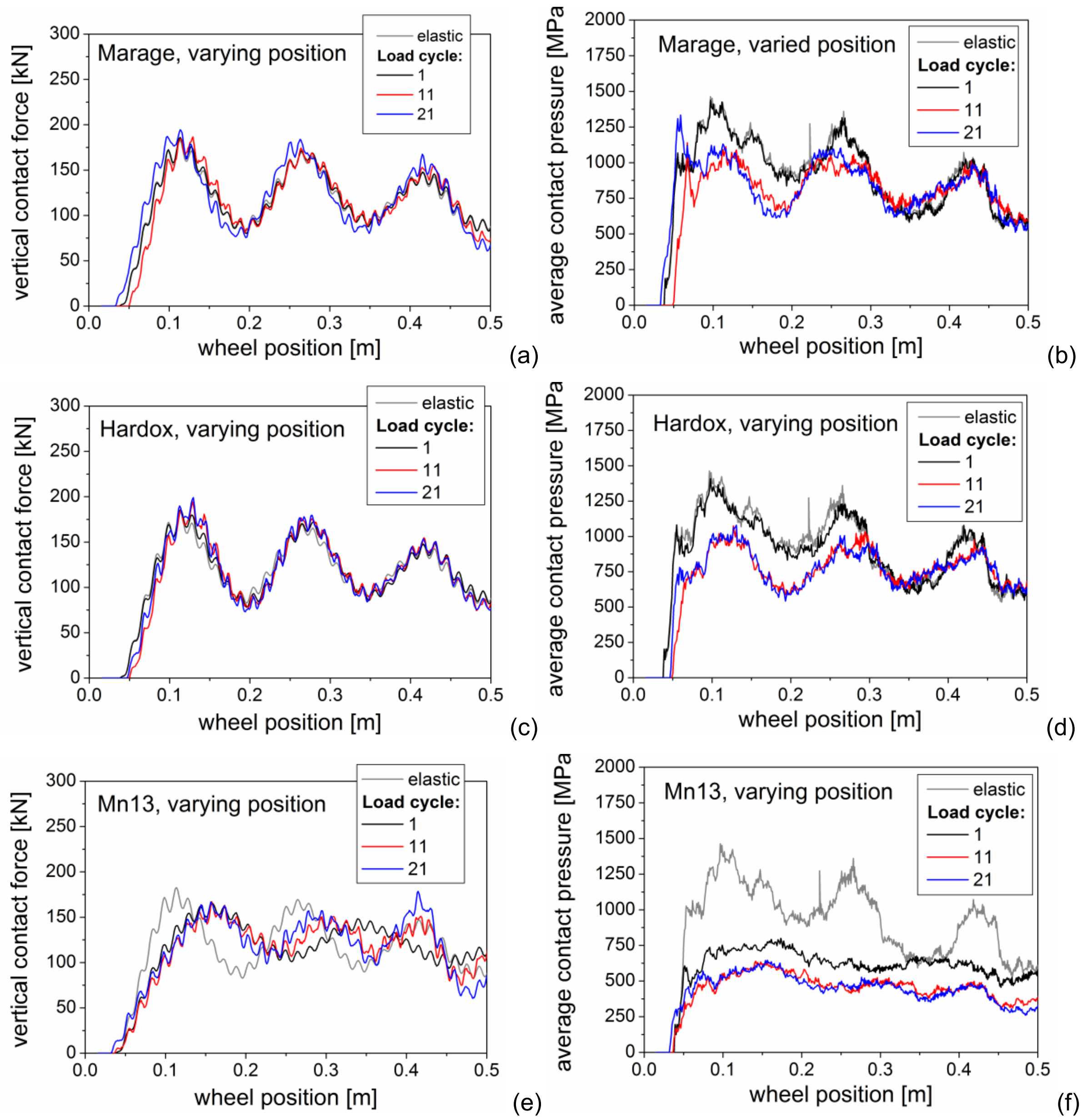

Figure 9: Evolution of the vertical contact forces and the average contact pressure with the load cycles with *varying position* loading. The first, the 11th and the 21st cycle are illustrated. As a reference, the results of the elastic model are given in all diagrams. The results for (a),(b) *Marage*, (c),(d) *Hardox* and (e),(f) *Mn13* as crossing materials are shown.

The deformed cross-sections after 20 cycles, shown in Figure 10c,d, are similar to the ones for *same position* loading but over a longer longitudinal distance . The highest vertical displacements of the surface are smaller with *varying position* loading.

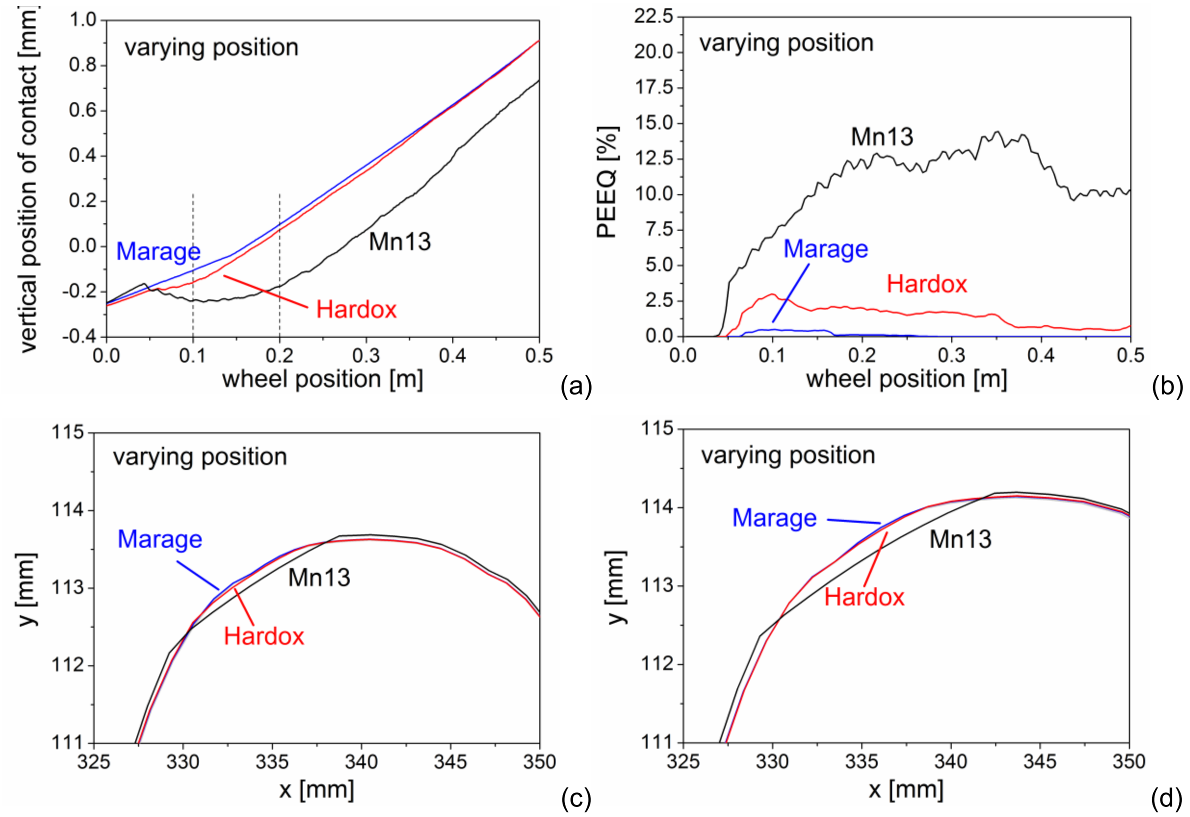

Figure 10: The crossing nose after 20 load cycles with *varying position* loading for the three investigated materials. Results of (a) the vertical positions of the contact point over the wheel position, (b) the maximum accumulated equivalent plastic strain (PEEQ) at all wheel positions, the deformed crossing profile at a wheel position of (c) 0.1 metres and (d) 0.2 m. In the diagrams of the crossing profiles, different scales (factor of 5) have been used in the x and y direction to visualize the small profile changes.

3.3.4 The tendency of the crossing to form dents

In Figure 8a, the loading with *same position* causes waviness in the crossings surface for *Mn13* and a less pronounced one for *Hardox*. Different initial wheel positions, on the other hand, show a more uniform deformation of the surface, see Figure 10a. The wave formation in *Mn13* crossings excites high contact forces and subsequent oscillations, see Figure 7e. This unrealistic case increases the dynamic loads, which in turn further increase those deformations.

The key factor for this wave formation is the uniformity of the loading. The more uniform the wheel profiles, the train speeds, the bogies and the axle loads are, the more the crossing tends to form waves. The exact role of the material behaviour in these models will be the subject of further calculations. Waviness produced after some cycles is favoured by materials with low yield stress. Whether harder materials with cyclic softening behaviour tend, on a longer term, to form dents cannot be clarified by the presented work due to the extensive amount of cycles (more than

1000) needed for this kind of investigation. It can be assumed that softening materials tend to increase existing dents whereas hardening materials may have the ability to smooth out dents if the loading position is not always the same.

3.3 Reduction of loads as result of the crossings geometrical adaption

From Figure 7 and Figure 9, it can already be seen that the average contact pressure is reduced by the plastic deformation of the crossing nose.

In Figure 11, contour plots of the vertical stresses σ_{yy} are shown at a wheel position of 0.2 m for the 21st cycle of loading with varying wheel positions. To highlight the effect of the plastic deformation on the stresses, the results of the elastic model are shown, too.

In the elastic model, the vertical stress (and thus the contact pressure) reach a minimum value of 2215 MPa (maximum contact pressure of 2215 MPa). At this wheel position, the model with the *Marage* crossing shows with a maximum contact pressure of 2212 MPa no significant decrease in the stresses. For *Hardox*, the contour plot shows that the contact patch has increased in size and the highest contact pressure is reduced to 1674 MPa. The *Mn13* crossing adapts best and reduces the maximum contact pressure to 935 MPa.

From these results it can be concluded that the crossing profile can in the case of *Mn13* easily approach the shape of the wheel profile in the contacting region. This change of the contact radii causes a nearly conformal contact and the lateral size of the contact patch increases. In the longitudinal direction the size of the contact patch stays about the same. For similar vertical contact forces the contact pressure is thus drastically reduced.

This lateral geometric adaption is determined by the plastic material behaviour of the crossing nose. The three materials used in this work can be seen as representative for very hard steel (*Marage*), a steel with an intermediate hardness and good wear resistance (*Hardox*) and a rather soft but in proceeding cycles hardening material (*Mn13*). In the first 20 cycles that are calculated in this work the *Mn13* already shows a distinct and *Hardox* a slight adaption. For *Hardox* and *Marage* there might be some more adaption in the following cycles but the model does not allow for such high cycle numbers yet. For higher cycle numbers abrasive wear may also cause an adaption of the profile.

As one of the assumption in the presented calculations only one single wheel profile has been used. In practice, there exists a statistical distribution of wheel profiles and presumably the crossing will adapt in the lateral direction towards an average of those profiles. This means that the presented model overestimates the effect of reduction of contact pressure since it can fully adapt to fit the given wheel profile. Such an adaption might cause higher contact stresses if a different wheel profile runs over the deformed crossing nose.

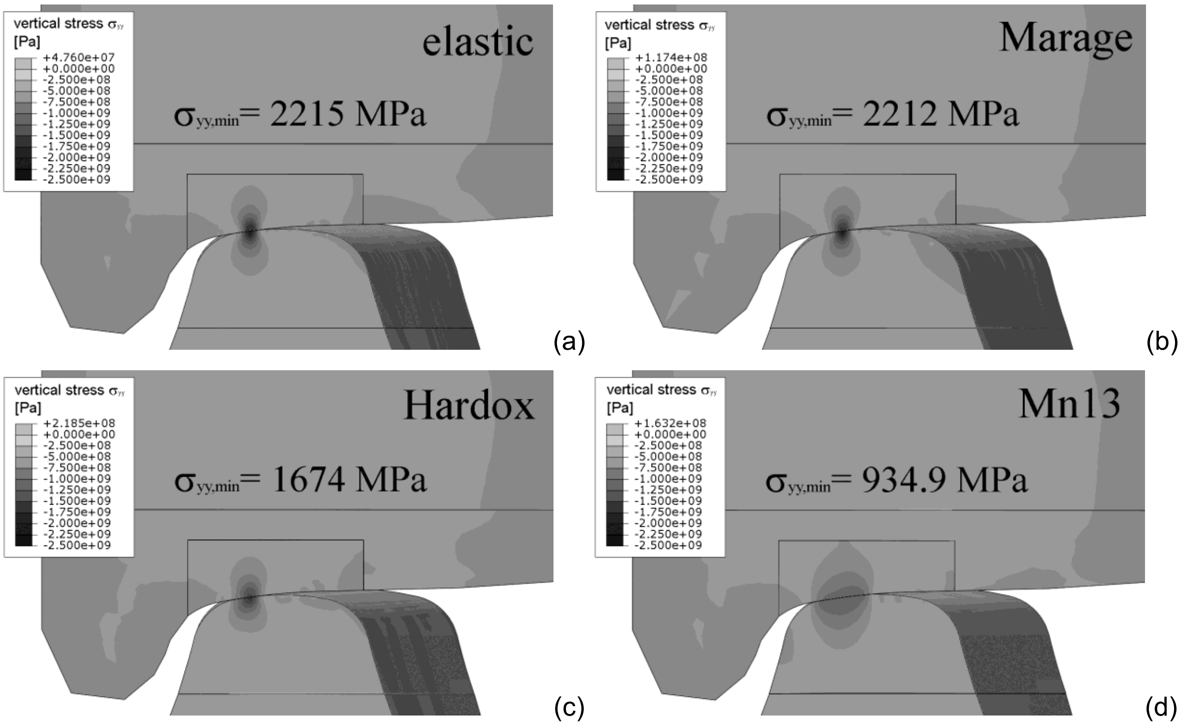

Figure 11: Comparison of the vertical stresses in wheel and crossing as the wheel is at a position of 0.2 m (according to the diagrams). Results for the elastic model are shown in (a). The 21st cycle of the model with *varying position* loading is shown for a crossing material of (b) *Marage*, (c) *Hardox* and (d) *Mn13*.

In Table 3 the highest contact stresses for all materials and types of loading are given. Results for two sections (0.1 metres and 0.2 metres) are shown. The trend of the significant decrease of stresses with softer materials, illustrated in Figure 11, is valid for loading with *same position* and *varying position* in both sections.

At the 0.1 m section, the decrease of the contact stresses for *Mn13* is even more pronounced than at the section at 0.2 m. An interesting result is that for *Mn13* nearly the same maxima of contact pressure are reached on both positions.

The different adaption in the longitudinal direction means that the results of the contact pressure depend on the type of loading (*same* or *varying position*). At the

0.1 m section, the *same position* loading results in a better adaption with the lower pressure values. At the 0.2 m section, the *varying position* gives the better adaption and the lower pressure values.

Table 3: Highest contact pressure for the different materials and types of loading in the 21st load cycle.

maximum contact pressure $p_{c,\max}$

[MPa]

	section at 0.1 m		section at 0.2 m	
position	same	varying	same	varying
Marage	3000	3143	2218	2212
Hardox	2206	2380	1892	1674
Mn13	1002	1086	1002	935
elastic	3112		2215	

4 Conclusions

A model that describes the adaption of the crossing nose to its dynamic contact loading allows for several conclusions: Generally, the contact stresses are reduced by the plastic deformation of the crossing. In the lateral direction, the size of the contact patch increases, causing the reduction of stresses. This effect can be regarded as *geometric shakedown*.

A material that adapts and shows at the same time a sound wear resistance can be considered ideal for crossing noses. Such a material would have a low yield stress and a good hardening behaviour, such as the widely used Manganese steel. Very hard materials, such as the investigated maraging steel *Marage*, show no or only a very slow adaption in the first 20 cycles and thus feature higher contact stresses. Due to the cyclic softening of *Marage*, subsequent cycles can cause plastic adaption at a later stage and likewise adaption due to wear. Note that deformations associated with this adaption were only about 0.5 mm and are thus in the order of magnitude of the production tolerance.

The main factor for the performance of the crossing in the track is the wear and rolling contact fatigue (RCF) resistance in its adapted geometry. In this work the reduction of the contact stresses due to plastic deformation has been studied. Materials that do not adapt may still perform well because they might have a very high wear and RCF resistance.

In addition, the effect of loading under the same conditions is described with the presented model as very special case (it is not realistic). If very similar loading conditions occur over several cycles, a longitudinal waviness in the crossing profile may appear increasing the dynamic contact forces. Materials that have low yield stresses and that show plastic softening favour this effect. Using different levels for the approaching wheels from wing rail to the crossing nose and thus different impact positions on the crossing nose, a more or less uniform deformation of the crossing is produced. In this case, the dynamic contact forces do not increase with the proceeding adaption, as no dents will form in the crossing profile.

The presented model does not allow for a final judgment about the performance of different materials used as crossing noses because it only considers the first 20 cycles of loading. In harder materials a similar adaption might occur in several thousand cycles. Manganese steel behaves very tolerant concerning high plastic deformations that are needed for the adaption. In harder materials this adaption might be associated with damage. The surprisingly good performance of the soft Manganese steel can be explained with its ability to adapt fast to the loading situation, thereby reducing the contact stresses.

Acknowledgements

Financial support by the Austrian Federal Government (in particular from the Bundesministerium für Verkehr, Innovation und Technologie and the Bundesministerium für Wirtschaft und Arbeit) and the Styrian Provincial Government, represented by Österreichische Forschungsförderungsgesellschaft mbH and by Steirische Wirtschaftsförderungsgesellschaft mbH, within the research activities of the K2 Competence Centre on “Integrated Research in Materials, Processing and Product Engineering”, operated by the Materials Center Leoben Forschung GmbH in the framework of the Austrian COMET Competence Centre Programme, is gratefully acknowledged.

References

[1] Kassa, E., and Nielsen, J. C. O., 2008, "Stochastic Analysis of Dynamic Interaction between Train and Railway Turnout," Vehicle System Dynamics, 46(5), pp. 429-449.

[2] Kassa, E., 2007, Dynamic Train-Turnout Interaction: Mathematical Modelling, Numerical Simulation and Field Testing, PhD Thesis, Chalmers University of Technology, Gothenburg, Sweden.

[3] Wiest, M., 2007, Modeling of Wheel-Rail/Crossing Interactions, PhD Thesis, University of Leoben, Austria.

[4] Pletz, M., Daves, W., and Ossberger, H., 2009, "A Dynamical Wheel Set: Crossing Model Regarding Impact, Sliding and Deformation," Proc. 8th International Conference on Contact Mechanics and Wear of Rail/Wheel Systems, Florence, Italy, pp. 801-809.

[5] Smith, R. W., and Mackay, W. B. F., 2003, "Austenitic Manganese Steels - Developments for Heavy Haul Rail Transportation," Canadian Metallurgical Quarterly, 42(3), pp. 333-341.

[6] Widmark, M., Melander, A., and Meurling, F., 2000, "Low Cycle Constant Amplitude Fully Reversed Strain Controlled Testing of Low Carbon and Stainless Sheet Steels for Simulation of Straightening Operations," International Journal of Fatigue, 22(4), pp. 307-317.

[7] Wiest, M., Daves, W., Fischer, F. D., and Ossberger, H., 2008, "Deformation and Damage of a Crossing Nose Due to Wheel Passages," Wear, 265(9-10), pp. 1431-1438.

[8] Johansson, A., Paulsson, B., Ekh, M., Nielsen, J. C. O., Ander, M. K. A., Brouzoulis, J., and Kassa, E., 2010, "Simulation of Wheel/Rail Contact and Damage in Switches & Crossings," Wear, 271(1-2), pp. 472-481.

[9] Nicklisch, D., Kassa, E., Nielsen, J., Ekh, M., and Iwnicki, S., 2010, "Geometry and Stiffness Optimization for Switches and Crossings, and Simulation of Material Degradation," Proceedings of the Institution of Mechanical Engineers, Part F: Journal of Rail and Rapid Transit, 224(4), pp. 279-292.

[10] Kalker, J. J., 1982, "A Fast Algorithm for the Simplified Theory of Rolling Contact," Vehicle System Dynamics, 11(1), pp. 1-13.

[11] Pletz, M., Daves, W., and Ossberger, H., 2010, "Dynamic Finite Element Model of a Wheel Passing a Crossing Nose," Proc. Tenth international conference on computational structures technology, Valencia, Spain, on-line.

[12] Pletz, M., Daves, W., and Ossberger, H., 2011, "A Wheel Passing a Frog Nose- Dynamic Finite Element Investigation of High Axle Loads," Proc. International heavy haul association conference, Calgary, Canada, on-line.

[13] Abaqus, Abaqus User's Manual, Version 6.9, www.abaqus.com.

[14] Kunz, J., 2009, "Kontaktprobleme und ihre Praktische Lösung," Konstruktion, 61(11/12), pp. 54-58, in German.

[15] Chaboche, J. L., 1989, "Constitutive Equations for Cyclic Plasticity and Cyclic Viscoplasticity," International Journal of Plasticity, 5(3), pp. 247-302.

Paper D

Prediction of Rolling Contact Fatigue in Crossings - Multiscale FE Model

M. Pletz
W. Daves
W. Yao
H. Ossberger

Proceedings of the 9th International Conference on Contact Mechanics and Wear of Rail/Wheel Systems (CM2012)

Prediction of Rolling Contact Fatigue in Crossings - Multiscale FE Model

Martin Pletz [1,2], Werner Daves [1,2], Weiping Yao[2] and Heinz Ossberger [3]
1) Institute of Mechanics, Montanuniversität Leoben, Leoben, Austria
2) Materials Center Leoben Forschung GmbH, Leoben, Austria
3) VAE GmbH, Zeltweg, Austria

Abstract

In this work finite element models at different length scales are applied to predict the performance of three different crossing materials (Manganese steel, Hardox and Marage 300) in view of the development of rolling contact fatigue (RCF) cracks. A model of the whole crossing (crossing model) is used for the calculation of the dynamic forces and movements of wheel and crossing. For the prediction of RCF repeated loadings have to be calculated, but only a reduced model permits a sufficiently fine mesh and reasonable computing times. Therefore, a simplified model of the wheel and the crossing nose (impact model) is developed, which uses the dynamic movements of the crossing model as boundary conditions. The accumulation of plastic strains in the crossing, the build-up of residual stresses and the geometric adaption of the crossing to the loads is studied for 81 load cycles. The contact pressures, shear stresses and residual stresses of the impact model with the adapted geometries of the 81st cycle are applied to a two-dimensional model with a surface crack (crack model). Using data from measured crack growth curves, the three materials can be compared in terms of crack development and growth.

1 Introduction

In the railway track structure, turnouts allow trains to change from one track to another. In contrast to the rails with unchanging constant profile in the running direction, the profile of the crossing nose and the wing rail changes throughout the turnout. In the crossing panel the rail is discontinuous but under normal operations the wheel stays in contact all the time either with the wing rail or the crossing nose or both. As the wheel runs onto the crossing nose, it has to change its velocity vector in vertical direction and this causes a vertical impact. Due to geometric restrictions, the crossing nose has a small radius at its tip. For the facing move (the wheel runs initially on the wing rail and impacts on the crossing nose) the small radius of the crossing nose together with the impact produces very high contact pressures. In addition, the different rolling radii of the wheel on the wing rail and the crossing nose cause slip during the time of the impact.

The high contact pressure can cause severe cyclic plastic deformation. Contact pressure and slip are the driving forces for wear and rolling contact fatigue (RCF), which limit the service time and the lifetime of crossings. In Figure 1, a crossing nose with such surface cracks is shown. Generally, the ideal crossing material should have a high wear resistance and a high resistance to crack initiation and growth.

Figure 1. A crossing nose with RCF cracks. With a longitudinal slip, they are perpendicular to the running direction of the wheel.

The process of a wheel passing a crossing is highly complex. The parameters are the passing direction, the axle load, the train speed, the wheel profile, the bogie design and of course the geometry and bedding of the crossing. There are some approaches to capture the dynamics of this process with numerical models. One way is the use of multibody system dynamics with the ability to describe a whole train as it runs over a turnout [1]. Another possibility, developed by the authors of this work, is using an explicit finite element code to model one wheel and three metres of the turnout (including the crossing). Some assumptions are made concerning the movement of the wheel over the crossing, which means that it disregards some effects of the bogies and the whole train’s movement. On the other hand, it provides a practical tool to study and understand damage relevant effects in detail.

In previous works by the authors [2, 3], two important mechanisms have been identified: First the vertical movement of the wheel and the crossing (involving the impact), and second the change in the angular velocity of the wheel set resulting in slip. The effect of the crossing's bedding, the train velocity and the axle load are further parameters of the investigations.

The dynamic process of a wheel running over a crossing nose is significantly dependent on the crossing material. In this work three materials are selected for which the loading of a surface crack will be described. These materials are a 13% Manganese steel, in the literature referred to as Hadfield steel [4] ("Mn13"), a maraging steel that is defined in the ASTM norm as "Marage 300" ("Marage") and a steel with a hardness that lies in between Mn13 and Marage ("Hardox").

2 Modelling

2.1 The crossing model

A model for the crossing has been developed using the finite element code ABAQUS/Explicit [5] by the authors [3, 6, 7]. In this model, a three metre part of the crossing is modelled, in which the wheel changes from the wing rail to the crossing nose. The mesh of the model can be seen in Figure 2. The influence of various parameters on the crossing's loading can be investigated. The calculated results include the maximum vertical contact forces, the wheel movement, the longitudinal position of impact on the crossing nose, the contact pressure, the slip and the plastic strains. Certain assumptions about the boundary conditions are made, see [6].

With this *crossing model* that contains about 250,000 elements causing calculation times of 8h on an up-to-date four-core computer, cyclic studies are very time-consuming. The crossing model contains elements with an edge-length of 3 mm in the contacting areas, which is sufficient for a good description of the dynamics and a rough but usually sufficiently accurate description of contact pressure, slip and plastic deformation. However, for a more detailed study of the adaption of the crossing nose (in terms of stresses and strains), the calculation times have to be reduced and the elements in the crossing nose have to be refined.

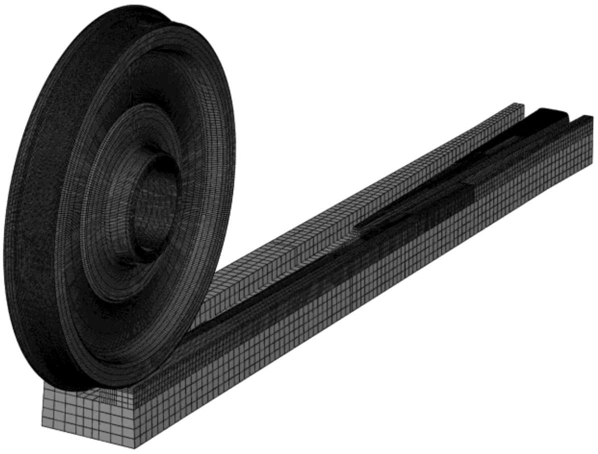

Figure 2: The crossing model with the wheel, two wing rails and the crossing nose. A total length of 3 metres is modelled.

2.2 The impact model

For the calculation of the cyclic loading of the crossing nose, the *impact model* is devised consisting of only a 0.6 metre part of the crossing nose, in which the wheel impact occurs. A picture of the mesh is shown in Figure 3. The case of the facing move (wheel initially running on the wing rail and impacting onto the crossing nose) is investigated. The parameters of the investigations are a new wheel profile, a train speed of 160 km/h and an axle load of 14.2 tons. For this load case, the results of the *crossing model* are applied to the *impact model* as described in [8].

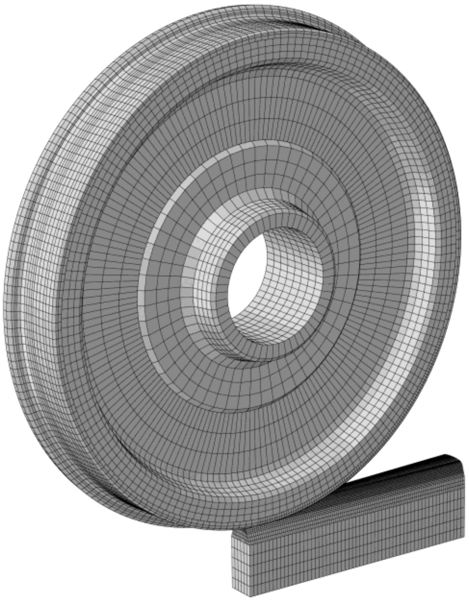

Figure 3: The impact model with the wheel and 0.6 metre part of the crossing nose.

Concerning the crossing geometry, a standard crossing of the type 760-1:15 (UIC 60 rails) is used. The unworn profile of an UIC-ORE 1002-type wheel is used as wheel geometry. The mass of the wheel is taken with 1025 kg and the moment of inertia of the whole axle is set to 135.5 kgm^2. The contact between the wheel and the crossing nose is modelled with a Coulomb friction coefficient of 0.3. The edge length of the contacting elements is less than 1.8 mm.

The wheel can approach the crossing nose along different levels (representing the running path of the wheels due to e.g. worn and unworn wheel profiles) along the wing rail. Higher approaching levels are associated with a later impact of the wheel on the crossing nose. For the vertical initial level positions of the wheel, four positions have been chosen: 0 mm 0.2 mm, 0.4 mm and 0.6 mm. During the cyclic calculations, these wheels approach and impact repeatedly on the crossing nose at these levels (in the sequence 0, 0.2, 0.4, 0.6, 0, 0.2 mm, …). A total of 81 cycles are calculated, which corresponds to 20 impacts on each level. In the model the wheel has the elastic behaviour of steel (Young’s modulus of 210 GPa, Poisson’s ratio of 0.3 and density of 7800 kg). For the crossing nose, the three materials Mn13, Hardox and Marage are used. For the corresponding cyclic plstic material behaviour a Chaboche type model is used [9]. Details about the plastic behaviour are given in [8], the flow curves of the materials are shown in Figure 4.

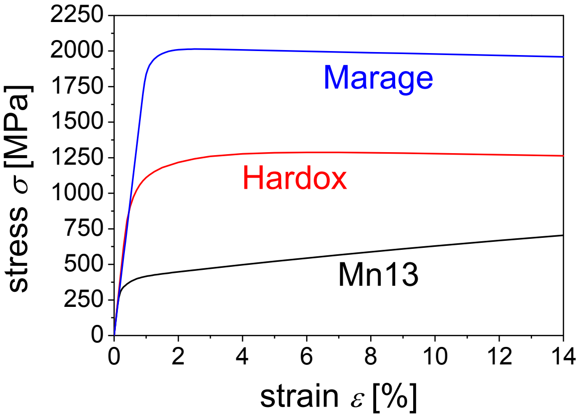

Figure 4. The tensile stress-strain curves of the three materials.

From the results of the impact model, the contact pressures, the contact patch sizes and the slips can be calculated. In the following they are applied in the two-dimensional crack model.

2.3 The crack model

With the loads derived from the 81st load cycle of the crossing noses using different material models the loading of an existing crack is studied in the crack model with and without previously calculated residual stresses in the crossing nose. The mesh of the model is shown in Figure 5. The wheel is modelled with a part of a ring with a thickness of 40 mm. The top and the sides of the wheel part are rigidly connected to a reference point in its centre, where boundary conditions and loads are applied. The crossing nose is modelled with a height of 40 mm and a length of 100 mm. The 2 mm thick top layer of crossing nose and wheel has a refined mesh with element length of 0.2 mm. The crack is modelled in the centre of the crossing nose on its surface. In Figure 5 the crack depth a_d and the crack angle α are shown. At the crack tip, 3-noded elements are used whereas all the other elements are 4-noded. In total, the model contains about 42 000 linear elements with plane strain formulation.

The bottom of the crossing nose part is fixed. Constraint equations for nodes at the sides disable a global strain in the horizontal direction, but allow a global shear strain. The wheel rolls over the crossing nose during a vertical and a longitudinal load and an angular velocity is applied in its centre.

For the evaluation of the crack driving force the concept of configurational forces is employed [10]. In [11] this method is used for studying the interaction between multiple cracks. The crack driving force based on the configurational force concept is similar to the Rice J-integral concept [12] for a linear elastic case, but can also be applied to elastic-plastic materials under cyclic loads because in the formulation of the configurational force only the elastic energy is considered as reusable free energy. In the Rice J-Integral concept the total strain energy (both elastic and plastic) are used (based on deformation theory), which strongly limits its applicability to elastic-plastic materials and cyclic loading cases.

The wheel is modelled elastically with a Young's modulus of 210 GPa and a Poisson's ratio of 0.3. The rail uses the same plastic material model as used in the 3D test-rig model.

For both positions on the rail, taken from the 3D simulation, a crack depth a_d of 1 mm and a crack angle α of 30° are assumed. The angle is defined according to Figure 5. As the wheel always accelerates during running onto the crossing nose, it moves from right to left. The angle of the crack growth direction α_e is defined in the same way as α, see Figure 5. A negative angle <180° thus represents a crack growth towards the surface, an angle of 0° predicts growth parallel to the surface and an angle of 90° predicts growth perpendicular to the surface into the rail. Between the crack faces contact is modelled with a coefficient of friction of 0.3. As in the three-dimensional models, a friction coefficient of 0.3 is used between wheel and crossing parts.

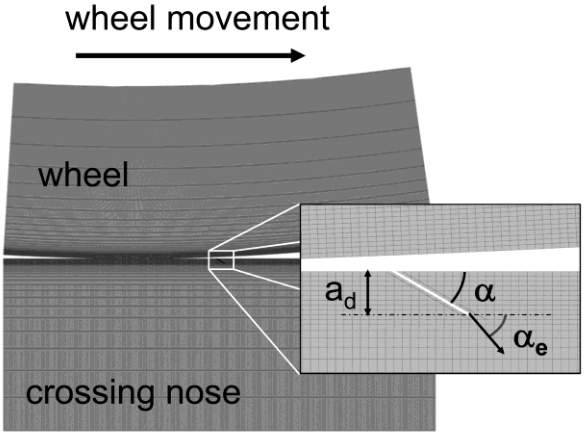

Figure 5. The geometry and the mesh of the crack model for a braking wheel. A close-up of the crack is shown where the crack angle α, the direction of crack extension α_e and the crack depth a_d are defined.

The residual stresses in the crossing are obtained from the impact model. In a two-dimensional plane strain model, only the longitudinal component of those residual stresses is applied. As the longitudinal strain of the rail is hindered in the crack model, the residual stresses from the three-dimensional impact model can be applied through thermal strains. With a virtual coefficient of thermal expansion α_T in the horizontal direction, the applied temperature differences are calculated as:

$$\Delta T(depth) = -\frac{\sigma_x(depth)}{E\ \alpha_T} \tag{1}$$

These temperature differences are applied in the crack model in an initial step.

3 Results and Discussion

3.1 Cyclic results of the impact model

Figure 6a,b,c shows the contact force developments for the three different materials for the first, the 41st and the 81st cycle of loading. It can be seen that through the plastic adaption of the crossing nose the maximum values of the contact forces tend to increase. This small increase of the vertical contact forces is not so important as the contact stresses are strongly reduced by the plastic deformation, see section 3.2. In the two harder materials Marage and Hardox this effect is only small. For Mn13, the plastic behaviour of the crossing nose leads to a contact force development in which the second maximum becomes bigger than the first one. The cause for these changes with proceeding cycles is the longitudinal development of the crossing's profile, which was approximately flat in the nominal geometry prior to deformation. In Figure 6d this profile is plotted after 80 cycles of loading for the three materials. The results for Marage approximately correspond with the nominal profile. For Hardox, there is a small dent in the region of the wheel's impact (wheel position of 0.1 m) with a depth of about 40 μm. The material Mn13 has a bigger dent with a depth of about 400 μm. This explains the increase of the second peak in the contact force development. The first impact of the wheel with the crossing nose is damped and a bigger impact occurs at the end of the dent. In Table 1 the highest values of the vertical contact forces and accumulated equivalent plastic strains (PEEQ) are shown. The change in the longitudinal profiles is associated with a maximum PEEQ of 30% in the Mn13, 6.8% in the Hardox and 0.76% in the Marage crossing. Note that the initial position of impact can cause an increase of the second contact force peak of the Mn13 crossing. In the following investigation of the loading of surface cracks in the crossing only the first peak of the contact forces is chosen to transfer the loads to the crack model. More details about the impact model are given in [8]

Table 1. Results of the impact model

Material	Mn13	Hardox	Marage
Max PEEQ (80 cycles)	30 %	6.8 %	0.76 %
Highest contact force (81st cycle)	225 kN	198 kN	193 kN

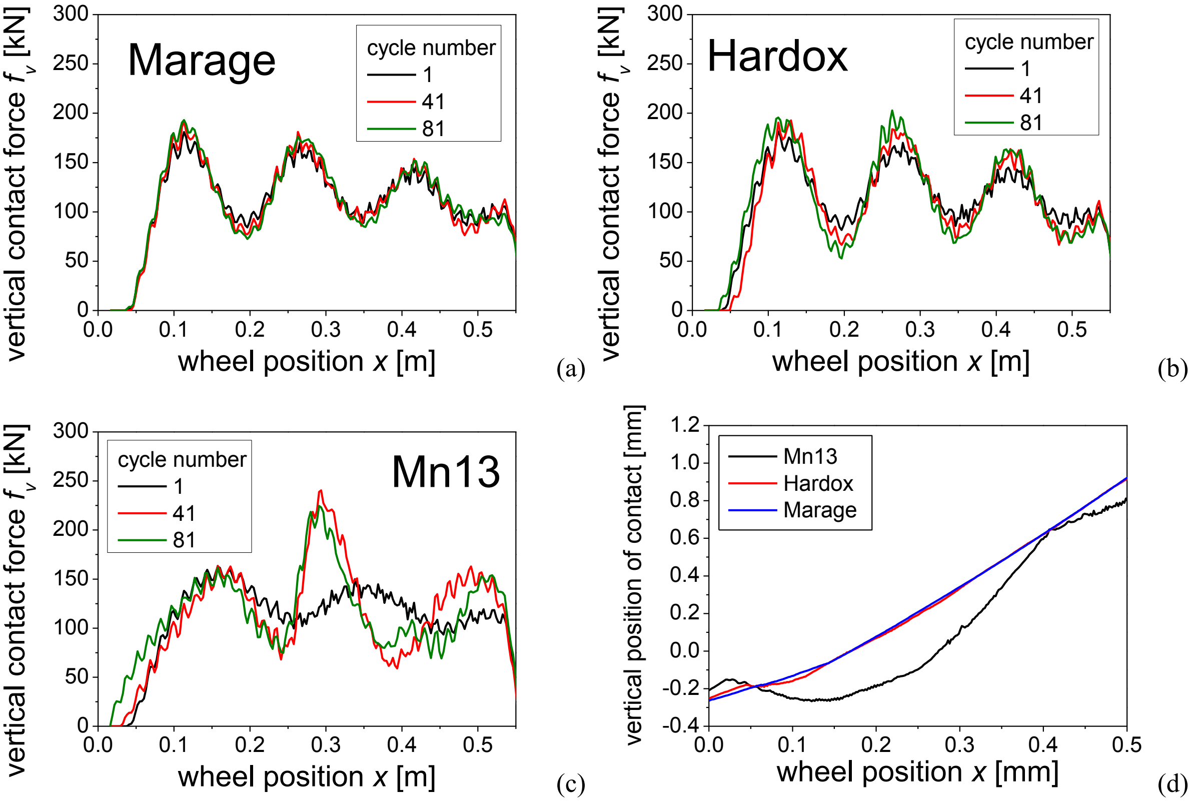

Figure 6. Results of the impact model for 81 cycles of loading and three materials. The curves shwo the vertical contact force developments for a) Marage, b) Hardox, c) Mn13 crossing material and d) the longitudinal crossing profiles for the three materials after 80 cycles.

3.2 Contact force results during the 81st cycle

In Figure 7a the development of the maximum contact pressure is plotted over the wheel position for the 81st cycle of loading. It can be seen that the arising contact pressures are different for the three materials. The softer ones have plastically adapted to the loading and feature lower contact pressures. Towards the end of the modelled crossing nose high contact pressures are calculated between wheel and crossing nose.

Looking at the developments of the slips which are shown in Figure 7b it can be seen that the highest values of about 0.7% are reached during the first contact of the wheel with the crossing nose, which then decrease towards nearly 0%. The slip for the three materials does not show as much difference as the contact pressure between the materials. The crack model needs a certain maximum contact pressure, slip and contact patch size as input. For each material, one position with high contact pressure and also a high slip value is chosen. In Figure 7 this is indicated by dashed lines. The first peak of the contact pressure has been chosen because there are high slips compared to the later ones with higher contact pressures.

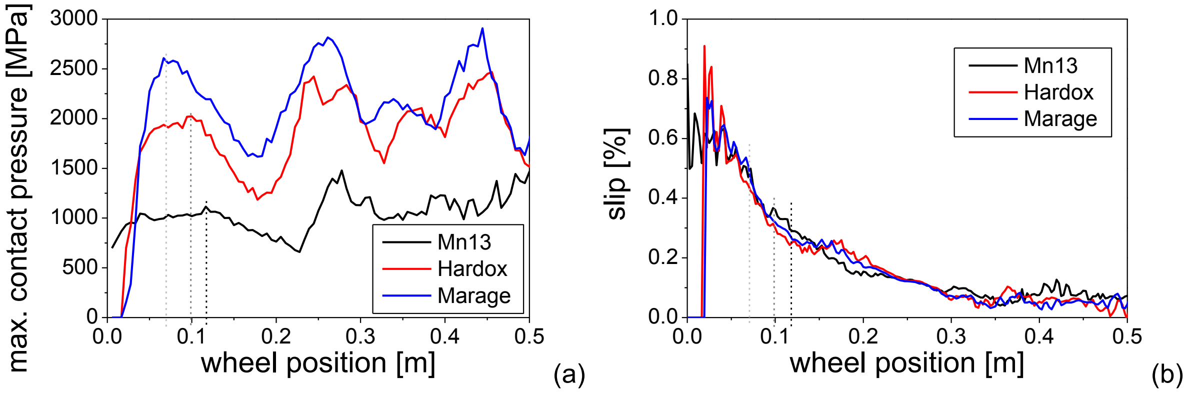

Figure 7. a) Diagram of the highest contact pressure in the 81st cycle of loading plotted over the wheel position, b) Results of slip in the 81st cycle of loading for the three crossing materials. The dashed lines indicate the chosen positions of the three materials for the 2D crack model.

To illustrate the tendency of the contact pressures by first contact of the wheel at the crossing nose for the different materials, a contour plot of the vertical stress (σ_{22}) is shown in Figure 8 for the selected positions that were highlighted in Figure 7 with dashed lines. For comparison reasons additionally to the three elastic- plastic materials the results for a purely elastic behaviour of the crossing material are shown, in which the highest compressive stresses reaches -2987 MPa. The increase in the size of the contact patch can clearly be seen from the difference between the harder and the softer materials with respect to the resulting maximum contact pressure.

In Table 2 the maximum contact pressure, the slip and the longitudinal contact patch size are shown for the selected points of the three materials Marage, Hardox and Mn13. As the selected longitudinal wheel position for the crack model lies for Marage0.07 m ahead of the position of other materials, the slip for the Marage crossing is higher than for the other materials.

Table 2. The maximum contact pressure, the longitudinal contact patch size and the slip from the 81st cycle of the impact model for all three materials for the selected wheel position.

	p_{max} [MPa]	a [mm]	Slip [%]
Mn13	1063	9.2	0.28
Hardox	2020	11	0.3
Marage	2610	11	0.5

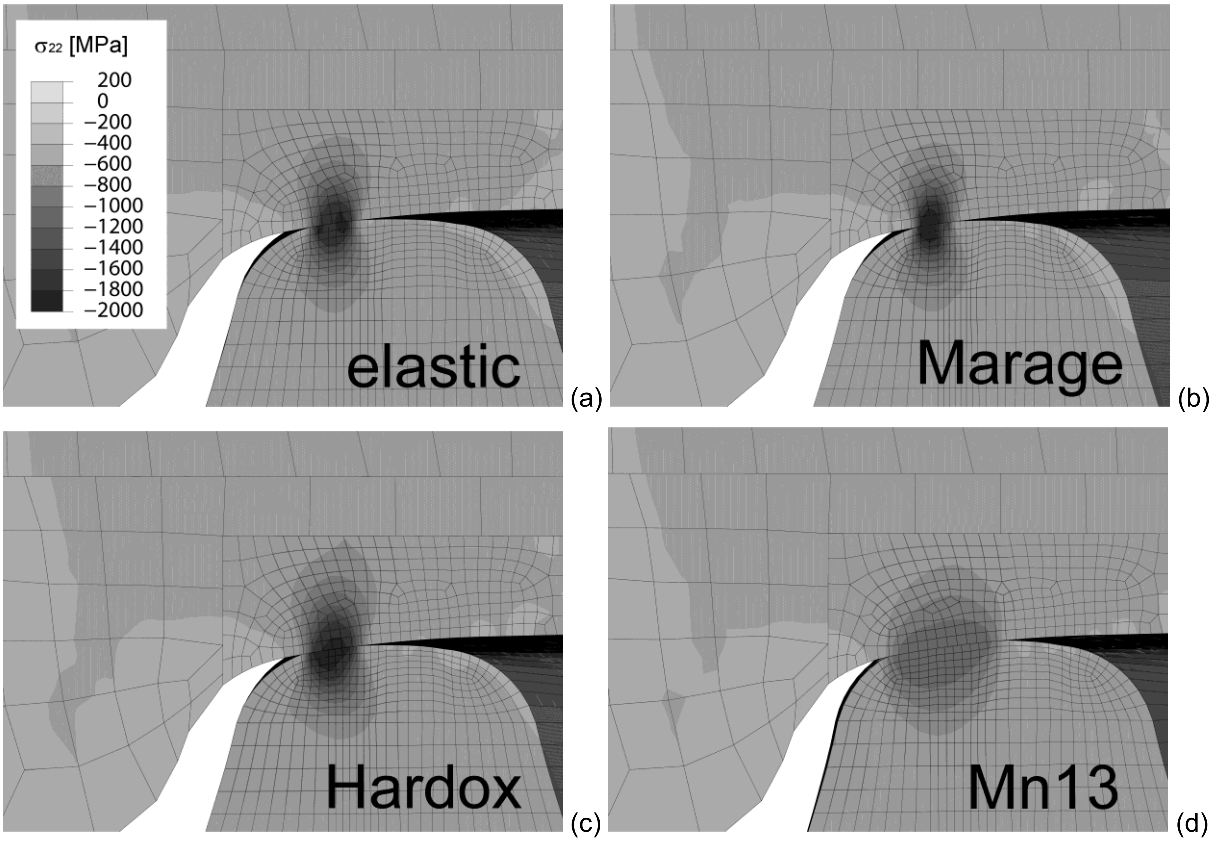

Figure 8. Contour plots of the vertical stresses in the selected positions for a) elastic crossing material, b) Marage, c) Hardox and d) Mn13 crossing material. Results of the 81st cycle of loading are shown.

3.3 Residual stresses after 80 cycles of loading

The plastic adaption of the crossing nose to the loads is associated not only with a different contact patch (reduction of contact pressure) but also with a different development of residual stresses in the crossing. For cracks in the crossing surface, the longitudinal stresses are of primary importance and must be incorporated into the crack model. In Figure 9, a contour plot of those longitudinal residual stresses (σ_{33}) is shown for a Mn13 crossing after 80 cycles of loading. Below the surface, compressive stresses are produced with a value of -221 MPa in a depth of about 6 mm. Below that area of compression in a depth of 18 mm, tensile residual stresses occur with a maximum value of 116 MPa. Directly on the surface, the residual stresses in the longitudinal direction have a value of about -50 MPa.

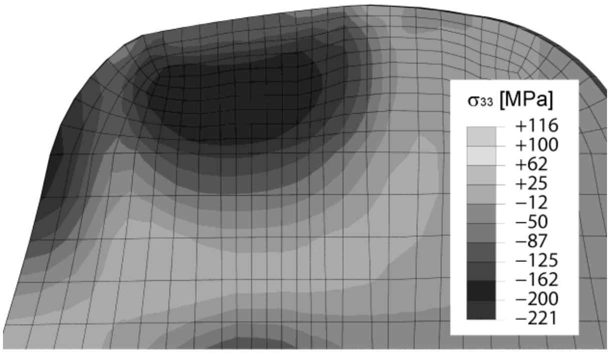

Figure 9. Contour plot of the residual stresses in the longitudinal direction after the 80th load cycle in the Mn13 crossing (results of the 80th cycle are the input for the 81st cycle). Cross- section at the position of the highest contact pressure after cycle 81.

In Figure 10, the longitudinal residual stresses are plotted in depth direction of the crossing for the three materials. As longitudinal position at the crossing nose a cross-section is chosen where the highest contact pressures appear. Table 3 shows the highest arising residual stresses for the three materials and the distance from the surface of their maxima as well as the longitudinal residual stresses in the assumed depth of the crack tip.

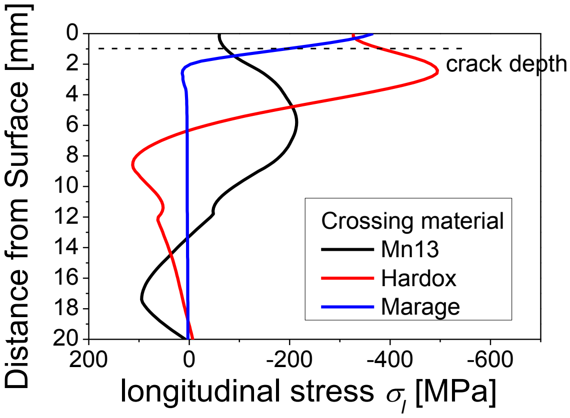

Figure 10. Contour plot of the residual stresses in the longitudinal direction after the 80th load cycle in the Mn13 crossing. Cross- section at the position of the highest contact pressure in cycle 81.

It can be seen that for Hardox and Marage, even higher residual stresses develop than in the initially soft Mn13 material For Hardox, the highest compressive stresses reach a value of -495 MPa in a depth of 2.4 mm. For Marage, the highest compressive residual stresses are directly on the surface with a value of -366 MPa.

Table 3. Longitudinal residual stresses in the crossing nose.

	Highest residual compressive stress [MPa]	Depth of maximum [mm]	Stress in depth of crack tip [MPa]
Mn13	-214	5.8	-73
Hardox	-495	2.4	-384
Marage	-366	0 (surface)	-193

3.4 Results of the crack model

Applying the loading of the selected wheel positions in the impact model (given in Table 2) for the three materials to the two-dimensional crack model, the development of the crack driving force can be calculated, see Figure 11. Both the results without and with the residual stresses taken from the impact model are plotted. The J_{tip} value is plotted over the wheel position (wheel moves from the left to the right) in Figure 11a for Mn13, Figure 11c for Hardox and 11e for Marage. For the determination of the possible crack growth direction the J_{tip} value is additionally plotted over the predicted crack growth angle in Figure 11b for Mn13, 11d for Hardox and 11f for Marage. From these pictures the maximum crack driving force can be directly related to the crack growth angle. The points of the maximum J_{tip} values are numbered so that the wheel position where certain crack growth angles occur can be identified. In Table 4 the maximum values of J_{tip} for all 6 cases (three materials with and without residual stresses) are shown. For a Mn13 crossing, the crack tip driving force J_{tip} is reduced only slightly by the residual stresses and for Hardox and Marage the residual stresses clearly reduce J_{tip}. In the model with residual stresses, Mn13 has the lowest J_{tip} due to the lower contact pressure and thus the lower shear stresses.

In all cases the wheel is accelerating on the crossing nose. In Figures 11a,c,e the wheel moves from the left to the right. For the Mn13 crossing (Figure 11a) only small J_{tip} values are reached before the wheel runs over the crack (wheel position < 0 mm). The maximum J_{tip} value of 1980 J/m^2 is reached just after the contact patch has moved over the crack at a wheel position of 7 mm. This maximum is associated with a crack growth angle of 34°, as can be seen in Figure 11b. In the Mn13 crossing, only small compressive stresses of -73 MPa exist in the depth of the crack tip (as denoted in Table 3) and therefore, the maximum J_{tip} values in the model with residual stresses are with 1900 J/m^2 nearly as high as without residual stresses.

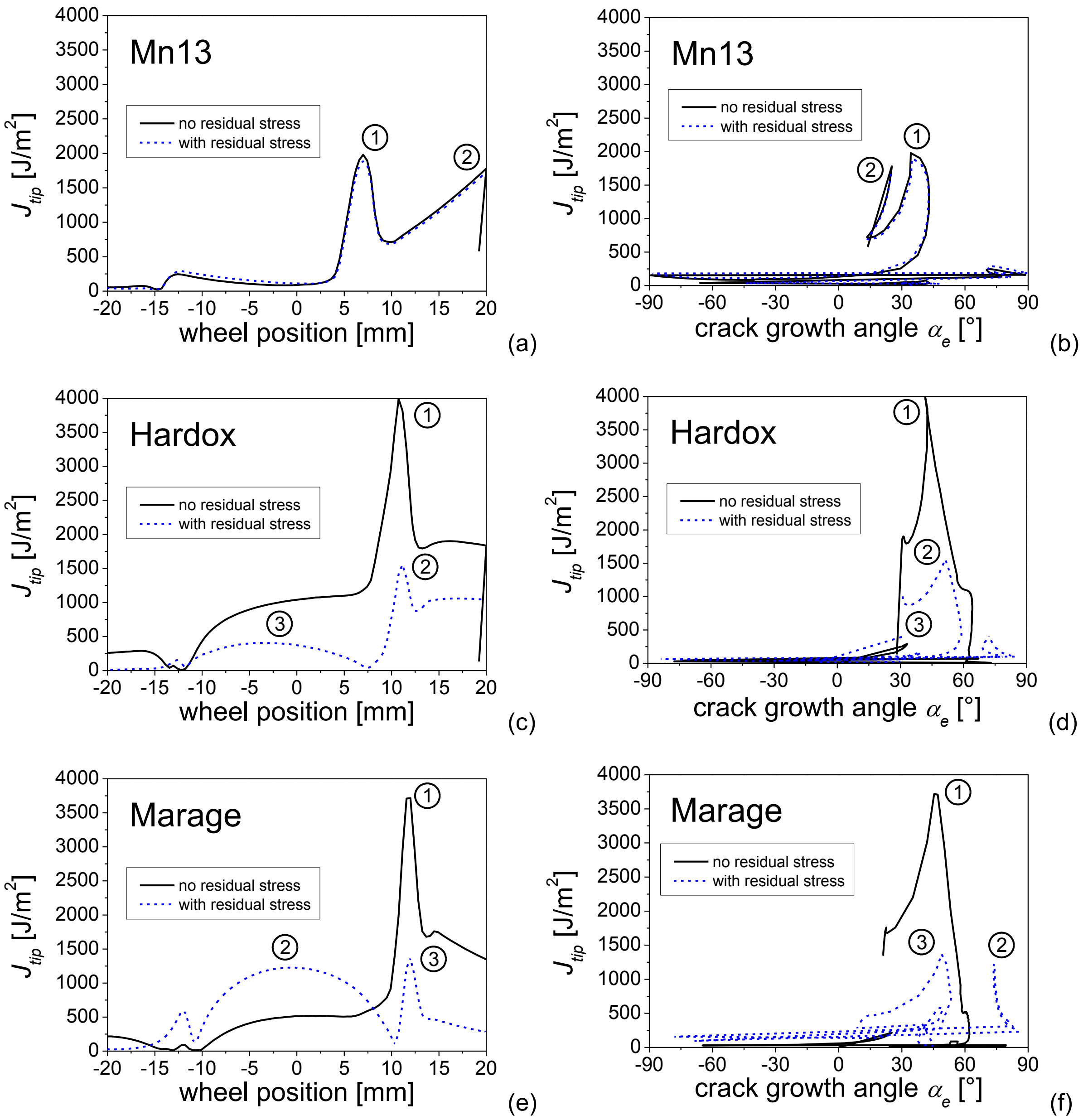

Figure 11. The results of the calculated J_{tip} value from the crack model. is the curves shoe the J_{tip} value along the wheel position (relative to the crack tip at position 0) for a) Mn13, c) Hardox and e) Marage and the J_{tip} value plotted over the angle of crack growth (α_e) for b) Mn13, d) Hardox and f) Marage. Selected points of the highest J_{tip} values during the wheel passage are marked.

For the Hardox crossing as shown in Figure 11c and 11d, the J_{tip} values in the model without residual stresses already increases to values of about 1000 J/m^2 as the wheel runs onto the crack (wheel position of 0 mm). As for the Mn13 crossing the maximum J_{tip} value is reached right after the wheel has passed the crack, reaching a value of 3990 J/m^2 at a wheel position of 11 mm with a predicted crack growth angle of 42°. Taking into account the residual stresses in the Hardox crossing the model gives significantly reduced J_{tip} values. The maximum is reduced to 1560 J/m^2 with a steeper crack angle of 51°. When the wheel is nearly directly over the crack (wheel position of -3 mm), there is another maximum of the J_{tip} value calculated in presence of residual stresses. This maximum, however, reaches J_{tip} values of not more than 450 J/m^2.

Table 4. Maximum values of the J_{tip} value and the corresponding crack growth angles for the three materials and the two cases without and with residual stresses.

	J integral J_{tip} [J/m^2]	Crack growth angle α_e [°]
Mn13	1980	34
Mn13, residual stress	1900	35
Hardox	3990	42
Hardox, residual stress	1560	51
Marage	3720	45
Marage, residual stress	1370	49

The results for the Marage crossing are shown in Figure 11e and Figure 11f. The development of the J_{tip} value for the model without residual stresses is similar to the results of Hardox, but with lower J_{tip} values with a maximum of 3720 J/m^2 at a wheel position of 12 mm. The crack growth angle for that maximum is 45°. By introducing residual stresses from the impact model the J_{tip} value is also considerably reduced. The maximum reaches a value of 1370 J/m^2 at a wheel position of 12 mm, which is even lower than the calculated value of the Mn13 crossing. In the cases with applied residual stresses the J_{tip} value has another peak at a position nearly directly over the crack (wheel position of -2 mm). Here it reaches a value of 1400 J/m^2 with a crack angle of 75°. For the critical J_{tip} values a series of experiments is necessary. This will be the subject of a future research project.

4 Conclusions

Models on three length scales are employed to calculate the driving force on existing cracks in crossing noses. Three materials with different hardnesses are compared: the very soft Manganese steel Mn13, the Hardox steel with a higher hardness and the very hard maraging steel Marage. On the level of the impact model the plastic adaption of the crossing nose to the loading is described, which reduces the contact pressures and shear stresses and thus the driving forces on the crack. It is shown that the soft Mn13 steel features less than half the contact pressures as the hard Marage steel. This is probably one reason for the good performance of Manganese steel used in crossings. The impact model also calculates the residual stresses in the crossing. The longitudinal residual stresses can be applied in the crack model. It is shown that the maximum of those compressive stresses moves towards the surface with increasing hardness of the crossing. Applying the loads from the impact model in the crack model finally shows the effect of the plastic adaption and the residual stresses on J_{tip}. In the calculations without residual stresses the severely adapting Manganese steel shows a lower crack tip loading than the harder Hardox and Marage steels. It is shown, however, that the residual stresses have nearly no effect on the crack driving force in Mn13 for the assumed crack depth. For Hardox and Marage crossings the residual stresses significantly reduce the driving force on the crack to values even less than in the Mn13 crossing. Without data from crack growth experiments (for cracks loaded in the shear mode, the so-called Mode II) no final statement can be made about the performance of the different materials used as crossings. The different fracture toughnesses need to be carefully taken into account and may shift the predicted tendency to develop cracks. The paper is intended to show a straight-forward procedure to evaluate possible rolling contact fatigue in this extremely complex case of a wheel running over a crossing nose. The approach shows that the whole system with the dynamic response, the cyclic plastic material behaviour (geometric adaption of the crossing and development of residual stresses) and the crack loading has to be regarded for describing and understanding the damage development.

Acknowledgements

Financial support by the Austrian Federal Government (in particular from the Bundesministerium für Verkehr, Innovation und Technologie and the Bundesministerium für Wirtschaft und Arbeit) and the Styrian Provincial Government, represented by Österreichische Forschungsförderungsgesellschaft mbH and by Steirische Wirtschaftsförderungsgesellschaft mbH, within the research activities of the K2 Competence Centre on “Integrated Research in Materials, Processing and Product Engineering”, operated by the Materials Center Leoben Forschung GmbH in the framework of the Austrian COMET Competence Centre Programme, is gratefully acknowledged.

References

[1] E. Kassa, Dynamic train-turnout interaction: mathematical modelling, numerical simulation and field testing, PhD Thesis, Chalmers University of Technology, Gothenburg, Sweden, 2007.

[2] M. Pletz, W. Daves, H. Ossberger, A Wheel Set / Crossing Model Regarding Impact, Sliding and Deformation- Explicit Finite Element Approach, Wear (submitted), (2012).

[3] M. Pletz, W. Daves, H. Ossberger, A Wheel Passing a Frog Nose- Dynamic Finite Element Investigation of High Axle Loads, Proceedings of the Institution of Mechanical Engineers, Part F: Journal of Rail and Rapid Transit, (2012).

[4] F.C. Liu, B. Lv, F.C. Zhang, S. Yang, Enhanced work hardening in Hadfield steel during explosive treatment, Materials Letters, 65 2333-2336.

[5] Abaqus, Abaqus user's manual, version 6.9, in.

[6] M. Pletz, W. Daves, H. Ossberger, A Dynamical Wheel Set: Crossing Model Regarding Impact, Sliding and Deformation, in: 8th International Conference on Contact Mechanics and Wear of Rail/Wheel Systems, Florence, Italy, 2009, pp. 801-809.

[7] M. Pletz, W. Daves, H. Ossberger, Dynamic Finite Element Model of a Wheel Passing a Crossing Nose, in: Tenth international conference on computational structures technology, Valencia, Spain, on-line, 2010.

[8] M. Pletz, W. Daves, S. Eck, H. Ossberger, The Plastic Adaption of Railway Crossings due to Dynamic Contact Loading - Explicit Finite Element Study, Tribology Inetrnational (submitted), (2012).

[9] J.L. Chaboche, Constitutive equations for cyclic plasticity and cyclic viscoplasticity, International Journal of Plasticity, 5 (1989) 247-302.

[10] N.K. Simha, F.D. Fischer, G.X. Shan, C.R. Chen, O. Kolednik, J-integral and crack driving force in elastic–plastic materials, Journal of the Mechanics and Physics of Solids, 56 (2008) 2876-2895.

[11] J. Tillberg, F. Larsson, K. Runesson, A study of multiple crack interaction at rolling contact fatigue loading of rails, Proceedings of the Institution of Mechanical Engineers, Part F: Journal of Rail and Rapid Transit, 223 (2009) 319-330.

[12] J.R. Rice, A.S.o.M. Engineers, A path independent integral and the approximate analysis of strain concentration by notches and cracks, ASME,

1968.